

**Ion optics and beam dynamics optimization at
the HESR storage ring for the SPARC experiments
with highly charged heavy ions**

Thesis

Oleksandr Kovalenko

2015

Ruprecht-Karls-Universität Heidelberg

Dissertation
submitted to the
Combined Faculties of the Natural Sciences and Mathematics
of the Ruperto-Carola-University of Heidelberg, Germany
for the degree of
Doctor of Natural Sciences

Put forward by
Oleksandr Kovalenko
born in Netishyn, Ukraine
Oral examination: 24th June, 2015

Ion optics and beam dynamics optimization at
the HESR storage ring for the SPARC experiments
with highly charged heavy ions

Referees:

Prof Dr. Ulrich Uwer
PD Dr. Yuri Litvinov

Zusammenfassung

Der Hochenergie-Speicherring (HESR) ist ein Teil der internationalen Beschleunigeranlage zur Forschung mit Antiprotonen und Ionen (FAIR) [1], die in Darmstadt entsteht. Die Physik mit hochgeladenen schweren Ionen wird neben der Antiprotonenphysik ein wesentlicher Teil des wissenschaftlichen Programms am HESR sein. Die Anwendung von Strahlkühlung, mit welcher die höchsten Phasenraumdichten der Strahlen erreicht werden, sowie von dünnen internen Targets ermöglicht ausgezeichnete Bedingungen für die Atomphysik an Speicherringen im Rahmen der internationalen SPARC Kollaboration [2–4].

Die existierende HESR Magnetanordnung wurde bis jetzt nur für die geplanten Experimente mit Antiprotonenstrahlen optimiert. Diese Doktorarbeit stellt neue ionenoptische Korrekturen vor, die den Betrieb des HESR mit hochgeladenen schweren Ionen ermöglicht. Die vorhandenen Ungenauigkeiten, wie Impulsbreite des Strahls, Magnetfeldfehler und Magnetfehlstellungen, führen zu Störungen der Strahldynamik: Anregung von Resonanzen und Einschränkung der Strahlstabilität. Diese Effekte werden in dieser Arbeit unter Benutzung von speziellen Simulationsprogrammen für Teilchenbeschleuniger, wie MAD-X und MIRKO, untersucht. Durch einige Korrekturrechnungen wurden nichtlineare Effekte minimiert und die Experimentbedingungen optimiert. Die Eignung der verwendeten analytischen und numerischen Werkzeuge wurde in einem dedizierten Experiment am bestehenden Speicherring ESR der GSI in Darmstadt mit einem Strahl aus heliumähnlichen Uranionen U^{90+} überprüft.

Abstract

The High-Energy Storage Ring (HESR) is a part of an upcoming International Facility for Antiproton and Ion Research (FAIR) at GSI in Darmstadt [1]. A key part of a scientific program, along with antiproton physics, will be physics with highly-charged heavy ions. Phase-space cooled beams together with fixed internal target will provide an excellent environment for storage ring experiments at the HESR for the SPARC collaboration [2–4].

Until recently, however, the existing ion optical lattice for the HESR was designed only for the experiments with antiproton beams. The thesis presents a new ion optical mode developed specifically for the operation of the HESR with highly charged heavy ions. The presence of the errors, such as beam momentum spread, magnetic field impurities or magnets misalignments, leads to disruption of beam dynamics: exciting of resonant motion and loss of beam stability. Within the paper, these effects are investigated with the help of numerical codes for particle accelerator design and simulation MAD-X and MIRKO. A number of correction techniques are applied to minimize the nonlinear impact on the beam dynamics and improve the experimental conditions. The application of the analytical and numerical tools is demonstrated in the experiment with uranium U^{90+} beam at the existing storage ring ESR, GSI.

Contents

1	Introduction	1
1.1	Overview	1
1.2	Motivation	2
1.3	Study structure	3
2	Theoretical background	4
2.1	Fundamentals	4
2.1.1	Lorentz force. Magnetic rigidity	4
2.1.2	Maxwell equations	5
2.1.3	Hamiltonian for a charged particle in electromagnetic field	6
2.2	Magnetic field multipole expansion	11
2.3	Linear betatron motion	14
2.3.1	Hill's equations	14
2.3.2	Matrix formalism	15
2.3.3	Courant-Snyder parametrization	17
2.3.4	Emittance	17
2.3.5	Normalized (Floquet) coordinates	18
2.4	Linear magnet imperfections	20
2.4.1	Dipole field errors and closed orbit distortion	20
2.4.2	Quadrupole field errors and betatron tune shift	21
2.5	Off momentum orbit	22
2.6	Momentum compaction and Transition energy	24
2.7	Chromaticity	25
2.8	Resonances	27
2.9	Numerical methods and particle tracking	28
2.9.1	Frequency map analysis	28
3	HESR storage ring	30
3.1	Magnets	30
3.2	Layout	31
3.3	Beam cooling	33
3.3.1	Electron cooling	33
3.3.2	Stochastic cooling	33
3.3.3	Stochastic vs Electron cooling	34
3.4	HESR operation modes	35
4	Ion optics and beam dynamics	36
4.1	Ion optics	36
4.1.1	Optics for the antiproton operation of the HESR	36
4.1.2	Step-by-step design of the heavy ion optics	37
4.1.3	Parameters of the developed optics	41
4.2	Closed orbit	43
4.2.1	Correction of the closed orbit	44
4.2.2	Beam-target overlap	47
4.3	Dynamic aperture (DA) studies	49

4.3.1	Tune scan	49
4.3.2	DA after chromaticity correction	54
4.3.3	DA dependence on turns	57
4.3.4	Frequency map analysis	58
4.4	Space charge tune shift	64
4.5	Charge state separation	65
4.5.1	Location 1. Target in the south-west arc	67
4.5.2	Location 2. Target in the north-west arc	68
5	Experiment with uranium beam at the ESR@GSI	71
5.1	ESR overview	71
5.1.1	Isochronous optics	72
5.2	Experiment. Dispersion measurement	73
5.3	Experiment. Transition energy	77
5.3.1	Schottky detector	77
5.3.2	Experiment outline	78
6	Summary	81
	List of Figures	83
	List of Tables	84
	Accelerator terms	85
	Bibliography	86

1 Introduction

1.1 Overview

Particle accelerators The emerging of a new branch of the physics – *accelerator physics* – is the modern evolving of the desire to look deeper into the matter and observe its details. The quality of the image is limited by the wavelength of the employed wave. For this reason we need the shortest possible waves in order to see the smallest elements of matter. Since all the particles have wave properties, those with two times the energy will allow us to see the details two times smaller. That is why we need the accelerators.

From the equation which describes the mass-energy equivalence:

$$E = mc^2 \quad (1)$$

we conclude that the more energy we "pump" into the beam the larger variety of new particles can be obtained in the particle collisions. In other words, in extremely high energy accelerators we are able to produce the particles which do not exist in the universe today.

Synchrotron Synchrotron is the name for the circular particle accelerator which has the guiding dipole magnetic field synchronously varied with the turn-by-turn increasing energy of the particles. The maximum energy here is limited by the strengths of the bending magnets and the radius of the machine. To date, the world largest 27-km-circumference accelerator Large Hadron Collider (LHC) is a synchrotron.

Storage ring Storage ring is a type of synchrotron which keeps the particles circulating with a constant energy for a long time up to many hours. There are electron and proton machines. The latter are used also for antiprotons as well as more heavy ions. The key difference between electron and proton storage rings is the presence of the *synchrotron radiation*. It scales inversely as fourth order of mass, thus for protons it is about 10^{13} times larger than for electrons. This results in the fact that the proton ring is highly sensible to any kind of perturbation because of the virtual absence of the synchrotron radiation. The perturbed electron machine, in contrast, due to radiation damping regains its equilibrium state in thousands of turns.

SPARC (Stored Particle Atomic Research Collaboration) The International Facility for Antiproton and Ion Research (FAIR) (see Figure 1.1) at Darmstadt in Germany is a science project with a versatile physics program including in-ring experiments at the High Energy Storage Ring (HESR), with the latter originally designed for experiments with antiprotons.

Relatively recently an experimental program with highly-charged heavy ions at relativistic energies in the HESR was worked out in the framework of the SPARC collaboration.

The atomic physics experiments are planned in two major research areas: collision dynamics in strong electromagnetic fields and fundamental interactions between electrons and heavy nuclei up to bare uranium.

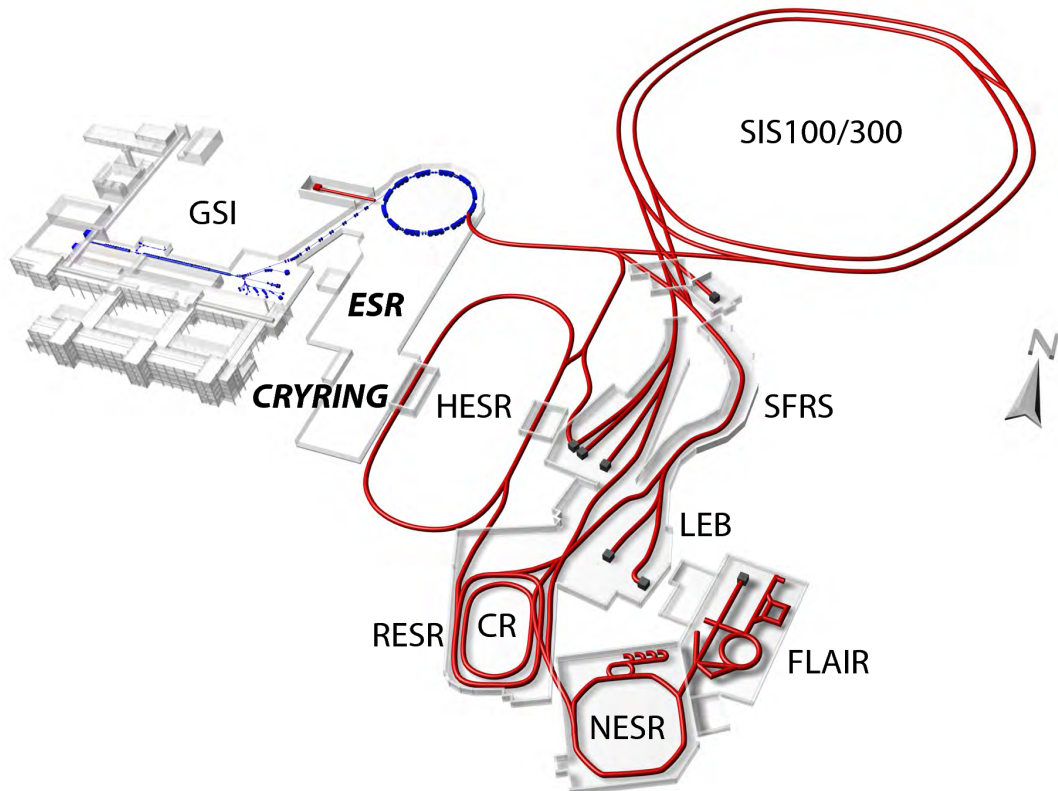


Figure 1.1: FAIR layout [5] with existing (blue) and planned (red) facilities.

For highly-charged heavy ions, FAIR will be worldwide unique with respect to the beam energies and intensities. Internal target experiments for highly-charged ions at relativistic energies will be available only at FAIR. In particular, the HESR will provide the possibility to exploit cooled heavy ion beams in the storage ring with an internal gas-jet target.

1.2 Motivation

The main motivation for the present study was to design an ion optics which is suitable for the experiments with heavy ions in the framework of the physics program of the SPARC collaboration.

Since the storage time for the physics experiments will exceed 10-15 minutes, the non-linear errors can disrupt the beam stability which eventually results in beam losses. In

order to keep the initial beam brilliance and, as a result, the achievable luminosity, a proper optimization of the optical layout parameters and the beam dynamics characteristics was crucial. The accelerator codes such as MAD-X [6], WinAgile [7] and MIRKO [8] were used in the workflow for the optical design and beam dynamics simulations.

1.3 Study structure

Section 1 provides a brief preamble to the study. Section 2 describes the theoretical background which was needed to complete the goals of the thesis, starting from Hamiltonian physics and proceeding up to the description of particle tracking codes. Section 3 presents the overview of the HESR storage ring and details of its operation. Section 4 shows the process of designing the new ion optics for heavy ions. Afterwards its thorough investigation and optimization with different techniques, such as tune scan, dynamic aperture methods and closed orbit manipulations, was performed. Finally, in Section 5 a number of lattice parameter measurements, such as the dispersion and transition energy, at the ESR storage ring at GSI is described. The obtained results are compared to the numerical simulations and theoretical predictions.

2 Theoretical background

Beam dynamics is one of the pillar branches of the accelerator physics. It studies the particles behaviour in the electromagnetic fields. Therefore we need to write the Maxwell equations which, combined with laws of classical mechanics, will serve to derive the general equations of motion of charged particles in an accelerator machine.

2.1 Fundamentals

Here we will describe the fundamental concepts with which we can get an insight on the motion of a particle in an accelerator.

2.1.1 Lorentz force. Magnetic rigidity

The second Newton's law states that the change of the momentum equals to the net force applied to the given object:

$$\frac{d\mathbf{p}}{dt} = \mathbf{F}, \quad (2)$$

In the case of a particle with charge q moving with velocity \mathbf{V} in the presence of electromagnetic field (\mathbf{E} , \mathbf{B}) the force \mathbf{F} in Equation (2) is the *Lorentz force*:

$$\mathbf{F} = q(\mathbf{E} + \mathbf{V} \times \mathbf{B}). \quad (3)$$

In the same time the work done by any force equals to

$$W = \int_1^2 \mathbf{F} \cdot d\mathbf{s} = \int_1^2 \mathbf{F} \cdot \mathbf{v} dt. \quad (4)$$

From the Equations (3) and (4) the electric field \mathbf{E} directly changes the particle energy and is mainly used for beam *acceleration*. The magnetic force does not affect the energy of the particle due to its orthogonality with particle velocity. On the other side, due to presence of the velocity in the product in Equation (3), for relativistic energies it can bend the beam path much more effectively than the electric field. Consequently, the role of the magnetic field in high energy accelerators - to make the particles move along a circular trajectory confined inside the aperture of the magnets. In other words, magnetic fields *steer* and *focus* the beam in the machine.

Let's consider a particular case when the magnetic field \mathbf{B} is perpendicular to velocity: it is a valid approximation because the relativistic beams in the accelerator have transverse velocity components which are extremely small comparing to the longitudinal ones. In the presence of the static magnetic field from the equality of the Lorentz magnetic term

in Equation (3) and centrifugal force $\mathbf{F} = mv^2/\rho$ we can calculate the bending radius (or gyroradius):

$$\rho = \frac{mv}{qB} = \frac{p}{qB}, \quad (5)$$

where m is the mass and p is the momentum of the particle. From Equation (5) we can express the product of bending field B and bending radius ρ :

$$B\rho[Tm] = \frac{p}{q} = \frac{10}{2.998} \frac{A}{Z} p[GeV/c/u], \quad (6)$$

where Ze and A are the particle charge and the atomic mass number respectively. The product in Equation (6) is called *magnetic* or *momentum rigidity* [9]. It is one of the basic concepts of accelerator physics and shows the effect of the dipole field on the motion of the particles. It calculates the value of the magnetic field required to bend the particle with a certain momentum-to-charge ratio in a dipole magnet with a defined radius.

2.1.2 Maxwell equations

As was already mentioned, in accelerators we normally use electric fields to increase particles energy and magnetic fields to guide and focus particles. Therefore we need the equations which govern the laws of electromagnetism. In its present form they were first denoted by James Clerk Maxwell and thus are called *Maxwell equations*.

Gauss' law for electricity states that the electric flux out of any closed surface is proportional to the electric charge enclosed within its surface:

$$\oint \mathbf{E} d\mathbf{S} = \frac{q}{\epsilon_0}, \quad \nabla \cdot \mathbf{E} = \frac{\rho}{\epsilon_0}, \quad (7)$$

where ϵ_0 is the vacuum permittivity, ρ is the total charge density.

Gauss' law for magnetism states that the net magnetic flux out of any closed surface is zero:

$$\oint \mathbf{B} d\mathbf{S} = 0, \quad \nabla \cdot \mathbf{B} = 0. \quad (8)$$

Another formulation of its law is that there are no magnetic multipoles.

Faraday's law of induction shows how a time varying magnetic field induces an electric field. More precisely, it states that the line integral of an electric field around a closed loop equals to the negative of the rate of change of the magnetic flux through the area enclosed by this loop:

$$\oint \mathbf{E} d\mathbf{l} = -\frac{d\Phi_B}{dt}, \quad \nabla \times \mathbf{E} = -\frac{\partial \mathbf{B}}{\partial t}. \quad (9)$$

Here Φ_B is the magnetic flux through the surface.

Ampere's law describes how the electric current as well as time varying electric field generate the magnetic field. In particular case of static electric field, it says that the line integral of the magnetic field around a closed loop is proportional to the electric current flowing through the loop:

$$\oint \mathbf{B} \, d\mathbf{l} = \int (\mu_0 \mathbf{J} + \mu_0 \epsilon_0 \frac{\partial \mathbf{E}}{\partial t}) d\mathbf{S}, \quad \nabla \times \mathbf{B} = \mu_0 \mathbf{J} + \mu_0 \epsilon_0 \frac{\partial \mathbf{E}}{\partial t}. \quad (10)$$

Here \mathbf{J} is the current density.

In all the preceding equations \mathbf{E} is the electric field, \mathbf{B} - magnetic field, \mathbf{J} - current density, ρ - total charge density, ϵ_0 is the electric constant (vacuum permittivity) and equals to 8.8542×10^{-12} F/m, μ_0 is the magnetic constant (vacuum permeability) and equals $4\pi \times 10^{-7}$ H/m. Stokes' and Gauss-Ostrogradsky (divergence) theorems are used to convert from integral to differential form.

After we specify the charge density ρ and the current density \mathbf{J} the Maxwell equations are used to calculate the electric and magnetic fields. An important property of the equations is that they are linear in fields and sources. That means that we can apply the principle of superposition and decompose some complicated fields in a set of simpler ones. This property will be used for the field multipole expansion in Section 2.2.

2.1.3 Hamiltonian for a charged particle in electromagnetic field

The Hamiltonian in the Hamiltonian mechanics has the same role as force in the Newtonian mechanics. They both describe the dynamics of the system. Between these two approaches the Hamiltonian mechanics has the freedom of using any independent variable¹, not only the time as in Newton equations of motion.

When comparing Lagrangian and Hamiltonian formalisms the latter has a number of advantages as well. The most important one is that with the canonical transformations in Hamiltonian mechanics we can convert from one to another canonical coordinates and momenta. With a good transformation choice it greatly facilitates the problem solving.

General form To describe the motion of the charged particles in electromagnetic field we need to construct the Hamiltonian. To do that, a conjugate pair of variables needs to be found. In its turn it requires a Lagrangian which, when substituting in the Euler-Lagrange equation:

$$\frac{d}{dt} \frac{\partial L}{\partial \dot{r}} - \frac{\partial L}{\partial r} = 0 \quad (11)$$

¹In accelerator physics a common choice for the independent variable is a "distance along the beam line" denoted as s

will give us the equations of motion associated with the Lorentz force from Equation (3). The form of the Lagrangian of the particle with charge e in electromagnetic field² is as follows:

$$L = \frac{mv^2}{2} - e\phi + e\mathbf{A}\mathbf{v}, \quad (12)$$

where \mathbf{v} is the velocity, \mathbf{A} is vector magnetic potential and ϕ is scalar electric potential. The electric and magnetic fields associated to these potentials are:

$$\mathbf{B} = -\nabla \times \mathbf{A}, \quad \mathbf{E} = -\nabla\phi - \frac{\partial\mathbf{A}}{\partial t} \quad (13)$$

The relativistic Lagrangian is:

$$L = -mc^2/\gamma - e\phi + e\mathbf{A}\mathbf{v}, \quad (14)$$

where γ is the Lorentz factor:

$$\gamma = \frac{1}{1 - \beta^2} \quad (15)$$

with $\beta = v/c$ where v is the particle velocity and c is the speed of light.

By definition, the conjugate momentum for the coordinate x is:

$$P_x = \frac{\partial L}{\partial v_x} = mv_x + eA_x. \quad (16)$$

In an analogous manner calculating p_y and p_z we obtain the relationship for the *canonical momentum*:

$$\mathbf{P} = m\mathbf{v} + e\mathbf{A}. \quad (17)$$

Canonical momentum should be distinguished and is generally different from the ordinary mechanical momentum $\mathbf{p} = m\mathbf{v}$.

The Legendre transformation, which are used to derive the Hamiltonian from the Lagrangian, are written [10] as follows:

$$H(q_i, P_i, t) = \sum \dot{q}_i P_i - L(q_i, \dot{q}_i, t), \quad (18)$$

where q_i are the generalized positions and P_i are the canonical momenta. Now applying the above-defined transformation from Equation (18) to the Lagrangian in Equation (12) we obtain the expression for the Hamiltonian for a relativistic charged particle in EM field:

$$H = \frac{1}{2}[(\mathbf{P} - e\mathbf{A})]^{1/2} + e\phi, \quad (19)$$

²Note that the q in this section is reserved for denoting the generalized coordinate in Hamiltonian formulation thus we use e for the charge of the electron. For a charged ion we must replace e by Ze

where \mathbf{P} is canonical momentum. This is a non-relativistic Hamiltonian. If we take into account also the relativistic effects, the Hamiltonian is found in the same way from the corresponding relativistic Lagrangian from Equation (14). Keeping in mind the relativistic notations for energy $E = \gamma mc^2$ and momentum $\mathbf{p} = \gamma m \mathbf{v}$ with Equation (17) the form of the Hamiltonian for relativistic particles in the electromagnetic fields becomes:

$$H = [(\mathbf{P} - e\mathbf{A})^2 c^2 + m^2 c^4]^{1/2} + e\phi. \quad (20)$$

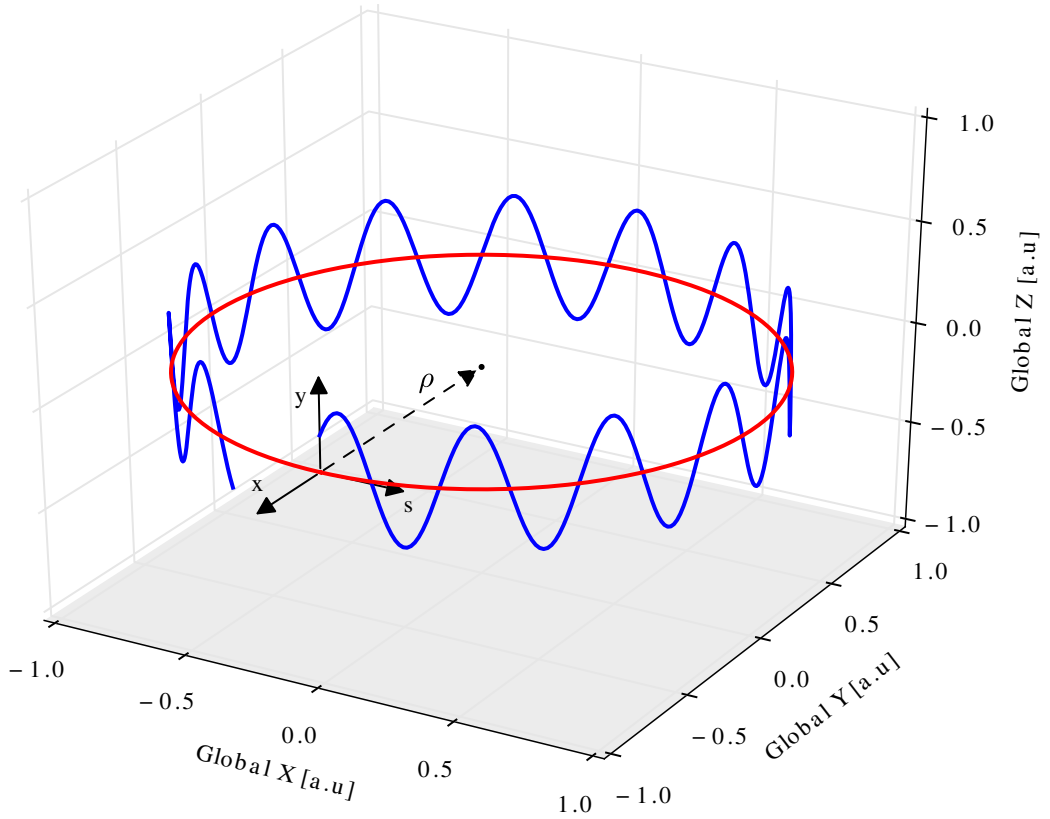


Figure 2.1: Motion in Frenet-Serret curvilinear coordinate system. The circular reference orbit (red) and particle oscillatory motion (blue) are shown. ρ - local bending radius, s - longitudinal coordinate parallel to the propagation direction of reference particle.

Converting to curvilinear coordinates The ease or difficulty of solving the equations of motion depends very much on the choice of coordinate system. In the beam dynamics we have a sequence of magnets placed along some straight or circular line. It is convenient to view the particle motion as deviations from this ideal or, a more common name, *reference orbit*. Consequently we choose the most suitable coordinates for the beam dynamics description which are the Frenet-Serret curvilinear coordinates (x, y, s) (see Figure 2.1) which

moves along this ideal reference trajectory. ρ is the radius of curvature of the reference orbit at the given location. Defining three unit vectors $(\hat{x}, \hat{y}, \hat{s})$ with their direction along the three coordinates respectively (x, y, s) , we can write the equation for the particle trajectory:

$$\mathbf{r} = \mathbf{r}_0 + x\hat{x} + y\hat{y}. \quad (21)$$

where \mathbf{r}_0 is the coordinate system origin location, (x, y) are the deviations of the particle from the origin \mathbf{r}_0 .

Now we need to derive the Hamiltonian in this new coordinate system. For that canonical transformations are performed by using a special generating function G [11]:

$$G = -(c\mathbf{P}_c - e c \mathbf{A}_c)(\mathbf{r}_0 + x\hat{x} + y\hat{y}). \quad (22)$$

Here the index c denotes the conjugate momenta and vector potential in the old Cartesian coordinates. With this generating function the Hamiltonian is transformed as [12]:

$$H_{new}(Q_k, P_k, t) = H_{old}(q_k, p_k, t) + \frac{\partial G}{\partial t}, \quad (23)$$

where q_k, p_k are the old coordinates and Q_k, P_k are the new ones. Thus the new Hamiltonian in curvilinear coordinates is transformed from the Hamiltonian in Cartesian coordinates from Equation (20) and has the following form [11]:

$$H = e\phi + c\sqrt{m^2c^2 + \frac{(P_s - eA_s(1 + x/\rho))^2}{(1 + x/\rho)^2} + (P_x - eA_x)^2 + (P_y - eA_y)^2}. \quad (24)$$

Afterwards there is a sequence of steps one has to follow in order to obtain the final equations of motions:

1. Changing the independent variable. It is convenient to change the independent variable from time t to ideal beam path s since all the electromagnetic fields are functions of beam line position s .
2. Normalization. The particle position and momentum are intended to be small: ultimately it allows to use expansion in power series of these variables in the final equations of motions. Therefore we normalize all the momenta and the Hamiltonian to the total momentum [12].

After these manipulations the new Hamiltonian is [11]:

$$H = -\left(1 + \frac{x}{\rho}\right)\left(-\frac{eA_s}{p} + \sqrt{1 - \left(P_x - \frac{eA_x}{p}\right)^2 - \left(P_y - \frac{eA_y}{p}\right)^2}\right) \quad (25)$$

where P_x and P_y are now the normalized canonical momenta, i.e. $P_x = P_{x,old}/p$ and

$P_y = P_{y,old}/p$. We also used $E^2 = (H - e\phi)^2 = p^2c^2 + m^2c^4$.

3. Approximations. In the accelerator physics one uses mostly the transverse fields which can be derived from the longitudinal A_s component of the vector potential. In this case we can neglect the other two components and put $A_x = A_y = 0$. Another common valid approximation in beam dynamics is a so called small-angle (paraxial) approximation in which the transverse momenta are much less than the longitudinal one. In other word we can write: $p \approx p_s$. The normalized momenta in our case equal to the trajectory slopes, namely $x' = dx/ds = p_x/p_s \approx p_x/p$; $y' = dy/ds = p_y/p_s \approx p_y/p$ and, due to paraxial approximation, $x' \ll 1$, $y' \ll 1$. We also introduce the momentum deviation $\delta = \Delta p/p_0 = (p - p_0)/p_0$ for off-momentum particles, i.e. for the particles whose momentum deviates from the reference momentum p_0 . Now in the first order we can replace $1/p = 1/[p_0(1 + \delta)] \approx (1 - \delta)/p_0$.

After these approximations the form of the Hamiltonian, which was defined in Equation (24) is much simpler:

$$H \approx -\left(1 + \frac{x}{\rho}\right)\left(-\frac{eA_s}{p_0}(1 - \delta) + \sqrt{1 - x'^2 - y'^2}\right) \quad (26)$$

In general the slopes x' and y' are not canonical momenta. But because of the first approximation we applied, where we set the transverse components of the vector potential A_x, A_y to zero, the slopes *are* now canonical.

Equations of motion The Hamilton equations are needed to obtain the equations of motion from the Hamiltonian. They are the first-order differential equations:

$$\dot{q}_i = \frac{\partial H}{\partial p_i}, \quad \dot{p}_i = -\frac{\partial H}{\partial q_i} \quad (27)$$

with q_i, p_i canonical variables and the dot denotes the time derivative. Using the second equation in Equation (27) the equations of motion for the x direction are then:

$$P'_x = -\frac{\partial H}{\partial x}. \quad (28)$$

Here $P_x = x' - \frac{e}{p}A_x$ and this leads to the relation $P'_x = x''$. The definition of the curl in the curvilinear coordinates is:

$$\nabla \times \mathbf{A} = \frac{1}{h_x h_y h_s} \begin{vmatrix} \hat{\mathbf{x}} & \hat{\mathbf{y}} & \hat{\mathbf{s}} \\ \frac{\partial}{\partial x} & \frac{\partial}{\partial y} & \frac{\partial}{\partial s} \\ h_x A_x & h_y A_y & h_s A_s \end{vmatrix}, \quad (29)$$

where the scale factors $h_x = h_y = 1$ and $h_s = 1 + x/\rho$. We also assumed only the transverse magnetic fields which leads to zero vector potential transverse components $A_x = A_y = 0$. It results in $h_s B_y = \frac{\partial h_s A_s}{\partial x}$ and the final form of the motion equations becomes [11]:

$$x'' + \frac{e}{p_0} B_y \left(1 + \frac{x}{\rho}\right) (1 - \delta) - \frac{1}{\rho} \sqrt{1 - x'^2 - y'^2} = 0, \quad (30)$$

$$y'' - \frac{e}{p_0} B_x \left(1 + \frac{x}{\rho}\right) (1 - \delta) = 0. \quad (31)$$

These are the equations of motion for an arbitrary transverse magnetic field expressed as

$$\mathbf{B} = B_x(x, y)\hat{x} + B_y(x, y)\hat{y}, \quad (32)$$

for a particle with momentum deviation $\delta = \Delta p/p$.

2.2 Magnetic field multipole expansion

In Section 2.1.2 we found that a principle of superposition can be applied to the magnetic field solution obtained from the Maxwell equations. Considering this, it is useful to represent the magnetic field as a set of multipoles. With such decomposition we can identify how pure the magnetic field is, i.e. how strong is the main desired multipole (dipole, quadrupole or higher order) comparing to other multipole orders.

Let's consider a space which does not contain charges and currents – a beam pipe if we neglect the beam inside – and fields which are static, i.e. does not change with time. So we can rewrite the differential Maxwell Equations (8) and (10):

$$\nabla \cdot \vec{B} = 0. \quad (33)$$

$$\nabla \times \mathbf{B} = 0 \quad (34)$$

The magnetic field $\mathbf{B} = (B_x, B_y, B_z)$ with B_z constant, which satisfies both these equations, is of the form:

$$B_y + iB_x = C_n(x + iy)^{n-1} \quad (35)$$

where C_n - complex constant, B_x, B_y - real field components. To prove the above assumption we can apply the differential operator:

$$\frac{\partial}{\partial x} + i \frac{\partial}{\partial y} \quad (36)$$

to both sides of Equation (35). Since B_x and B_y are independent of z and B_z is constant

we come to the conclusion that the field in Equation (35) satisfies the modified Maxwell equations from Equations (33) and (34).

The field in the form from Equation (35) is a so called "multipole field". $n = 1$ corresponds to the dipole field, $n = 2$ - quadrupole, $n = 3$ - sextupole etc. Since Maxwell equations are linear in fields (each term contains the field up to the first power) we can use the superposition law and find a new field as a solution:

$$B_y + iB_x = \sum_{n=1}^{\infty} C_n (x + iy)^{n-1} \quad (37)$$

which in polar coordinate system is:

$$B_\theta + iB_r = \sum_{n=1}^{\infty} C_n r^{n-1} e^{i(n-1)\theta} \quad (38)$$

To follow a common notation we rewrite the Equation (37) in the following form:

$$B_y + iB_x = B_{ref} \sum_{n=1}^{\infty} (b_n + ia_n) \left(\frac{x + iy}{R_{ref}} \right)^{n-1} \quad (39)$$

where B_{ref} and R_{ref} are the reference field and the reference radius which are commonly represented by the main dipole field and the radius at which a_n, b_n are measured. a_n, b_n are the normalized multipoles with a_n - normal and b_n - skew component. The latter introduces "coupling" which is roughly the interchange between horizontal and vertical motion. A high-quality magnet has the multipole coefficients a_n, b_n less than few units of 10^{-4} relative to the main field.

The multipole expansion in cylindrical coordinates reads:

$$B_\phi + iB_r = B_{ref} \sum_{n=1}^{\infty} (b_n + ia_n) \left(\frac{re^{i\phi}}{R_{ref}} \right)^{n-1} \quad (40)$$

One of the main advantages of a multipole expansion of a magnetic field is that it provides an accurate compact data which can be fed to the beam dynamics codes. When the beam line has several hundreds of different magnets, the multipole maps are an extremely efficient technique for constructing the transfer maps for each of the magnetic elements. And the transfer map, in its turn, is used for computation of the positions and the momenta of the particles in small incremental steps along the beam path.

The examples of pure quadrupole and sextupole multipole fields are presented in Figure 2.2.

Accelerator magnets The magnets in accelerator are divided by the type of multipole field they produce. Among the most important are:

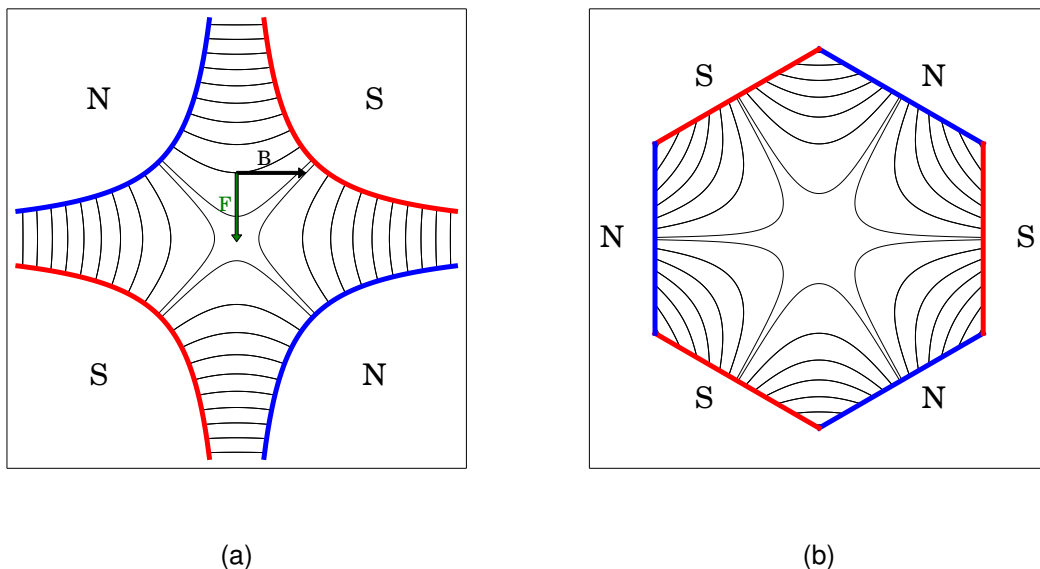


Figure 2.2: Pure quadrupole (a) and sextupole (b) fields in the transverse plane. For a quadrupole field the direction of the Lorentz force for a positively charged particle is presented with a green arrow, a black arrow shows the magnetic field direction.

- Dipole magnets for guiding the beam along the design orbit. The other uses of dipole magnets:
 - Corrector magnets – for small angle corrections;
 - Kicker magnets – for injection or ejection of the beam;
 - Undulators – for producing a synchrotron radiation in electron rings;
- Quadrupole magnets for beam focusing;
- Sextupole magnets for chromaticity correction;
- Octupoles, higher-order multipole magnets for high-order field errors corrections.

The so called "skew" magnets are obtained by rotating the "upright" magnet by an angle $\pi/2n$, where n is the multipole order. Thus, for instance, a skew quadrupole magnet is just a normal one rotated by 45° .

The properties of the normal dipole, quadrupole and sextupole fields are given in the Table below:

Table 2.1: Normal (upright) multipole components in Cartesian and cylindrical coordinates.

	Cartesian	Cylindrical
Dipole	$B_x(x, y) = 0$ $B_y(x, y) = B_0$	$B_r(r, \varphi) = B_0 \sin \varphi$ $B_\varphi(r, \varphi) = B_0 \cos \varphi$
Quadrupole	$B_x(x, y) = gy$ $B_y(x, y) = gx$	$B_r(r, \varphi) = gr \sin 2\varphi$ $B_\varphi(r, \varphi) = gr \cos 2\varphi$
Sextupole	$B_x(x, y) = g'xy$ $B_y(x, y) = g'(x^2 - y^2)$	$B_r(r, \varphi) = \frac{1}{2}gr'^2 \sin 3\varphi$ $B_\varphi(r, \varphi) = \frac{1}{2}gr'^2 \cos 3\varphi$

2.3 Linear betatron motion

The basic goals of beam dynamics can be achieved by using only two types of magnets, dipoles and quadrupoles³, which, respectively, bend and focus the beam in the accelerator. Beam transport systems, based only on these two lowest order magnet types are called linear systems because of the constant or linear restoring forces produced. And the resulting theory of particle dynamics in the presence of such magnets only is referred to as *linear beam dynamics* or simply *beam optics* [11].

2.3.1 Hill's equations

The particle in a cyclic accelerator, e.g. in storage ring, moves around a so called closed orbit. From its name it is the orbit that closes on itself after one revolution. In an ideal lattice without magnet errors the closed orbit passes through the centers of all quadrupole magnets and coincides with the reference orbit defined previously.

Let us keep only linear fields, i.e. the general field will be described to first order in the transverse coordinates. We also neglect the vertical bending. Then the expression for the field will be:

$$B_y = B_0 - \frac{\partial B_y}{\partial x}x = B_0 - B_1x, \quad B_x = \frac{\partial B_y}{\partial x}y = B_1y. \quad (41)$$

With this field the equations of motion from (30) and (31) can be rewritten in a simpler form [14]:

³Dipoles and quadrupoles sometimes are combined into one magnet called *combined function* magnet [13]. Nowadays, though, it is rarely used.

$$\begin{cases} x''(s) + \left(\frac{1}{\rho(s)^2} - k(s)\right)x(s) = \frac{1}{\rho(s)} \frac{\Delta p}{p}, \\ y''(s) + k(s)y(s) = 0. \end{cases} \quad (42)$$

with normalized to the magnetic rigidity both dipole strength $1/\rho = \frac{1}{B\rho}B$ and quadrupole strength $k = \frac{1}{B\rho} \frac{\partial B}{\partial x} = \frac{1}{B\rho}B_1$. This set of equations (42) is called Hill's equations [15]. .

For now let's consider an on-momentum particle ($p = p_0$). Then the Hill equations are changed to the following homogeneous form:

$$\begin{cases} x''(s) + K_x(s)x = 0, \\ y''(s) + K_y(s)y = 0. \end{cases} \quad (43)$$

Here K_x and K_y are the focusing functions which equal $K_x = 1/\rho^2 - B_1/B\rho$, $K_y = B_1/B\rho$, where $B_1 = \partial B_y/\partial x$.

2.3.2 Matrix formalism

We can represent the focusing functions $K_{x,y}(s)$ in Equation (43) as piecewise constants since the accelerator magnets have uniform or almost uniform shape of magnetic field – this is a so called hard edge approximation.

Let's take one of the equations from Equation system (43). Let it be the one that describes particle betatron motion in horizontal plane. The expressions which will be derived in this section are equally valid for the vertical plane as well. So we have the equation

$$x''(s) + K_x(s)x = 0, \quad (44)$$

with the periodic focusing function $K_x(s + L) = K_x(s)$. Here we consider the circular accelerator with a circumference L .

Assuming an exponential solution and solving the characteristic equation we obtain the piecewise solution for the particle trajectory:

$$x = \begin{cases} a \cos(\sqrt{K} + b), & K > 0, \\ as + b, & K = 0, \\ a \cosh(\sqrt{K} + b), & K < 0. \end{cases} \quad (45)$$

The constants a and b can be found from the initial values x and x_0

Let's define a vector which we will call "particle state vector" and which consists of the coordinate and the trajectory slope of the particle:

$$\vec{x}(s) = \begin{cases} x(s), \\ x'(s). \end{cases} \quad (46)$$

Then the solution of the Equation (44) can be rewritten as

$$\vec{x}(s) = M(s|s_0)\vec{x}_0. \quad (47)$$

where the transfer matrix $M(s|s_0)$ from position s_0 to s is defined:

$$M(s|s_0) = \begin{cases} \begin{pmatrix} \cos(\sqrt{K}l) & \frac{1}{\sqrt{K}} \sin(\sqrt{K}l) \\ -\sqrt{K} \sin(\sqrt{K}l) & \cos(\sqrt{K}l) \end{pmatrix}, & K > 0, \text{ focusing quadrupole,} \\ \begin{pmatrix} 1 & l \\ 0 & 1 \end{pmatrix}, & K = 0, \text{ drift,} \\ \begin{pmatrix} \cosh(\sqrt{K}l) & \frac{1}{\sqrt{K}} \sinh(\sqrt{K}l) \\ \sqrt{K} \sin(\sqrt{K}l) & \cos(\sqrt{K}l) \end{pmatrix}, & K < 0, \text{ defocusing quadrupole,} \end{cases} \quad (48)$$

where $l = s - s_0$. In all cases we have the following condition for the determinant of the transfer matrix:

$$\det M = 1, \quad (49)$$

due to the theorem which states that the Wronskian determinant of two independent solutions (in our case these are the cos-like and sin-like solutions) of the Equation (44) is *const*. In our case that the determinant of any magnetic element transfer matrix is unity and it leads to the preservation of the phase space density. This is called a *Liouville's theorem* [16]. It states that the particle density remains constant in a system with conservative forces only.

The transfer matrix for a pure sector dipole, where focusing function $K_x = 1/\rho^2$, is written in the following way:

$$M(s|s_0) = \begin{pmatrix} \cos(\theta) & \rho \sin(\theta) \\ -\frac{1}{\rho} \sin(\theta) & \cos(\theta) \end{pmatrix}. \quad (50)$$

Here $\theta = l/\rho$, l is the length of a dipole magnet, ρ is the bending radius.

The transfer matrix of two consecutive magnet elements is just the multiplication of their individual matrices:

$$M(s_2|s_0) = M(s_2|s_1)M(s_1|s_0). \quad (51)$$

With the help of the matrix method the particle state vector can be tracked along the transfer line. This is called *particle tracking* and it is done via numerical simulations. Given the initial particle state vector at a starting point s_0 one can find the coordinate of the particle at any other point s .

The condition for stability of the motion fulfils when the net transfer matrix remains bounded if the number of lattice elements increases indefinitely. Thus for the periodic lattice which consists of the blocks with transfer matrix M the stability criteria reads:

$$|\text{Trace}(M)| \leq 2 \quad (52)$$

2.3.3 Courant-Snyder parametrization

A general form for a matrix M with determinant equal to unity can be parametrized as:

$$M = \begin{pmatrix} \cos(\varphi) + \alpha \sin(\varphi) & \beta \sin(\varphi) \\ -\gamma \sin(\varphi) & \cos(\varphi) - \alpha \sin(\varphi) \end{pmatrix} = \hat{I} \cos(\varphi) + \hat{J} \sin(\varphi), \quad (53)$$

where α, β, γ are Courant-Snyder parameters, φ is the phase advance, \hat{I} is the unit matrix and \hat{J} is expressed as:

$$\hat{J} = \begin{pmatrix} \alpha & \beta \\ -\gamma & -\alpha \end{pmatrix}, \quad (54)$$

with $\hat{J}^2 = -\hat{I}$ or $\beta\gamma - \alpha^2 = 1$.

2.3.4 Emittance

The solution of the Hill's equation in horizontal plane reads:

$$\begin{cases} x = \sqrt{\varepsilon} \sqrt{\beta(s)} \cos(\varphi - \varphi_0), \\ x' = -\frac{\sqrt{\varepsilon}}{\sqrt{\beta}} (\alpha \cos(\varphi - \varphi_0) + \sin(\varphi - \varphi_0)). \end{cases} \quad (55)$$

Here $\alpha = -\beta'/2$, ε is a so called emittance, φ is the phase functions which, with some derivation, can be found as:

$$\varphi = \int \frac{ds}{\beta(s)}. \quad (56)$$

The ellipse formed by the trajectory of one particle in the phase space is defined by the expression

$$\varepsilon = \gamma x^2 + 2\alpha x x' + \beta x'^2, \quad (57)$$

where β, α, γ are Twiss or Courant-Snyder parameters. Another names are betatron or optical functions. The Equation (57) is derived from Equation (55) if we take into account $\beta\gamma - \alpha^2 = 1$.

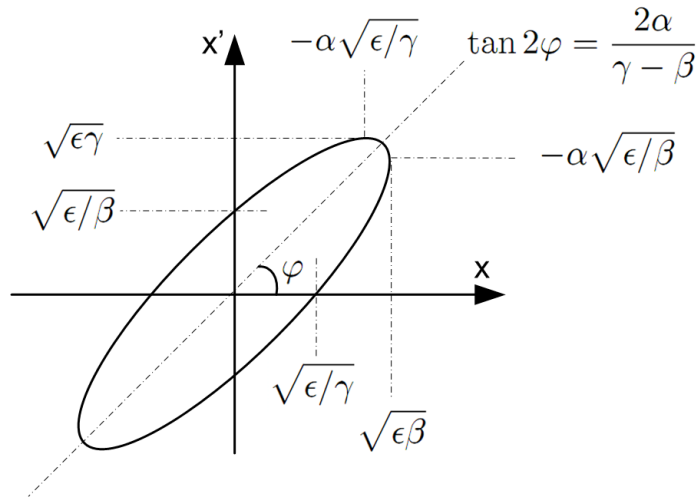


Figure 2.3: Courant-Snyder invariant ellipse.

The Equation (57) defines the particle trajectory in the $x - x'$ phase space, which is plotted in Figure 2.3. The emittance ε has a simple geometrical meaning – when multiplied by π it is the area of the ellipse encircled by the particle in the phase space. According to Liouville's theorem the emittance is an invariant of motion. It means that although emittance shape and orientation changes along the accelerator, the particle which started on a certain ellipse stays on it.

Since the trajectory angles x' are expressed as dimensionless tangents, emittance have the dimension of distance. The units are either $\text{mm} \cdot \text{mrad}$ or μm and they are equivalent.

2.3.5 Normalized (Floquet) coordinates

Let's consider an equation:

$$x''(s) + K(s)x = 0, \quad (58)$$

with $K(s) = K(L+s)$ where L is the circumference of the circular accelerator. We perform the transformation from variables (x, s) to (ω, φ) :

$$\omega = \frac{x}{\sqrt{\beta}}, \quad \varphi = \frac{1}{v} \int \frac{ds}{\beta}. \quad (59)$$

In these new coordinates the Equation (58) reads

$$x'' + kx = \frac{1}{v^2 \beta^{3/2}} [\dot{\omega} + (\frac{1}{2} \beta \beta'' - \alpha^2 + k\beta^2) v^2 \omega] = p, \quad (60)$$

where $\dot{\omega} = \frac{\partial \omega}{\partial \varphi}$ and p is the introduced perturbation (field error, momentum error, etc.), which was not present in the equations yet. The expression in Equation (60) $\frac{1}{2} \beta \beta'' - \alpha^2 + k\beta^2 = 1$ because of the β -function property. Hence we have:

$$\dot{\omega} + v^2 \omega - v^2 \beta^{3/2} p = 0. \quad (61)$$

Such an equation can be obtained from the Hamiltonian of the following form:

$$H = \frac{1}{2} \dot{\omega}^2 + \frac{1}{2} v^2 \omega^2 - v^2 \beta^{\frac{n+2}{2}} \frac{p_n}{n} \omega^n, \quad (62)$$

where $p = p_n x^{n-1} = p_n \beta^{n-1} \omega^{n-1}$. If we convert to action-angle variables, the Hamiltonian is brought into the form convenient for studying the perturbation effects.

Taking into account that v is constant and considering no perturbations ($p = 0$) we come to the harmonic oscillator and its solution:

$$\omega = \omega_0 \cos(\psi + \psi_0). \quad (63)$$

where $\psi = v\varphi$. The transformation matrix is then given

$$M(s|s_0) = \begin{pmatrix} C(\psi) & S(\psi) \\ C'(\psi) & S'(\psi) \end{pmatrix} = \begin{pmatrix} \cos(\psi) & \sin(\psi) \\ -\sin(\psi) & \cos(\psi) \end{pmatrix}. \quad (64)$$

Now with equation $x(s) = a\sqrt{\beta(s)}\cos(\psi(s))$ we finally obtain

$$\begin{cases} \omega = \frac{x}{\sqrt{\beta}} = a\cos(\psi), \\ \frac{d\omega}{d\psi} = \sqrt{\beta}x' + \frac{\alpha}{\sqrt{\beta}}x = -a\sin(\psi). \end{cases} \quad (65)$$

The use of the normalized coordinates not only allows us to treat particle beam dynamics equivalent to a harmonic oscillator but is also convenient in studying the perturbations. In the phase space each particle moves along the closed trajectories in the form of an ellipse which we called the phase ellipse. If we use normalized coordinates, the unperturbed phase ellipse becomes an invariant circle as shown in Figure 2.4. Finally, in the phase space with the new coordinates we obtained an ideal circular motion in the phase

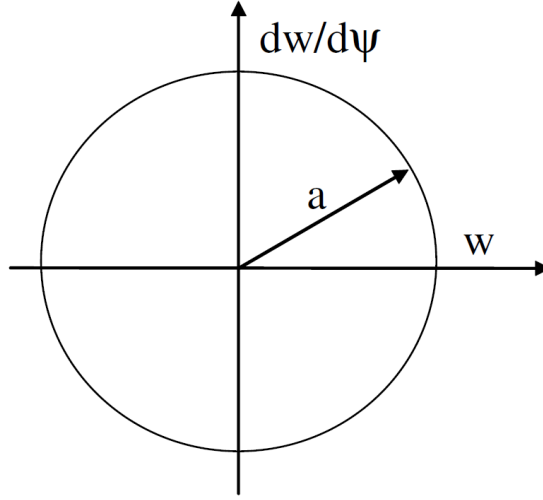


Figure 2.4: Phase space in normalized coordinates.

space with radius a (see Figure 2.4), which is betatron oscillations amplitude.

2.4 Linear magnet imperfections

When considering small magnetic field errors, the Hill's equations are modified as:

$$\begin{cases} x'' + K_x(s)x = \frac{\Delta B_y}{B\rho}, \\ y'' + K_y(s)y = -\frac{\Delta B_x}{B\rho}, \end{cases} \quad (66)$$

and the magnet field errors ΔB_y and ΔB_x are represented according to multipole expansion (see Section 2.2):

$$\Delta B_y + i\Delta B_x = B_0 \sum_{n=0}^{\infty} (b_n + ia_n)(x + iy)^n, \quad (67)$$

where B_0 is the main dipole field, b_n -coefficients are normal field errors, a_n -coefficient represents the skew magnetic field error. We need to study the effect of different order errors on the beam dynamics.

2.4.1 Dipole field errors and closed orbit distortion

Dipole field errors distort the closed orbit around which the particle perform betatron oscillation. Usually the dipole field error comes from the rolled dipole magnet or a misaligned quadrupole.

The equation of motion which should be solved is:

$$x''(s) + K_x(s)x = \frac{\Delta B_0}{B\rho}, \quad (68)$$

where $\frac{\Delta B_0}{B\rho}$ represents the normalized dipole error. The similar equation is for the vertical plane. The solution consists of a regular betatron motion and the closed orbit deviation. Applying the matrix formalism, the closed orbit distortion due to N dipole errors θ_i at locations s_i can be calculated as:

$$x(s) = \frac{\sqrt{\beta(s)}}{2 \sin(\pi\nu)} \sum_{i=1}^N \sqrt{\beta_i} \theta_i \cos(|\varphi(s) - \varphi(s_i)| - \pi\nu), \quad (69)$$

where ν is a betatron tune of the machine, i.e. the number of oscillations for a complete revolution, φ is a phase advance, β_i are the values of the beta functions at the positions of the dipole kicks. The Equation (69) shows that the deviation goes to infinity when the betatron tune ν is integer. Thus the betatron tune should always be sufficiently far from integer values.

Dipole corrector magnets are used to correct the distorted closed orbit. The detection of the orbit coordinate is done with Beam Position Monitor (BPM). The right positioning of the dipole correctors and BPMs with respect to the phase advance is crucial for effective closed orbit correction.

2.4.2 Quadrupole field errors and betatron tune shift

The quadrupole error occurs due to the following effects:

- Error in magnetic field of the quadrupole magnets;
- Error in dipole magnets;
- Closed orbit deviation in sextupoles;
- Sextupole magnets misalignment.

The focusing function $K(s)$ is determined by the quadrupole field. As a consequence the quadrupole field error leads to β -function distortions which causes change of tunes $\nu_{x,y}$.

Let's consider a Hill equation of betatron motion with respect to the closed orbit

$$x'' + K(s)x = 0 \quad (70)$$

with perturbed focusing function $K(s) = K_0(s) + \delta K$ due to quadrupole gradient error δK . The condition of periodicity is fulfilled: $K(s) = K(s+L)$, where L is the circumference.

Let M_0 be the one turn transfer matrix of a machine without perturbation

$$M_0 = I \cos(\mu_0) + J \sin(\mu_0), \quad (71)$$

where I is a 2×2 unit matrix and J is:

$$J = \begin{pmatrix} \alpha(s) & \beta(s) \\ -\gamma(s) & -\alpha(s) \end{pmatrix}. \quad (72)$$

Here $\alpha(s), \beta(s), \gamma(s)$ are betatron function amplitudes of the ideal machine.

The transfer matrix M_{Qerr} for infinitesimal quadrupole error δK at location s_1 over a short length ds_1 is

$$M_{Qerr} = \begin{pmatrix} 1 & 0 \\ -\delta K(s_1)ds_1 & 1 \end{pmatrix}. \quad (73)$$

The one turn transfer matrix for the machine with a perturbation is then $M_{tot} = M_{Qerr} \times M_0$ and therefore equals:

$$M_{tot} = \begin{pmatrix} 1 & 0 \\ -\delta K(s_1)ds_1 & 1 \end{pmatrix} \cos(\mu_0) + \begin{pmatrix} \alpha & \beta \\ -\alpha\delta K(s_1)ds_1 & -\beta\delta K(s_1)ds_1 - \alpha \end{pmatrix} \sin(\mu_0). \quad (74)$$

The phase advance μ of the perturbed machine can be obtained from the trace of M_{tot} :

$$\cos(\mu) = \frac{1}{2} \text{Trace}(M_{tot}) = \cos(\mu_0) - \frac{1}{2} \beta \delta K(s_1) ds_1. \quad (75)$$

For small $\delta\mu = \mu - \mu_0$ we have:

$$\delta\mu = -\frac{1}{2} \beta(s_1) \delta K(s_1) ds_1. \quad (76)$$

And for the distributed along the ring quadrupole error the expression for the tune shift reads:

$$\delta\nu = \frac{\Delta\mu}{2\pi} = \frac{1}{4\pi} \oint \beta(s_1) K(s_1) ds_1 = 0. \quad (77)$$

One can clearly see that large tune shifts can be produced by the quadrupole errors in high- β locations.

2.5 Off momentum orbit

Beam guidance and focusing depends on the momentum of the particle which follows directly from the Lorentz force expression from Equation (3). And the beam is never monoenergetic. Therefore we need to take into account the deviation from the reference momentum δ which is defined as:

$$\delta = \frac{p - p_0}{p_0}, \quad (78)$$

where p is the particle momentum and p_0 is the reference momentum. Expanding the transverse motion equation to first order in x/ρ and taking into account only first order of a momentum-dependent part we obtain:

$$x'' + K_x(s)x = \frac{\delta}{\rho}, \quad (79)$$

where $K_x = 1/\rho^2 + B_1/B\rho$ with B_1 as a quadrupole gradient. The solution of this equation can be expressed with the sum of the solution of homogeneous part $x_\beta(s)$ and a particular solution of the inhomogeneous part x_δ :

$$x(s) = x_\beta(s) + x_\delta. \quad (80)$$

Therefore the particle motion is the sum of betatron motion:

$$x_\beta = \sqrt{\varepsilon_x \beta_x(s)} \cos(\varphi_x + \varphi_0) \quad (81)$$

and a displacement because of the momentum error:

$$x_\delta = D(s)\delta. \quad (82)$$

Here $D(s)$ is called "dispersion function".

Now we can introduce the 3×3 transfer matrix where the third dimension is responsible for the motion due to off-momentum. To give an example of a new transfer matrix for off-momentum particles, we will bring the transfer matrix for a sector dipole with $K_x = 1/\rho^2$ which reads then:

$$M(s|s_0) = \begin{pmatrix} \cos(\theta) & \rho \sin(\theta) & \rho(1 - \cos(\theta)) \\ -(1/\rho) \sin(\theta) & \cos(\theta) & \sin(\theta) \\ 0 & 0 & 1 \end{pmatrix}, \quad (83)$$

where θ is the bending angle. Hence the closed orbit for an off-momentum particle is no longer the one which goes through the center of all magnets. Instead, now it is determined by the momentum term δ . To calculate the particle trajectory we use the following relation:

$$\begin{pmatrix} x(s) \\ x'(s) \\ \delta \end{pmatrix} = M(s|s_0) \begin{pmatrix} x(s_0) \\ x'(s_0) \\ \delta \end{pmatrix} \quad (84)$$

2.6 Momentum compaction and Transition energy

A particle with coordinate x moves along a trajectory with a curvature radius $\rho + x$ and the associated length of the path dL in this case is:

$$dL = (\rho + x) d\theta = (\rho + x) \frac{ds}{\rho} \quad (85)$$

where ds is the corresponding distance along the reference trajectory. Neglecting the betatron motion we obtain the total path the particle covers per one revolution:

$$L = \oint \left(1 + \frac{x}{\rho}\right) ds = L_0 + \oint \frac{x}{\rho} ds = L_0 + \oint \frac{D(s)\delta}{\rho} ds, \quad (86)$$

where L_0 is the machine circumference. Now we introduce the *momentum compaction factor* α_c which is the relative change in the particle path length with respect to the particle relative momentum deviation. Taking into account the relations from Equations (82) and (86) we obtain:

$$\alpha_c = \frac{dL}{L_0} \frac{1}{\delta} = \frac{1}{L_0} \oint \frac{D(s)}{\rho} ds \quad (87)$$

Therefore it appears that the path elongation for off-momentum particles arises only from the curved sections (where curvature radius $\rho \neq \infty$) with non-zero dispersion.

The time it takes for a particle to cover a distance L is:

$$T = \frac{L}{c\beta} \quad (88)$$

Hence:

$$\frac{dT}{T} = \frac{dL}{L} - \frac{d\beta}{\beta} \quad (89)$$

Knowing that

$$\frac{d\beta}{\beta} = \frac{1}{\gamma} \frac{dp}{p} \quad (90)$$

and with Equation (89) we rewrite the Equation (87) as:

$$\frac{dT}{T} = \left(\alpha_c - \frac{1}{\gamma^2}\right) \delta = \eta_c \delta \quad (91)$$

where η_c is the *momentum compaction*. Introducing a new term called *transition energy* which is:

$$\gamma_{tr} = 1/\sqrt{\alpha_c} \quad (92)$$

we rewrite the expression (91):

$$\frac{dT}{T} = \eta_c \delta = \left(\frac{1}{\gamma_{tr}^2} - \frac{1}{\gamma^2} \right) \delta \quad (93)$$

or keeping in mind that $dT/T = -df/f$ the previous equations becomes in terms of frequency variation:

$$\frac{df}{f} = -\eta_c \delta = \left(\frac{1}{\gamma^2} - \frac{1}{\gamma_{tr}^2} \right) \delta \quad (94)$$

Here is the meaning of the transition energy. During the acceleration the particle will reach the transition point, at which the energy added to the particle can no longer translate to the velocity increase since the velocity approaches the speed of the light. Instead it converts to the mass of the particle almost without changing particle velocity. Thus the frequency of the revolution drops down since the velocity does not change and orbit becomes longer due to dispersion function. This energy, at which the transition occurs, is called the *transition energy*.

To summarise it, there are three cases, depending on the beam energy, which are defined in the following way:

- $\gamma > \gamma_{tr}, \eta_c > 0$: above transition condition – the revolution time increases with energy increase,
- $\gamma < \gamma_{tr}, \eta_c < 0$: below transition condition – the revolution time decreases with energy increase,
- $\gamma = \gamma_{tr}, \eta_c = 0$: a so called *isochronous* condition: frequency is independent of the energy.

The last case needs special attention. In proton machines the transition crossing is extremely dangerous because of the loss of the longitudinal phase focusing which leads to complete beam loss. Though when talking about storage rings, the ion optics adjusted in the isochronous condition gives an opportunity for the high precision mass measurement [17]. The explanation, why the transition energy should be equal to the ion energy, is simple: in the isochronous ring the particles with a velocity spread will, nonetheless, all have the same revolution frequency.

2.7 Chromaticity

The particle beam in the ring is never monochromatic, i.e. it has finite spread in energy (momentum). It is important to study the effect of this momentum distribution on the ion optics.

The focusing strength of a quadrupole magnet is given with

$$k[m^{-2}] = \frac{\partial B/\partial x}{B\rho}, \quad (95)$$

where $B\rho$ is magnetic rigidity. For a particle with a momentum error δ quadrupole focusing strength becomes

$$k[m^{-2}] = \frac{\partial B/\partial x}{(1-\delta)B\rho}. \quad (96)$$

Thus, depending on the momentum of the particle the focusing strength of quadrupole can be strengthened or weakened.

Let's write equations of motion neglecting the quadratic terms of the amplitudes and the momentum error. It will be

$$\begin{cases} x'' + kx = kx\delta - \frac{1}{2}m(x^2 - y^2), \\ y'' - ky = -ky\delta + mxy, \end{cases} \quad (97)$$

where k and m are the normalized quadrupole and sextupole gradients respectively.

Now from Equations (80) and (82) we set $x = x_\beta + \delta\eta$ with η as the dispersion function. Ignoring the quadratic terms of (x, y, δ) , the Equation (97) is transformed to

$$\begin{cases} x''_\beta + kx_\beta = (k - m\eta)x_\beta\delta, \\ y''_\beta - ky_\beta = -(k - m\eta)y_\beta\delta. \end{cases} \quad (98)$$

In the r.h.s. of the above set of equations we have a linear perturbation term with respect to the betatron amplitude. From Section 2.4.2 it is already known that this type of error leads to the tune shift

$$\begin{cases} \Delta\nu_x = -\frac{\delta}{4\pi} \oint \beta_x(k - m\eta)ds = \delta\xi_x, \\ \Delta\nu_y = -\frac{\delta}{4\pi} \oint \beta_y(k - m\eta)ds = \delta\xi_y. \end{cases} \quad (99)$$

where $\xi_{x,y}$ is called chromaticity and it is one of the basic parameters to describe the machine. It shows that the quadrupoles, when acting on the off-momentum particles, change their frequencies thereby introducing the tune spread. If this effect is not controlled, the beam will occupy a large area in the $Q_x - Q_y$ tune plane with the potential crossing of the resonance lines.

Chromaticity has two major effects in high-intensity rings: one is the tune spread from the combined effect with the momentum spread, other is its role in controlling the collective instabilities, such as e.g. head-tail instability [18].

Chromaticity correction If we provide the sextupoles with the right normalized gradient m we can completely correct the chromaticities. From Equation (99) at least 2 sextupoles are needed to compensate the chromaticities in both planes. Equation (99) also shows that the locations with large dispersion are more preferable to minimize the sextupole strength. With grouping the sextupoles into the families⁴ the sextupole strengths can be reduced even more.

The drawback of introducing the sextupole fields to the beam line is that, if not properly arranged by the phase advance [19], sextupole magnets can lead to significant shrinking of the dynamic aperture.

2.8 Resonances

Perturbation terms in the equation of motion can lead to a beam instability called "resonance". It occurs when the perturbation acts synchronously with the oscillation motion. If perturbation frequency coincides with the frequency of the particle the betatron amplitude is amplified due to turn-to-turn coherent kicks. It leads to the resonance phenomena and eventually to the particle loss. These perturbations come from the field imperfections, misplacements of magnets in the lattice and from particles momentum spread.

From Section 2.4 it was concluded that we should avoid the integer and half-integer tunes due to dipole and quadrupole errors respectively. These are so called linear resonances.

To take into account also higher-order errors and corresponding resonances, the general condition for the resonances in the transverse plane should be written. Neglecting the coupling between transverse and longitudinal motion the resonance condition states:

$$kQ_{0x} + lQ_{0y}m = pN, \quad (100)$$

where Q_{0x} , Q_{0y} are the ion optics tunes in horizontal and vertical planes respectively, k, l, p are integer values. The order of the resonance equals to $|k + l|$.

Any tune working point finds itself on a resonance of some order. But the lower order resonance have faster instability growth times comparing to higher order ones. Hence, it is important to place the lattice tunes in the region which is free of, at least, low-order structure resonances – as a rule of thumb, up to fourth order (see the resonance diagram in Figure 4.10). For instance, in the LHC the tune working point is adjusted to avoid the resonances up to 12th order [20].

To find the effect of different field multipole errors a Hamiltonian perturbation theory is employed [11,21]. Having constructed a generating function to obtain a new pair of canonical variables we can transform the Hamiltonian to much simpler form. After that we neglect the

⁴Groups of the magnets with the same strength

terms above some order in perturbation and obtain an approximate solution for the equations of motion. In this way we can analyze, for example, the change of the betatron tune with the betatron amplitude or beam dynamics in the vicinity of the resonances.

2.9 Numerical methods and particle tracking

...all models are wrong, but some are useful.

George Box, statistician

Simulation modelling is the process of creating and analyzing a prototype of a physical model to predict its performance in the real world [22]. In accelerator physics we need to have an algorithm with an aim to predict the motion of the particles in the ring. Having constructed a particle tracking model we can investigate the behaviour of the beam in magnetic fields with certain approximations.

Therefore the most efficient way to determine beam stability characteristics for a particular lattice design is to perform numerical particle tracking studies.

The tracking module PTC (Polymorphic Tracking Code) of MAD-X [6] accelerator code performs element-per-element tracking of particle trajectories for a defined number of turns. The multipole errors can be chosen to be systematic or statistical as well as the particle momentum deviation is taken into account. The motion of single particles in phase space can be observed together with an analysis of the frequency spectrum of the particle under the influence of all nonlinear fields. The PTC symplectic⁵ treatment of all accelerator elements gives full control over the precision of the computation results. Hence sometimes we can sacrifice in accuracy to gain in time and vice versa.

For instance, in case of sextupole correction the tracking code can be employed to maximize the dynamic aperture. By varying the strength of a sextupole, one at a time, the dynamic aperture is determined through particle tracking and any variation that produces an increase in the dynamic aperture is accepted as the new sextupole strength.

This makes particle tracking one of the most integral and focal techniques in accelerator physics which helps to explore significant features of the beam dynamics.

2.9.1 Frequency map analysis

In the linear beam dynamics the tune, which is the number of the particle betatron oscillation per one revolution, is constant. However, in the presence of the beam momentum spread it is the sextupole nonlinear fields which have to be introduced to compensate the chromaticity

⁵Symplecticity should be an integral property of any accelerator code [23], otherwise non-physical changes to the system are introduced.

effect. Besides, there are always non-linear terms of the magnetic fields coming from the magnet non-perfect manufacturing and their misalignments while installing. It all gives rise to the nonlinearities which lead to the dependence of the tunes on the particle amplitude.

If the nonlinearities are not very strong, the KAM (Kolmogorov-Arnold-Moser) theorem [24] states that the motion can still be stable when far from resonances. Therefore if the resonances are not strongly excited, for relatively small amplitudes we can observe stable linear motion with small changes of tunes. However, for some initial coordinates we can observe an unstable motion which leads to the tune change with time, which is called Arnold diffusion [25]. Therefore by studying the change of the tunes associated with a range of initial conditions we can obtain an indication of the system stability.

We can use the results obtained from the particle tracking to determine the tunes depending on the betatron amplitude. Performing the DFT (Discrete Fourier Transform) with windowing, the mapping from the spatial plane $x - y$ to tune space $Q_x - Q_y$ is provided [26]. Besides that, the change of frequency with time can indicate the dangerous zones in beam phase space, which can lead to beam loss, and which need detailed investigation.

The above-described technique – *Frequency Map Analysis (FMA)* – gives us a picture of a resonant structure, chaotic and stable regions in the beam phase and tune spaces. The further resonance analysis can give hints for optimizing the lattice and finding better correction schemes. The frequency map analysis was used for improving the beam stability at the LHC [27]. Besides LHC, with this method relatively good agreement in the few percent range between the model and experiment was obtained at a number of machines around the world [28, 29].

3 HESR storage ring

The HESR storage ring is one of the most important components of the FAIR accelerator facility. It will accommodate the key experiments of the FAIR physics program such as internal target experiments with antiprotons [30]. Another remarkable feature of the ring is its ability to be fed and to employ the unstable isotopes as well as stable highly charged heavy ions. It is a worldwide unique experimental physics program with highly charged heavy ions which will provide an opportunity to investigate the interaction of the relativistic cooled highly charged heavy ions with matter. Furthermore, it will allow to explore fundamental interactions in strong electromagnetic fields. A hydrogen gas jet target with variable density of up to 10^{15} cm^{-2} [31,32] will be provided for the internal target experiments.

The two types of systems for beam cooling, namely electron cooler and stochastic cooling facility, will provide the full control of the beam in 6D phase space.

The electron cooler can also be used as a target of free electrons to explore ion-electron interactions. Besides this, the powerful petawatt laser beams [33] will be employed either for beam cooling or for precision spectroscopy.

The storage ring with a circumference of 575 m has a racetrack design and incorporates electron as well as stochastic cooling. The radio-frequency cavities contain not only accelerating-decelerating module but also the barrier bucket cavity. The latter is used for compensating of the beam energy loss coming from beam interaction with target [34]. It all favors the effective accumulation of the particle in a beam with tiny momentum spread and high brilliance.

The HESR magnetic rigidity of 5-50 Tm corresponds to the momentum range of 0.58 - 5.79 GeV/c/u for bare uranium beam, i.e. for an atomic mass number $A = 238$ and a charge state $Z = 92$. The corresponding total energy is in the range of 1.10 - 5.87 GeV/u which gives 170 MeV/u to 4.94 GeV/u in kinetic energy. Expressed in terms of Lorentz factor the range is $1.2 < \gamma < 6.3$. These are the highest energies achievable in the storage ring around the world at the moment.

3.1 Magnets

The HESR lattice consists of 44 dipole magnets for bending, 84 quadrupole magnets for focusing and 64 sextupole magnets for chromaticity correction. From 64 sextupoles there are 52 in arcs and 12 in straight sections. It should be noted that the sextupole magnet aperture is larger than the other magnets. It allows for each of the sextupole to incorporate one beam position monitor. The dipole corrector magnets, which include horizontal as well as vertical ones, are used for orbit correction purposes.

The types of the magnets used in the HESR and their parameters [35] are presented in the table 3.1

Table 3.1: Magnets at the HESR.

Magnet type	Quantity	Magnetic length	Strength	Aperture
Dipole	44	4.2 m	8.182° (Deflection angle)	100 mm
Quadrupole	84	0.6 m	20 T/m (Max gradient $\frac{\partial B}{\partial x}$)	100 mm
Sextupole	64	0.3 m	42.5 T/m ² (Max gradient $\frac{\partial^2 B}{\partial x^2}$)	135 mm
Dipole correctors	56	0.3 m	1 mrad / 2 mrad	100 mm

The aperture available for the beam is constrained by the vacuum chamber aperture to 89 mm, i.e. 11 mm less than the aperture of the dipoles and quadrupoles.

3.2 Layout

As was already mentioned, the HESR storage ring has a racetrack design with a total circumference of 575 m. More detailed review of the structure of the ring is given in this section.

Arc The two arcs of the HESR are identical by design. The length of the arc is 156 m. Each arc of the ring accommodates 4 families of quadrupoles — three focusing and one defocusing. They serve to independently control the parameters such as horizontal tune, vertical tune and dispersion function. The latter defines the value of the transition energy – see eqs. (87) and (92).

The second dipole after the start of the arc as well as the second dipole before the end are removed. This trick, which is called missing dipole concept, works as a dispersion suppressor [36] and allows for dispersion-free straight sections. It will be shown that this place, where dipole was removed, is suitable for installation of an internal target for heavy ion experiments.

The sextupoles for chromaticity correction and dipole corrector magnets are located in the free space regions between the dipoles and the quadrupoles.

From the geometrical point of view the arcs have a 2-fold symmetry. Unfortunately it is not possible to preserve such symmetry for the whole ring because of the magnet structure of the straight sections.

Straight section The 132 m long straight sections in the HESR accommodate different types of installations: cooling systems, acceleration RF cavities, injection systems and an

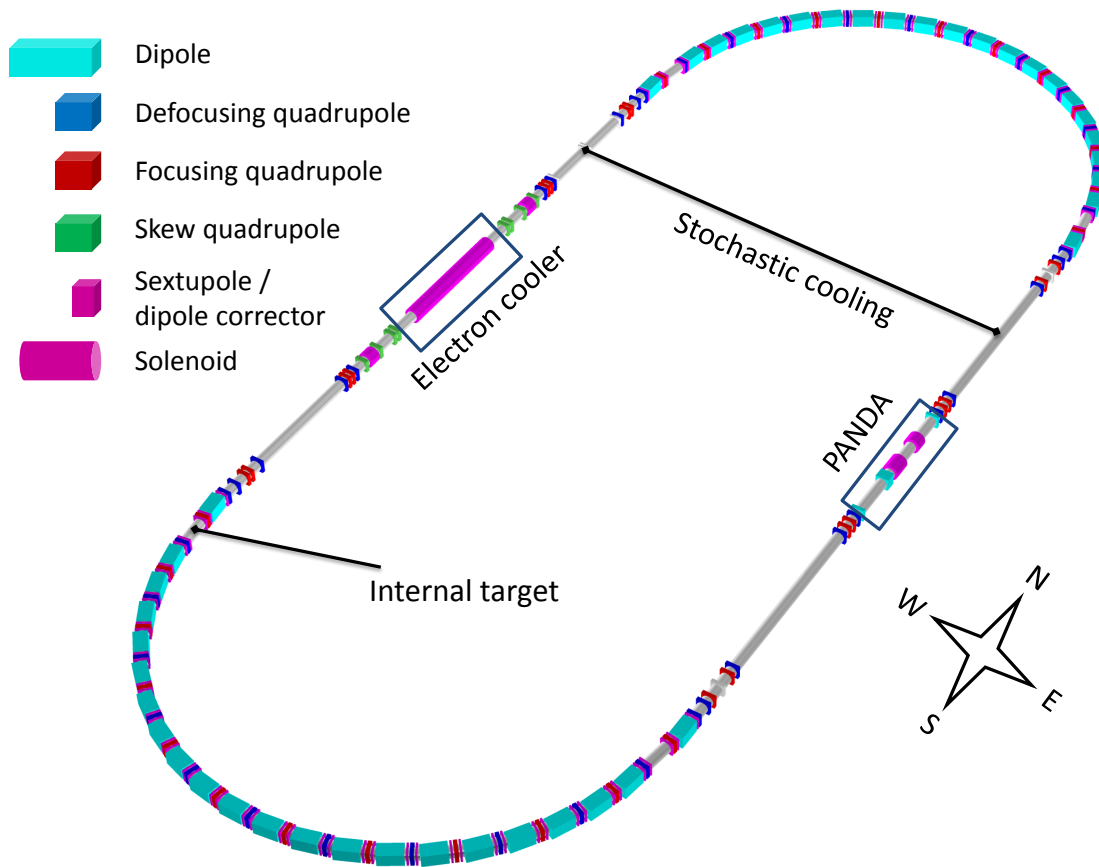


Figure 3.1: HESR layout.

internal target facility for the experiments with antiprotons. The phase advance of the each straight section is around 2π . The insertion with such a phase advance is called *telescopic* since in the presence of only linear magnetic fields it becomes virtually transparent for the beam.

Each straight section contains 4 quadrupole triplets separated by long drifts. In the west straight section an electron cooler is located whereas the east one accommodates the PANDA experimental installation. The design of the straight sections is non-identical. Despite having the same number of quadrupole split triplets their locations and the strengths of the quadrupoles are different. It all results in different ion optical parameters: the beta functions of the west straight can be varied to optimize the electron cooling whereas those in the PANDA section form a tight beam waist. More detailed description is given in Section 4.1.

The main location of the SPARC internal target for heavy ion experiments will be in the south west section of the arc (see Figure 3.1).

3.3 Beam cooling

Beam cooling is a non-Liouvillian process which reduces the beam phase space in both transverse and longitudinal directions. It is used to achieve the following goals:

- Accumulation of the particles in a storage ring;
- Increasing the luminosity for experiments;
- Counteracting the heating in internal targets and due to intra-beam scattering;
- Increasing the energy and angular resolution in experiments.

It is a remarkable feature of the HESR storage ring to cool the beam in 6D phase space. It allows to compensate the emittance blow-up coming from intra-beam scattering (IBS) and interaction with internal target. It also helps to achieve significantly less emittance size and momentum spread. The HESR is provided with two different cooling systems – stochastic and electron cooling.

3.3.1 Electron cooling

Electron cooling was invented by Gersh Budker in 1966 [37] in INP, Novosibirsk. It is based on the exchanging of the energy between an electron and an ion beam through Coulomb interaction. As a result the momentum spread as well as a transverse emittances are reduced.

A 2 MeV electron cooler [38] with an electron current of up to 3 A is planned to be installed in the first phase, called Modularized Start Version (MSV). The electron energy of 2 MeV corresponds to $\gamma = 3.9$ or velocity $\beta = 0.967$. The corresponding bare uranium ion $^{238}\text{U}^{92+}$ energy per nucleon is about $3.6 \text{ GeV}/u$. This is the maximum energy of the uranium ions that can still be cooled with the present cooler. If we increase the energy further then only stochastic cooling can be employed.

From the beam dynamics point of view the critical effect of the electron cooler comes from the toroid magnets which bend the electron beam in order to overlap it with ions. The deflecting force of the toroids on the ion beam and the necessity of the dipole correctors on both sides of the electron cooler is always a matter of a detailed investigation.

3.3.2 Stochastic cooling

Another technique for reducing the beam phase space is the stochastic cooling. This process uses the electric signal coming from deviated particles passing the pick-up device and by means of a feedback loop kicks given particles back to the beam centroid. The

technique was invented by a Dutch physicist Simon van der Meer in 1972 and in 1974 it was successfully tested.

The efficiency of the stochastic cooling strongly depends on the value of slip factor η , which relates the fractional change in the orbit period T_0 to energy, according to:

$$\frac{\Delta T}{T_0} = \eta \frac{\Delta E}{E}. \quad (101)$$

The slip factor should be small between the cooling pick-ups and kickers to minimize the "bad mixing", and the phase slip factor should be large between kickers and pick-ups to maximize the "good mixing". This way stochastic cooling will have the maximum efficiency.

It can be also shown that the total phase slip factor for the whole ring, defined in Equation (101), can be also expressed as:

$$\eta = \frac{1}{\gamma_{tr}} - \frac{1}{\gamma}, \quad (102)$$

where γ_{tr} is the transition energy. The latter equals to:

$$\gamma_{tr} = \frac{1}{\sqrt{\alpha_c}} = \left(\int \frac{D(s)}{\rho} ds \right)^{-\frac{1}{2}}. \quad (103)$$

Thus it is clear that the slip factor and thereby the stochastic cooling efficiency depend on the shape of the dispersion function $D(s)$.

3.3.3 Stochastic vs Electron cooling

Different cooling methods are used for different beams, their bunching, energies etc. Here the pros and cons of the stochastic and electron cooling methods are presented:

- Electron cooling effectiveness is independent of beam intensity whereas the stochastic cooling works better for weak beams;
- Stochastic cooling is better suited for highly charged ions because of the larger signal-to-noise ratio;
- In the electron cooling recombination between ions and electrons inevitably reduces the ion beam lifetime;
- Stochastic cooling works more effectively for "hot" beams as compared to electron cooling. The latter will be the faster, the smaller is the difference between the electron and ion velocities.

Since in the HESR both cooling methods can be applied, the advantages of both techniques can be combined in a synergistic way. The whole energy range can be covered:

electron cooling for low energies, stochastic cooling for high energies, both cooling methods in the mid energy range. Consequently, bunched as well as DC beams of different intensities can be efficiently controlled in 6D phase space.

3.4 HESR operation modes

In the framework of the SPARC the HESR can operate either with stable heavy ions (HI) or with unstable radioactive ions (RIBs). The difference is that in RIBs mode the stripped uranium ions will collide with a thick target and by means of Super-FRS (Superconducting FRagment Separator) a certain range of nuclei will be filtered and delivered to CR. In the CR the 50 ns bunch will be rotated in the phase space, then debunched to coasting beam and stochastically cooled during 1.5 s [39]. Afterwards the stochastically pre-cooled beam will be transferred to the HESR for experiments.

In heavy ion mode the fully stripped uranium ions will be directly injected through the accelerator chain SIS18-SIS100 synchrotrons via CR to the HESR for internal target experiments. The stripping foil between SIS100 and CR will help to achieve the highest charge states of the ions. The magnetic rigidity of the CR collector ring is $B\rho = 13 \text{ Tm}$ which corresponds to 740 MeV/u for bare uranium. Consequently, with this energy the ions will be injected to the HESR in the zero-dispersion east straight section. The intensities of the beam are restricted from the radiation protection point of view to the maximum value of 10^9 ions.

The transverse emittances of the injected to the HESR beam are $\varepsilon_{x,y} = 0.5 \text{ mm mrad}$ and the momentum spread $\Delta p/p = 0.05\%$, all 2σ values [40].

4 Ion optics and beam dynamics

4.1 Ion optics

4.1.1 Optics for the antiproton operation of the HESR

The initial ion optical layout for the HESR was designed by the Jülich Research Center community [41, 42] for the PANDA experiment with antiprotons – it is denoted as *antiproton optics*. It is shown in Figure 4.1 and characterized by the following properties:

- A low- β insertion in the straight section which houses the PANDA experimental facility. The purpose is to make the beta functions low in both planes in order to reduce the beam size.
- The straight sections with zero dispersion to minimize the beam cross section at the PANDA target and to avoid the transverse-longitudinal coupling effect due to RF accelerating cavities⁶
- Periodic FODO arcs whose second-to-last bending magnets are symmetrically removed. This allows for the zero dispersion outside of the arcs (i.e. in the straight sections)

The main lattice parameters can be seen in Table 4.1

Table 4.1: A list of the parameters of the antiproton optics.

Transition energy, γ_{tr}	6.23
Momentum compaction factor, α	0.026
Betatron tunes, Q_x, Q_y	7.62, 7.62
Maximum beta functions β_x/β_y	222/170 [m]
Maximum dispersion D_x	6.2 [m]
Chromaticities ξ_x/ξ_y	-14.3/-13.7

The transition energy value for this optics is $\gamma_{tr} = 6.2$. The magnetic rigidity from 5 to 50 Tesla allows to change the momentum of the antiprotons in the range from 1.5 GeV/c to 15 GeV/c. The corresponding Lorentz factor ranges from 1.9 to 16. The transition energy γ_{tr}

⁶The accelerator RF cavity gives a longitudinal kick to the particle by changing its energy. If the dispersion at the location of the cavity is not zero, see Equation (82), then this kick will be transferred to the transverse plane [43] leading to the transverse-longitudinal coupling.

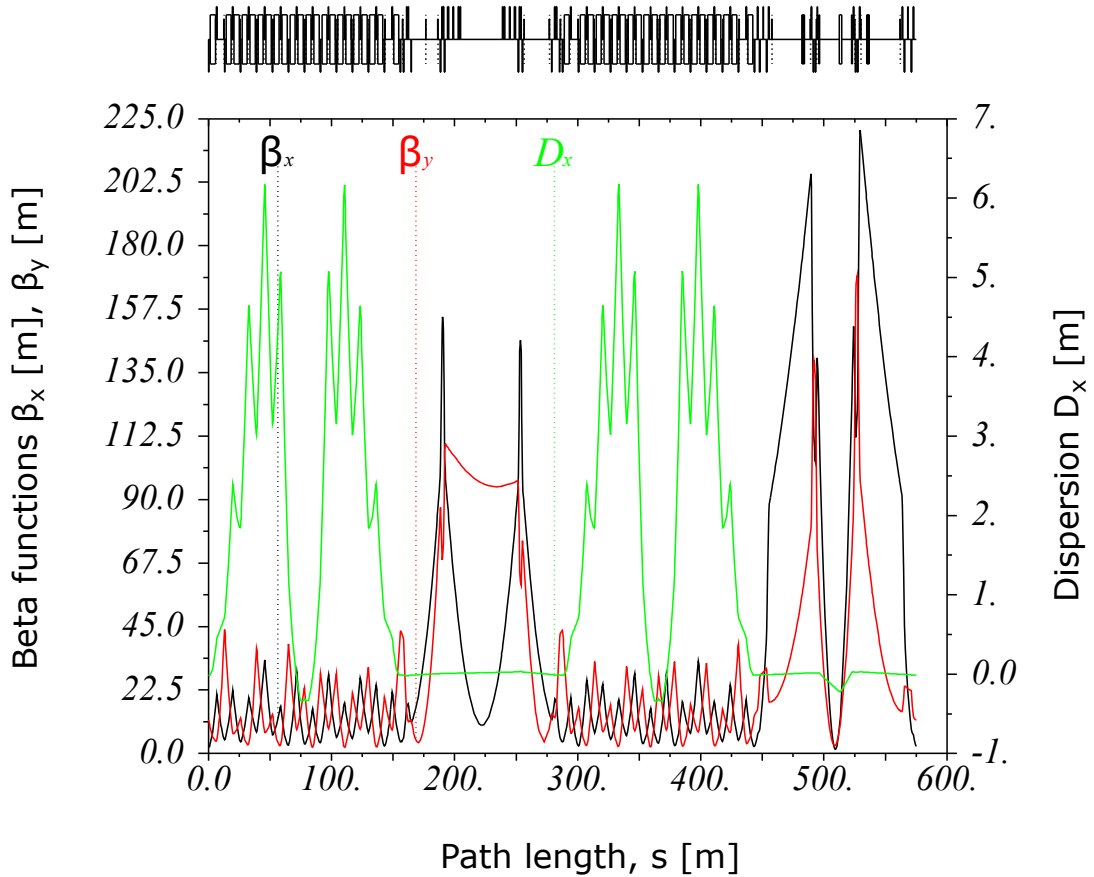


Figure 4.1: Standard antiproton optics for PANDA experiment. Dispersion function is shown with green, horizontal beta function β_x - black, vertical beta function β_y denoted with red.

value of the lattice is high enough to be above the injection energy. Otherwise the transition energy crossing would occur which would result in strong beam instabilities. And since the HESR lattice does not have fast pulsed quadrupole magnets, designed specifically for γ_{tr} -crossing, it would ultimately result in significant beam losses [44].

The PANDA experiment requires the largest luminosity during the beam-target collision which is accomplished by low beta insertion at the position $s = 509$ m (see Figure 4.1). It allows to have a collision point with low, around few meters, amplitudes of β_x, β_y -functions.

The next section presents the design process of a new ion optical layout for the HESR operating with heavy ions – *heavy ion optics*.

4.1.2 Step-by-step design of the heavy ion optics

Design strategy The heavy ion optics design strategy can be summarized in the following short statements:

- Relax the beta functions in the low- β region at the PANDA target location (Figure 4.1);
- Drive the maximum values of the beta functions down, thus enhancing the acceptance of the ring;
- Reduce the quadrupole strengths over the lattice, thereby lowering the chromaticities. The corresponding sextupole fields needed for chromaticity correction also become smaller. It leads to increasing of the dynamic aperture.

The optics matching was performed with the aid of MAD-X accelerator code.

FODO FODO cell is a common magnet structure and a typical building block of a larger lattice consisting of focusing and defocusing quadrupoles with a drift or bending magnet in between⁷. Schematically it is denoted with "QD – O – QF – O" or identically " $\frac{1}{2}$ QD – O – QF – O – $\frac{1}{2}$ QD".

The arc of the HESR is a periodic focusing structure based on the FODO cells. Such a lattice design is simple and flexible; it also has the advantages of small quadrupole strengths; it is stable against field variations and has large dynamic aperture [11].

Let's have a more detailed look at the FODO cell of the HESR storage ring. The quadrupole length l_q equals 0.6 m, the length of the whole FODO section L_{cell} is 13.0 m.

In most cases in the accelerators the length of the quadrupole l_q is much less than the focal length f , or:

$$l_q \ll f, \quad f = \frac{1}{kl_q} \quad (104)$$

where k is the normalized quadrupole gradient. If this condition holds then we can apply *thin lens approximation* and rewrite the transfer matrix of the quadrupole from Equation (48) assuming that $\sqrt{kl_q} \ll 1$. For example, for the focusing quadrupole, making an expansion to the first order of $\sqrt{kl_q}$, the transfer matrix reads:

$$M(s|s_0) = \begin{pmatrix} 1 & 0 \\ -1/f & 1 \end{pmatrix} \quad (105)$$

The next step is the calculation of the complete transfer matrix for the F (focusing quadrupole) - O (bending magnet) - D (defocusing quadrupole) - O (bending magnet) structure. We equate the obtained FODO transfer matrix to the general form for the transfer matrix in Equation (53) and apply the stability motion criteria from Equation (52). Consequently, we get a condition for a stable motion in a line, built from infinite FODO cells with focusing and defocusing quadrupoles with equal strengths. This condition reads:

⁷From the point of view of beam dynamics in curvilinear coordinates, drift and bending magnet are identical in the first order with zero momentum deviation

$$f > \frac{L_{cell}}{4} \quad (106)$$

where k is the normalized quadrupole gradient. It defines the maximum limit for the quadrupole strengths. If this condition is not fulfilled, the particle amplitudes in the FODO line will grow indefinitely with time. From the Equation (106) the maximum value of the normalized quadrupole gradient can be calculated: $k = 0.51 \text{ m}^{-2}$.

Our main goal at this stage is to find the optical beta functions which maximize the acceptance with moderate quadrupole strengths. To get the maximum value of the acceptance, the phase advance for a FODO cell should be in the range between 60 and 90 degrees [11]. The lengths of the quadrupole magnet and of the FODO cell in the HESR are 0.6 m and 13 m respectively. With these parameters the maximum beam acceptance will be for the normalized gradient ranging between $k = 0.26 \text{ m}^{-2}$ and $k = 0.36 \text{ m}^{-2}$ (see Figure 4.2). Therefore we defined the fixed range of the quadrupole strengths $k \in [0.26; 0.36] \text{ m}^{-2}$ within which we will perform further ion optics investigations.

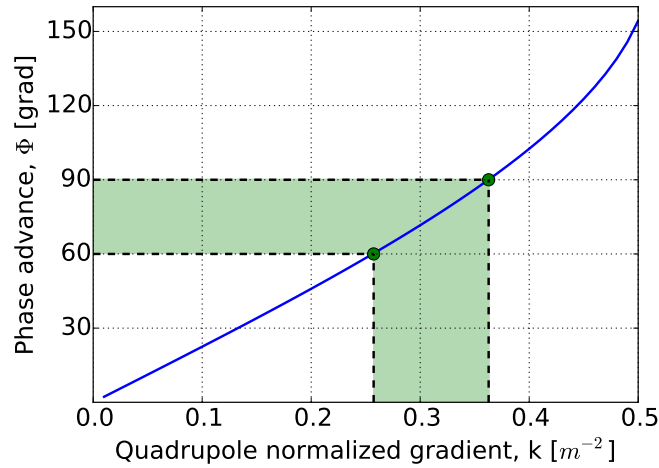


Figure 4.2: Blue line shows the dependence of the phase advance on the normalized gradient of the quadrupole in the FODO cell. The green zone indicates the range of the normalized gradient values for which the acceptance has the largest values.

The plot in the Figure 4.3 shows the FODO cell optical functions. The phase advance is 72 and 69 degrees in, respectively, horizontal and vertical planes.

As can be seen from Figure 4.3, the maximum values of the beta functions are about 21 m in both planes. The minimum β -amplitudes are close to 6 m. The periodic dispersion varies from about 2.0 m up to 3.5 m.

Arc After the FODO cell design, the optical functions in the HESR arc should be defined.

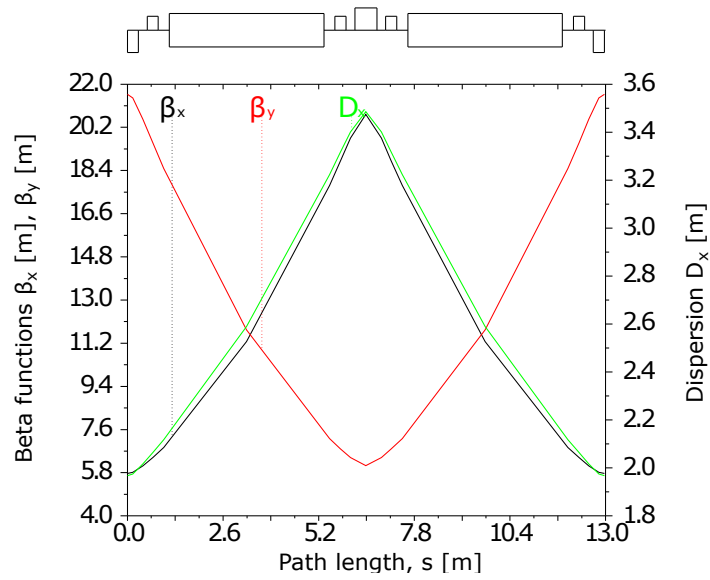


Figure 4.3: Periodic solution for the optical functions in the FODO cell. The two long magnets are the dipoles. The first, the middle and the last magnets are the quadrupoles. The other magnetic elements are sextupoles or dipole corrector magnets – they did not affect the computation.

HESR arc consists of 25 quadrupoles and has a two-fold symmetry. The first and the last quadrupole magnets of the arc have half the field gradient of the rest quadrupoles. This trick allows for the odd number of quadrupoles, which is 25 in total, make up exactly 12 FODO cells. It is because those two half-strength quadrupoles, when combined, function like one normal magnet.

Second-to-last quadrupoles from each end of the arc are removed – this serves as a missing magnet dispersion suppressor which is a widely used and easily implementable scheme. This is needed to provide dispersion free straight sections.

The matching procedure for the first half of the arc was performed. Four quadrupole families (one defocusing and three focusing) were utilized for this purpose. The following boundary conditions in the end of the half (i.e. in the middle of the full arc) were imposed: dispersion derivative D'_x and both alpha-functions α_x, α_y were set to zero. With this condition the full arc is constructed merely by mirroring the lattice of a half arc.

The final version of ion optical functions for half of the arc is presented in Figure 4.4. With a mirrored half arc we obtain a complete arc with a total length of 156 m.

Straight The straight sections each have a phase advance close to 2π . Therefore they can be represented with a transfer matrix which equals almost unity. This greatly facilitates the final matching to obtain a stable optics for the whole ring.

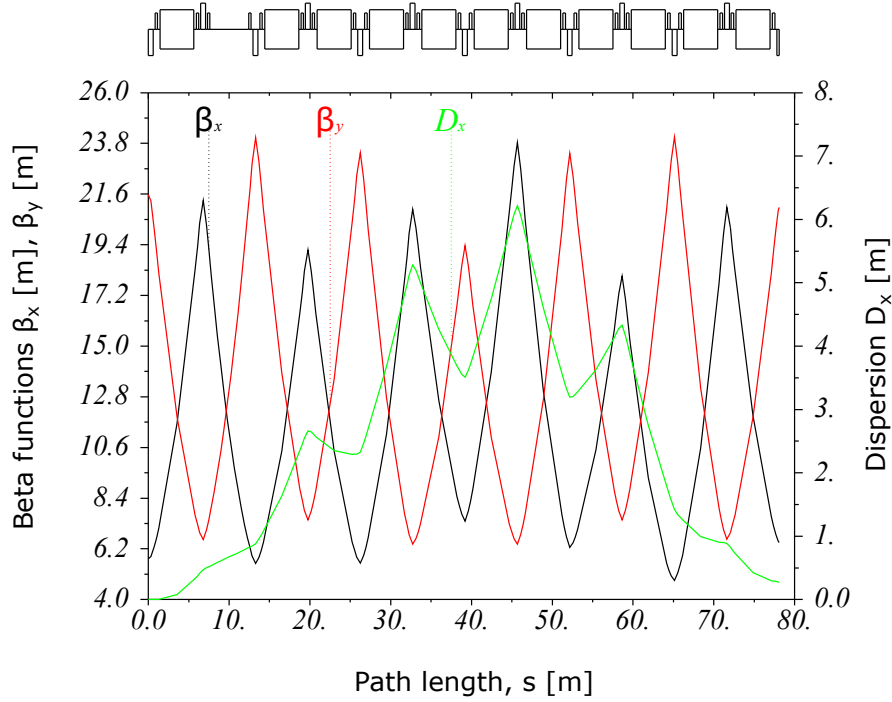


Figure 4.4: Optical functions for half of the arc.

Complete lattice The results of the full lattice optical functions β_x , β_y , D_x after the matching are shown in Figure 4.5.

4.1.3 Parameters of the developed optics

Here the main parameters of the optics developed for heavy ion operation are summarized. In addition, the side-by-side comparison to the antiproton optics is provided.

First, we define the acceptance of the lattice as the maximum emittance that a certain beam transport system can accept and transfer without losses. In the developed heavy ion optics it is determined by the horizontal and vertical beta functions which have their maximum values in the locations of electron cooler and PANDA straight sections (see Figure 4.5). Neglecting the orbit shift due to momentum spread and taking into account only betatron amplitude, it can be calculated as:

$$A_{x,y} = \frac{R^2}{\beta_{x,y,max}}, \quad (107)$$

where R is the vacuum pipe aperture which equals to 44.5 mm and we assume no closed orbit distortions. Substituting the maximum values of the beta functions, $\beta_x = 90$ m, $\beta_y = 88$ m, into the Equation (107), we obtain the following results for acceptance: the horizontal one equals to $A_x = 22.0$ mm mrad and the vertical one equals to $A_y = 22.5$ mm mrad. These are

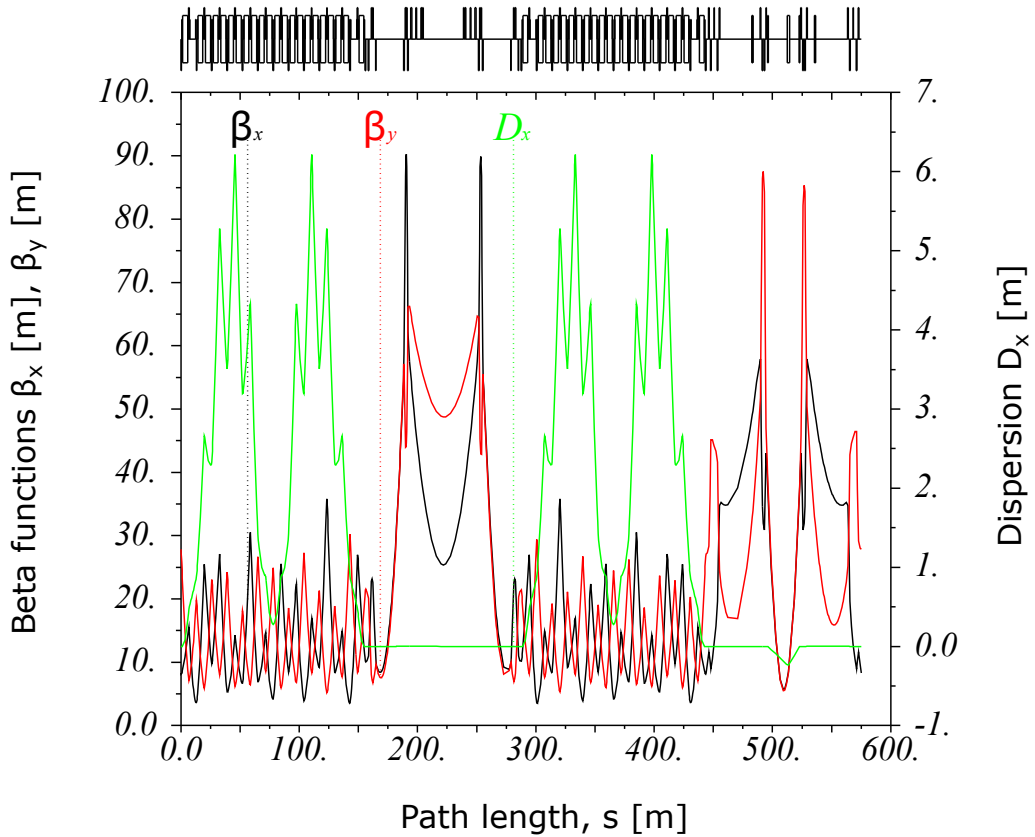


Figure 4.5: Optical functions for the full lattice. The path length $s = 0$ corresponds to the beginning of the arc. The center of the electron cooler is located at $s = 250$ m, the PANDA target is positioned at $s = 509$ m.

about 4 times larger than the acceptance for antiproton optics ($A_x = 4.9$ mm mrad, $A_y = 5.7$ mm mrad for $\beta_t = 2$ m [35]).

The moderate strengths of the quadrupoles in the developed optics result in relatively low chromaticities. It is fortunate to have as low chromaticity as possible since the required sextupole field for its correction will be minimized. The values of the chromaticities in the heavy ion optics – $\xi_x = \xi_y = -8.6$ – are equal because of the similar strength of the focusing and defocusing quadrupole strengths along the lattice. The chromaticities have significantly lower values comparing to antiproton optics. In the latter case they range up to -17 and -13 for the horizontal and the vertical planes respectively [35].

The reduced quadrupoles strengths have another effect – the tune working point is moved to $(Q_x, Q_y) = (6.87, 6.22)$ values as well as the transition energy is now smaller with value $\gamma_{tr} = 5.94$. For ion optics for antiproton operation the tunes were $(Q_x, Q_y) = (7.62, 7.62)$ and the transition energy was $\gamma_{tr} = 6.23$.

The change of the transition energy factor leads to variation of the slip factor according

to relation (102). And the latter is crucial for the effectiveness of the stochastic cooling. Since the previous studies [45] proved that the old value of the parameter $\gamma_{tr} = 6.23$, which corresponds to slip factor for injection energy $\eta = 0.28$, is effective for the cooling of heavy ion beams, it was decided keep the η -parameter constrained near the 0.28 value.

The Table 4.2 summarizes the most important parameters of the developed optics.

Table 4.2: A list of the parameters of the heavy ion mode optics.

Injection energy, E_{inj}	0.74 GeV/u
Magnetic rigidity range, $B\rho$	[5, 50] Tm
Kinetic energy range, T for $^{238}\text{U}^{92+}$	[0.17, 4.94] GeV/u
Transition energy, γ_{tr}	5.94
Slip factor (for injection energy), η	0.28
Tunes, Q_x, Q_y	6.87, 6.22
Chromaticities, ξ_x/ξ_y	-8.6/-8.6
Maximum beta functions, β_x/β_y	90/88 m
Maximum dispersion, D_x	6.2 m
Transverse acceptance hor/ver	22.0/22.5 mm mrad

4.2 Closed orbit

The magnetic field of the magnets as well as their placement along the beamline will never be perfect and thereby we have to account for the corresponding errors. For instance, an imperfection of dipole magnet field or a misalignment of a quadrupole magnet lead to the lowest order errors, namely *dipole errors*. These errors cause closed orbit distortion. As a result, the beam acceptance of such lattice is reduced. Moreover, if not controlled, the orbit distortion can be even larger than the magnet physical aperture which prevents any functioning of the accelerator.

To bring the distorted orbit back close to the reference orbit a *closed orbit correction* procedure has to be performed.

4.2.1 Correction of the closed orbit

A kick θ at some location of the beamline causes a distortion of the closed orbit [11] x_{co} at location s such as:

$$x_{co}(s) = \frac{\sqrt{\beta(s)}}{2\sin(\pi\nu)} \sqrt{\beta_\theta} \theta \cos(\pi\nu - |\Delta\varphi|), \quad (108)$$

where θ is an integrated dipole field strength in mrad, β_θ and $\beta(s)$ are the beta functions at the kick and at the distortion location s , ν is the betatron tune, $\Delta\varphi$ is the phase advance from the kick to the orbit distortion location.

With n corrector magnets the orbit distortion x_i at i -th BPM (beam position monitor) is:

$$x_i = \frac{\sqrt{\beta_i}}{2\sin(\pi\nu)} \sum_{k=1}^n \sqrt{\beta_k} \theta_k \cos(\pi\nu - |\Delta\varphi_{ik}|). \quad (109)$$

Here index k denotes the corrector magnet, $\Delta\varphi_{ik}$ is the phase advance between the i -th monitor and k -th corrector.

For n BPMs the orbit displacements due to the dipole kicks can be expressed in a matrix formulation:

$$\mathbf{x}_m = R\boldsymbol{\theta}_n, \quad (110)$$

where the elements of the matrix R are:

$$R_{ik} = \frac{\sqrt{\beta_i\beta_k}}{2\sin(\pi\nu)} \cos(\pi\nu - |\Delta\varphi_{ik}|). \quad (111)$$

Afterwards the corrector strengths can be found either by inversion of the matrix R , then the corrector strengths are $\boldsymbol{\theta}_n = \mathbf{R}^{-1}\mathbf{x}_m$, or via least square optimization. The latter method is more preferable since it avoids extreme strengths of the corrector magnets that would not be available in the accelerator.

The COD (closed orbit distortion) calculations and its correction were performed for the HESR ring in the heavy ion operation mode. Among the main causes of orbit distortions one can name:

- Linear magnetic field errors;
- Dipole rolls;
- Quadrupole misalignments.

All errors and misalignments were assumed to satisfy the Gaussian distribution with 3σ which corresponds to 99.7% confidence interval. The goal was to correct the beam orbit distortions induced by these errors. The whole process consisted of the following steps:

- Random misalignments and tilts with root-mean-square values of respectively 0.2 mm and 0.5 mrad are assigned to the lattice elements.
- Systematic as well as random magnet field errors are generated in bending and quadrupole magnets [42,46]. Gaussian distribution was assumed with $\pm 3\sigma$ cutoff;
- Closed orbit with the above defined misalignments and errors is computed;
- MAD-X MICADO algorithm with SVD (Singular Value Decomposition) preconditioning [47] is applied to find the desired strengths of the dipole corrector magnets with which the closed orbit at the beam position monitors have minimum values⁸.

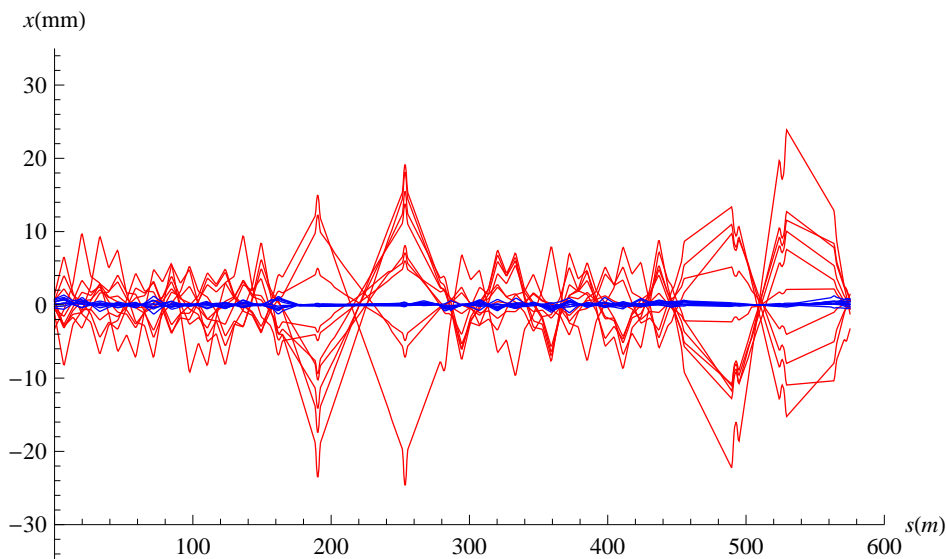


Figure 4.6: Uncorrected (red) and corrected (blue) closed orbits are shown for ten random seeds for horizontal plane.

The computation was performed with statistics of 500 random seeds for error sets generation. The example of the closed orbit correction in the horizontal plane is shown in Figure 4.6 where ten distorted closed orbits as well as their corrected versions are shown. Even with ten seeds one can observe that the maximum values of the distorted orbit can approach the 30 mm mark which is not far from the beam pipe boundaries ($\pm 44.5 \text{ mm}$). This proves the necessity of closed orbit correction during the future commissioning with beam.

⁸MICADO is an iterative "least square" method which works well only for independent dipole corrector magnets, i.e. for the correctors with in-between phase advance not multiple of π . If a pair of dependent correctors is revealed then the MICADO technique can lead to unnecessary random local bumps along the beamline. Thereby, the aim of the SVD preconditioning is to identify such linearly dependent pair of correctors and to exclude one of the magnets from the correction procedure.

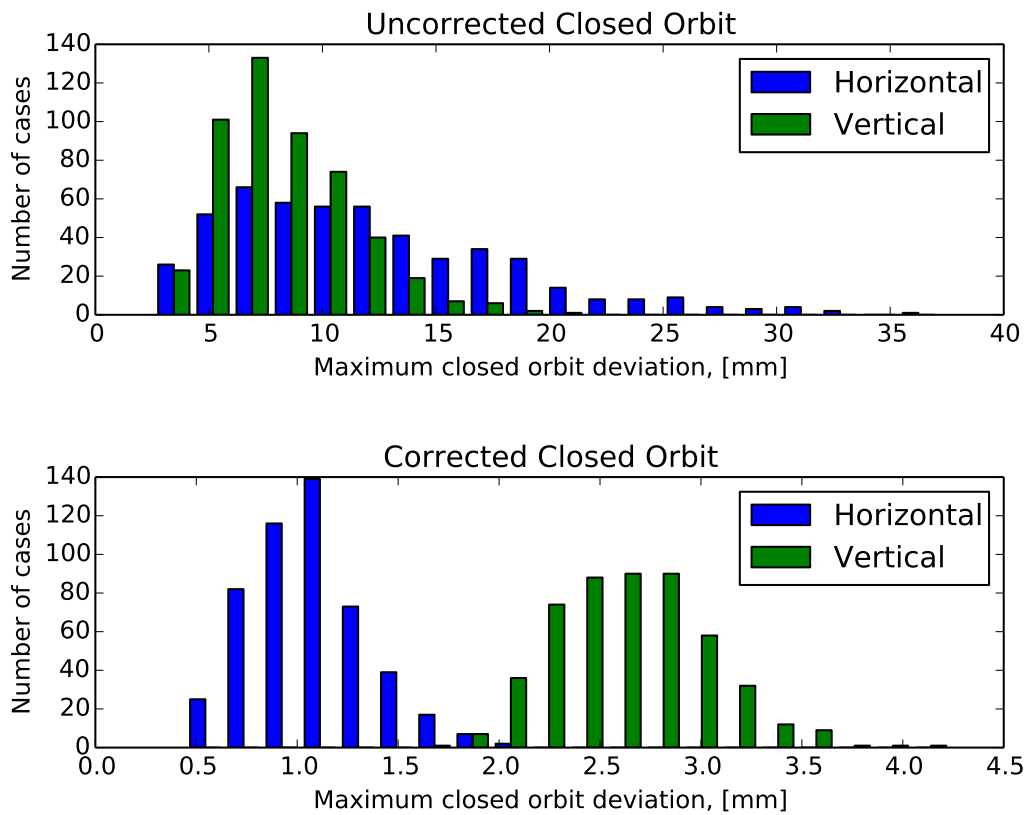


Figure 4.7: Uncorrected and corrected closed orbits maximum deviations are shown for 500 seeds for horizontal (blue) and for vertical (green) planes.

The results in Figure 4.7 show the values for the maximum closed orbit deviations before and after correction. The maximum distortion for 500 seed statistics is 36 mm horizontally and 21 mm vertically.

After the correction the most probable maximum deviation in vertical plane is 2.7 mm whereas horizontally it is 1.1 mm. For one case out of 500 in vertical plane there was a 4.2 mm deviation. For horizontal plane the maximum deviation reaches 2.0 mm. It appears that the horizontal value is more than twice smaller than vertical one. It can be explained by not identical number of correctors in two planes: the number of horizontal correctors was larger by four than that of vertical ones. Another reason is that the initial vertical uncorrected orbit has a larger spread toward the higher values comparing to the horizontal one. It all makes vertical orbit more difficult to correct at the locations of the beam position monitors .

4.2.2 Beam-target overlap

The luminosity of any internal target experiment depends on the overlap of the beam and the target. Thus to maximize the interaction area, they should be properly aligned.

In the HESR the internal target will be rigidly attached inside the vacuum chamber so it cannot change its position after installed. Even with properly aligned target the beam orbit distortions are unknown at the time before the beam commissioning - they will be measured only after beam injection. Therefore, it is the beam equilibrium orbit which should be reshaped to reach the best beam-target overlap. It will be done with the sufficient number of dipole corrector magnets around the target.

The layout of the dipole corrector magnets at the HERS was designed primarily for operating with antiprotons. The task is thereby to check whether we are able to adjust the beam for the heavy ion experiments in the SPARC target location, i.e. in the missing dipole drift inside the arc.

As was already computed in the previous Section 4.2.1, the residual deviations of the closed orbit after correction will be in the order of few mm. To be on the safe side it was assumed that the maximum orbit distortion after the correction can be up to ± 5 mm. We also make a stronger assumption that this deviation can happen exactly at the target position. To correct the orbit back, a possibility of a local closed orbit bump should be verified.

In principle, only three correctors are enough for creating a local orbit bump with an ability to change the orbit displacement. In order to be able to adjust not only the amplitude but also the angle, one more dipole corrector magnet should be utilized. This makes up a scheme consisting of four dipole corrector magnets which allows an independent control of the amplitude and the angle.

4 correctors which are closest to the target location were taken. The corrector strengths in the simulations were limited to ± 1 mrad. The orbit distortion due to the 4 correctors can be calculated from the Equation (109) where the index n equals to number of magnets, 4 in our case. Differentiating the equation gives the angle of the orbit x'_s at the observed location s .

Creating of the bump implies a set of preconditions. They consist of zero closed orbit outside the four correctors or $x(s_4) = x'(s_4) = 0$, where s_4 is the location of the fourth corrector. We also need to adjust the orbit to a zero angle and 5 mm bump at the target position or $x(s_{target}) = 5\text{mm}$, $x'(s_{target}) = 0$.

The created closed orbit bump in the horizontal plane with a 5 mm displacement and zero angle is given in the Figure 4.8.

From the plot the unfortunate residual effects of the correction scheme are clear: although still inside the beam pipe, the residual deviations of the closed orbit reach the amplitude of about 15 mm. This is caused by the inappropriate phase advances in the pairs "corrector-corrector" and "corrector-target".

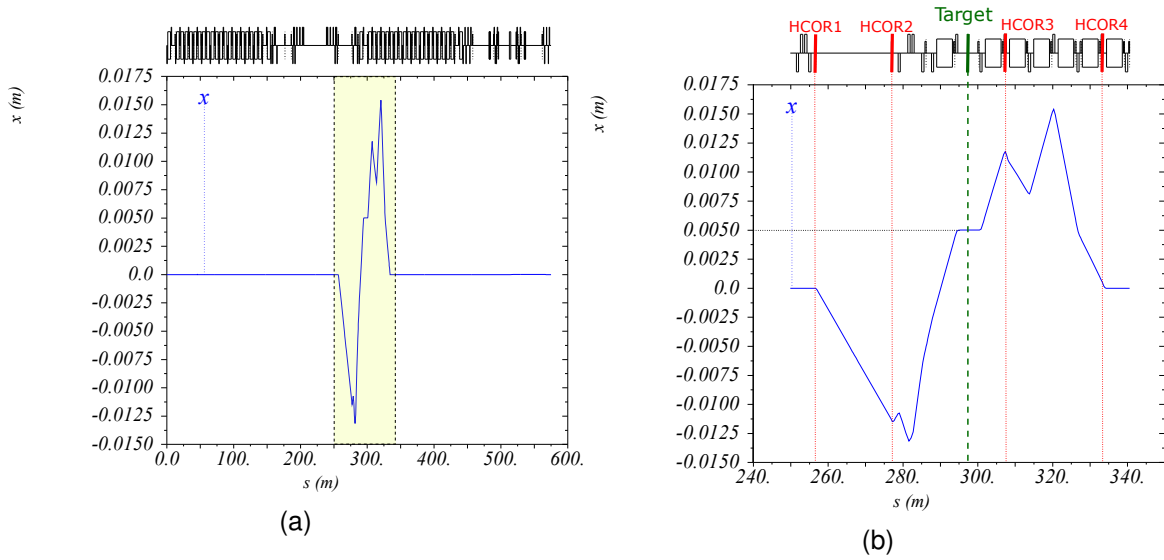


Figure 4.8: The closed orbit bump in the horizontal plane at the internal target location. Plot (b) is a magnified area from the orbit distortion in the plot (a). Its purpose is to show the amplitude and the angle of the orbit in a more precise way.

A similar technique was used for bump creation in the vertical plane with four vertical magnet correctors located around the internal target. For the vertical plane the simulation results are given in the Figure 4.9. The residual orbit deviation in the vertical plane is around

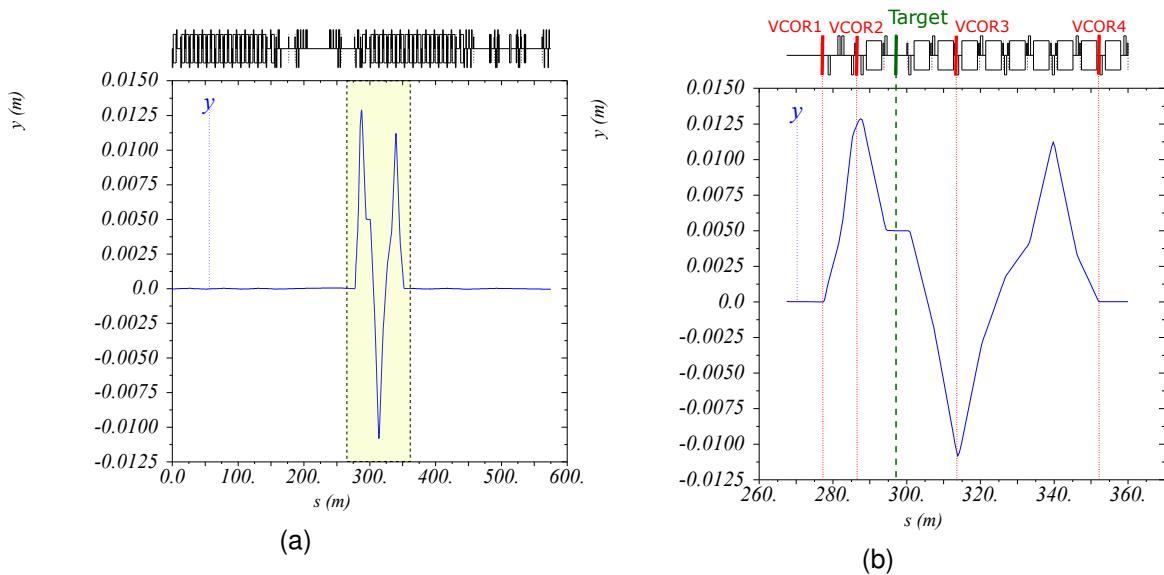


Figure 4.9: The closed orbit bump in the vertical plane at the internal target location. Plot (b) is a magnified area from the plot (a) to show the amplitude and the angle of the orbit more precisely.

13 mm. The corrector strengths in the end did not exceed the technical strength limit of 1

mrad.

As a conclusion, it was proven that with the present layout and strengths of dipole correctors it is possible to create a local bump in both planes in the ± 5 mm tolerance interval. Together with angle adjustment this allows for the perfect beam-target overlap even for the worst-case deviations of the closed orbit at the target location.

4.3 Dynamic aperture (DA) studies

Dynamic aperture shows the largest amplitude of the betatron motion in the presence of nonlinear fields which is still stable for a defined number of turns [11]. The size of the dynamic aperture has a direct connection to the beam lifetime [48]. Thus in order to suppress the instabilities and provide a beam without losses over time one has to care that the dynamic aperture borders are sufficiently large. As a rule of thumb, it should be at least larger than the physical aperture.

4.3.1 Tune scan

The dynamics of the beam depends strongly on the location of the tune working point. The control of tunes increases the dynamic aperture thereby prolonging the beam lifetime and reducing the beam loss.

A common tool which can help in selection of the working point location is the *resonance diagram*. It is a plot showing the resonance lines of different order with the fractional horizontal and vertical tunes on its axes. The Figure 4.10 shows an example of such a diagram with resonance lines up to 4th order. The best tune position is in the regions where there are possibly no resonances. From the Figure 4.10 one can note that the largest resonance-free regions are the triangle-shaped spaces adjacent on both sides to the difference resonance $(1,-1)$, i.e. $Q_x - Q_y = 0$, located in the top right quadrant. When choosing this region one should be careful to maintain the safe distance from the integer and half-integer resonances.

The resonance diagram by itself do not show to what extent a certain resonance is excited by the lattice errors. To inspect the beam dynamics more thoroughly, a special method, called *tune scan*, is employed. The technique is to probe the tune map by changing the horizontal and vertical tunes of the lattice with small step. At each stage we compute and store the dynamic aperture of the given working point. Finally, we identify the tunes at which the dynamic aperture has the maximum value. Since the dynamic aperture size defines the beam stability properties, the tune scan is an excellent technique for finding the best working point for machine operation.

The tune scan was performed with the constraint that the betatron frequencies should be close to the linear coupling difference resonance $|Q_x - Q_y| = n$, where n is integer,

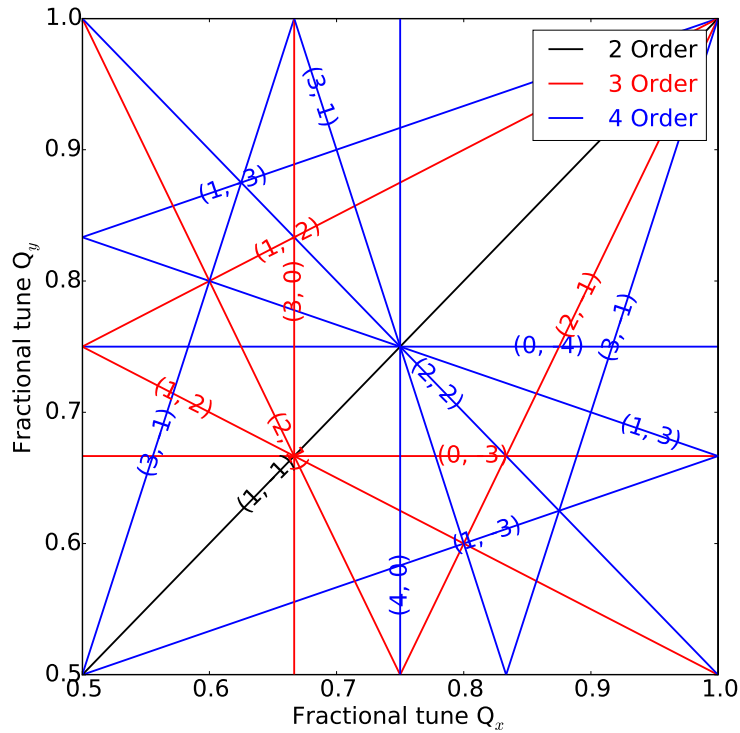


Figure 4.10: Resonance diagram up to 4th order. The black line (1,-1) defines the difference resonance $Q_x - Q_y = 0$.

because of the low density of the machine resonances. This minimized the possibility of overlapping with other resonance lines thereby enhancing the available tune space.

It should be noted that the difference resonance $|Q_x - Q_y| = n$ is to be distinguished from the sum resonance $|Q_x + Q_y| = n$ from the point of view of beam dynamics. In the case of sum resonance the particle amplitudes can grow indefinitely whereas near the difference resonance the amplitude in one plane increases only at the expense of the amplitude in another plane. Therefore for the difference resonance, despite the continuous exchange of motion between the two transverse planes, the amplitudes remain confined.

In Section 4.1.2 in the optics design we were guided by the objectives of relaxing the low-beta insertions, increasing the acceptance and overall reducing the quadrupole strengths. The latter results in smaller sextupole non-linear fields for fighting the chromaticity. The obtained tune working point there was $(Q_x, Q_y) = (6.87, 6.22)$.

Tune working point search. Part 1 In order to provide information which can be used for setting the betatron tune working point, a tune scan for a developed lattice was performed. The computations were done for zero relative momentum deviation $\Delta p/p = 0$.

The full scan procedure consisted of the following iterations:

- With the help of MAD-X matching algorithm, by varying the quadrupole strengths, a certain combination of tunes Q_x, Q_y in the linear lattice was set up;
- After setting the tunes the magnets were randomly misaligned and the errors were introduced in dipoles and quadrupoles. For that a Gaussian distribution with 3σ -cutoff was employed;
- The dynamic aperture is computed in units of $mm\ mrad$ for 100 turns;
- The process is repeated for the next tune combination until the whole tune space is covered between 6.5 and 7.0 for horizontal tune and 6.0 and 6.5 for vertical one.

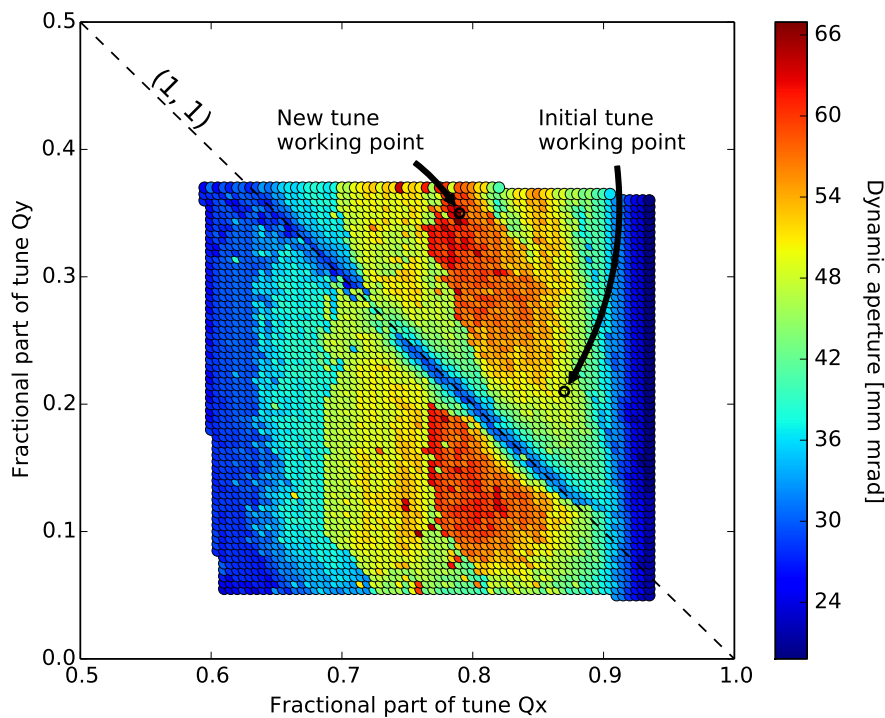


Figure 4.11: Tune scan with the indicated old and new tune working points.

The Figure 4.11 shows the MAD-X computation results with a colorbar representing the value of the dynamic aperture DA calculated as $(DA_x + DA_y)/2$. The initial tune working point was (6.87, 6.21) which appears to be not an optimum solution. From results the largest dynamic aperture is achieved for the tunes (6.79, 6.36).

Tune working point search. Part 2 One important aspect was missed up to now during the tune scan. So far we did not locate the tunes close to the difference resonance, i.e. where the tunes are almost equal. Now we need to fulfill this requirement and change the tune working point location. In the tune span between 6 and 7 the optics matching did not succeed in making the tunes equal thus it was decided to shift to the 5-to-6 tune range. For this purpose optical functions had to be rebuilt starting from the basic FODO cell.

During the design the same sequence of steps was performed as in section 4.1.2. In other words, the first level consisted of configuring the FODO cell phase advance. Then the half-arc was set up. After that the full arc was built. And in the very end the fine tuning was achieved by modulating the quadrupole strengths in the straight sections.

Afterwards, the tune scanning was performed along the linear coupling resonance within a maximum deviation from the resonance line about $\Delta Q = \pm 0.01$. The quadrupoles in the zero-dispersion straight sections were used for fine adjusting of the betatron tune. Therefore the dispersion function was not changed during the matching.

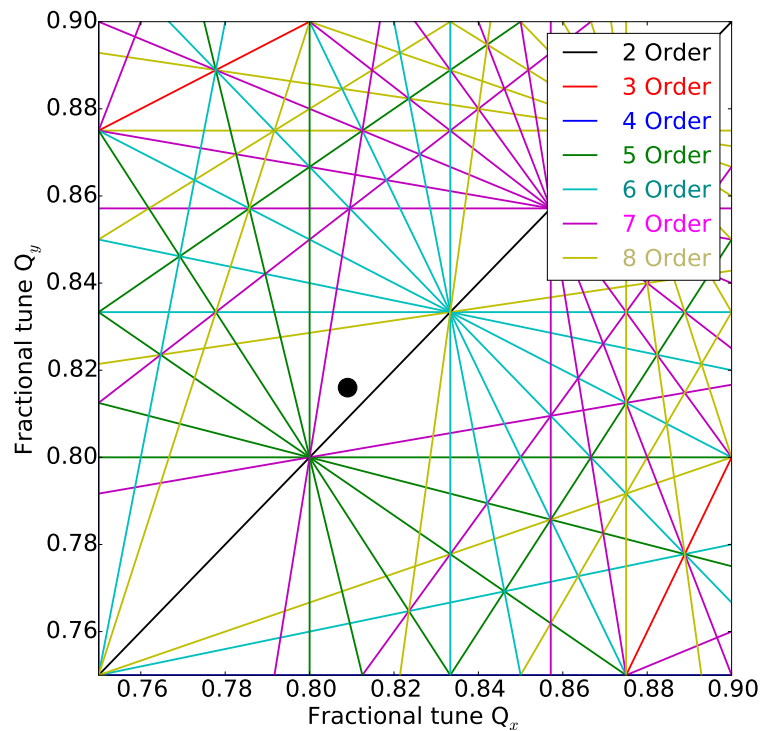


Figure 4.12: Coloured lines represent the resonance lines up to 8th order. The working point $(Q_x, Q_y) = (5.809, 5.816)$ is denoted with a black dot.

After that a more fine analysis was performed which led to the final working point at which the heavy ion machine should be operated. Figure 4.12 shows the tune working point

which was found. The tunes $(Q_x, Q_y) = (5.809, 5.816)$ combine two features: first, its location is appropriate since it finds itself in the vicinity of the main difference resonance, and second, it has the largest dynamic aperture value (see Section 4.3.4 for more details) in the [5; 6] tune range.

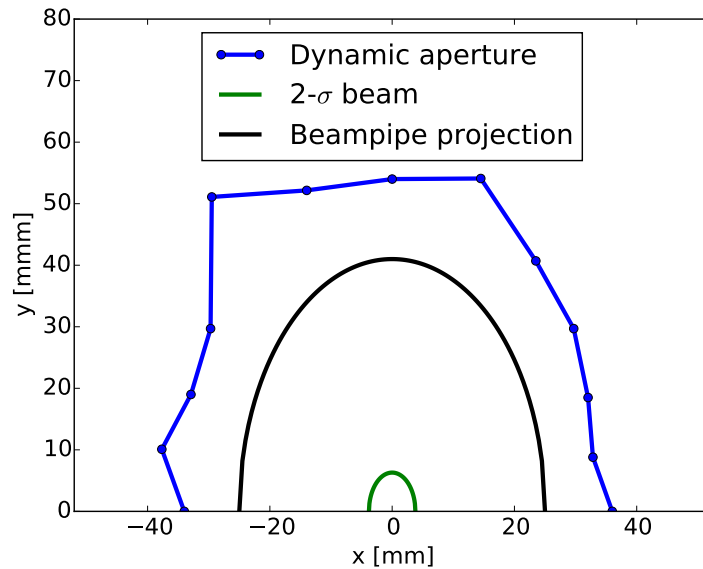


Figure 4.13: Dynamic aperture for the tune working point (5.809, 5.816), physical aperture (denoted as beam pipe projection) and the 2- σ beam are shown.

Figure 4.13 shows the comparison between the dynamic aperture computed after one thousand turns, 2- σ beam and the physical aperture projection. The dynamic aperture size fulfills the most important requirement: it is sufficiently larger than the vacuum chamber aperture which ensures effective use of the internal space of the vacuum pipe .

The corresponding optical functions are plotted in Figure 4.14. The maximum values of β -functions are 91 m in the horizontal plane and 90 m in the vertical plane. It results in the final acceptance value 21.8 mm mrad and 22.0 mm mrad in the horizontal and vertical planes respectively, which is about 4 times larger than in the antiproton ion optics. The averaged dynamic aperture over 100 seeds statistics is close to 16 beam σ .

The calculated transition energy for the ion optics after the tune scan is $\gamma_{tr} = 5.1$. The corresponding frequency slip factor for the injection energy 740 MeV equals $\eta = 0.27$. That means that the stochastic cooling studies, which were carried out earlier for an optics with $\gamma_{tr} = 6.2$ and with the corresponding slip factor $\eta = 0.28$ [45], can still be applied for the current lattice. Table 4.3 summarizes the main parameters of the ion optical layout.

Table 4.3: A list of the parameters of the heavy ion mode optics.

Injection energy, E_{inj}	0.74 GeV/u
Magnetic rigidity range, $B\rho$	[5, 50] Tm
Kinetic energy range, T for $^{238}\text{U}^{92+}$	[0.17, 4.94] GeV/u
Transition energy, γ_{tr}	5.1
Slip factor at the injection energy, η	0.27
Tunes, Q_x, Q_y	5.809, 5.816
Chromaticities, ξ_x/ξ_y	-7.3/-8.4
Maximum beta functions, β_x/β_y	91/90 m
Maximum dispersion, D_x	8.0 m
Transverse acceptance hor/ver	22.5/22.5 mm mrad
Dynamic aperture	15.6 beam σ

4.3.2 DA after chromaticity correction

The chromaticity effect comes from the quadrupoles whose strengths depend on the momentum of the particle. Hence, any lattice introduces the negative chromatic effect since the quadrupole strengths become weaker with momentum increase. If not corrected, the result is the spread in the tunes of the beam which can lead to resonance crossing. Therefore it is essential to reduce the chromaticity to zero in both planes.

The heavy ion optics after the tune scan was investigated in details. The natural chromaticities for the ion optical layout (Table 4.3) in both planes are $\xi_x/\xi_y = -7.3/-8.4$. In order to correct the chromaticity, the sextupoles located only in the non-zero dispersion locations could be used. The 52 sextupoles located in the arcs, where dispersion is not zero, were used for correction. The additional sextupoles, mounted in straights, are employed for non-chromatic purposes – to correct geometric aberrations.

To check the effect of the sextupoles on the dynamic aperture, particle tracking was utilized. The observation point was set in the middle symmetry point in the zero-dispersion straight where the electron cooler is located. Due to the symmetry the alpha-functions at this position were $\alpha_{x,y} = 0$, beta functions $\beta_x = 29$ m, $\beta_y = 79$ m.

Before the tracking the initial slopes x', y' were kept zero while the initial amplitudes

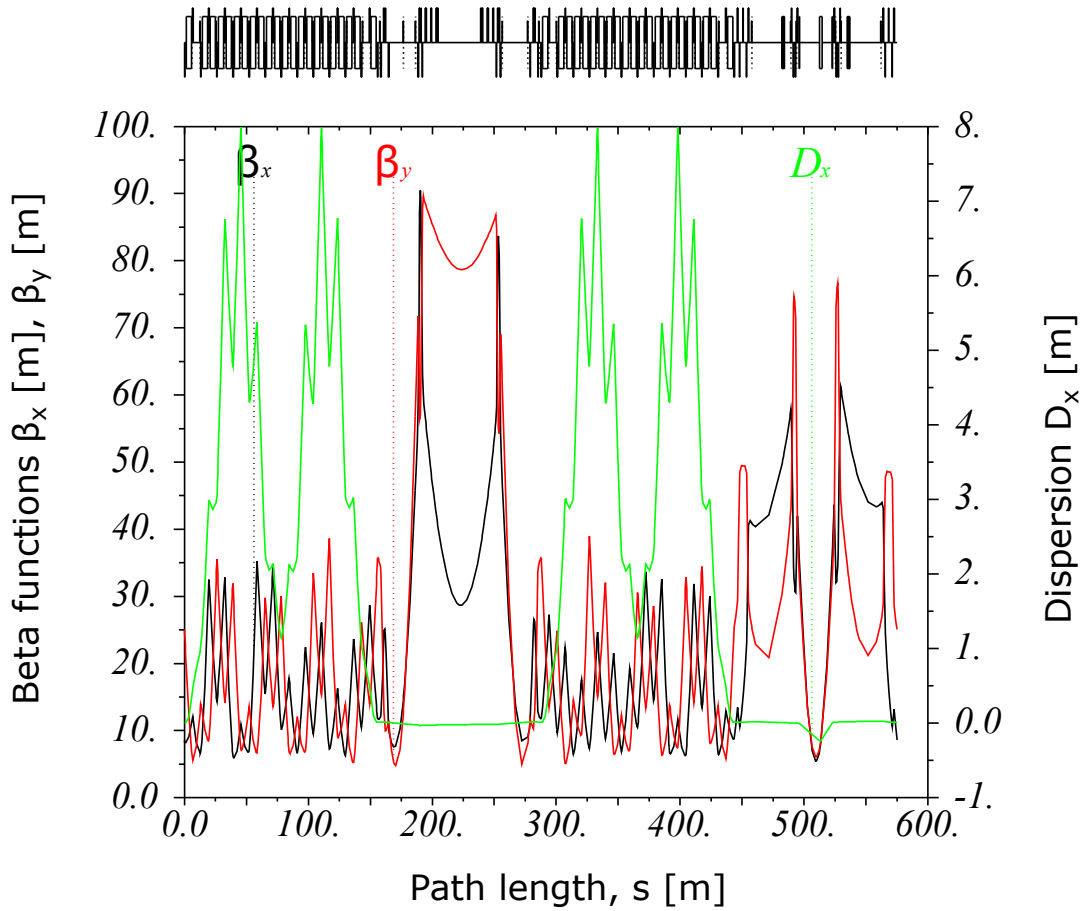


Figure 4.14: Optical functions of the lattice in heavy ion mode (solenoids included in the calculations): horizontal amplitude β_x (black), vertical amplitude β_y (red), dispersion function D_x (green). Path length s [m]: 0-156 m - north arc, 156-287 m - electron cooler, 287-443 m - south arc, 444-575 m - PANDA straight.

x, y were changed with small step until the particle approached the stability border outside of which it became unstable. The number of turns was set to 10000.

The Figure 4.15 shows the comparison of the dynamic aperture measured for the ideal lattice with two and with six sextupole families. Knowing the largest stable amplitude x in horizontal and y in vertical plane the dynamic aperture can be found from Equation (57).

The computations for 50 seeds show that for two sextupole families the DA equals to about 100 *mm mrad* in both planes. For 6 sextupole families the DA is about 4 times larger than for 2 families. It equals to 417 *mm mrad* in horizontal plane and 364 *mm mrad* in vertical plane. The reason for this is that for six families the integrated sextupole strength is in average lower and the sextupoles are more evenly distributed along the lattice than for two families. Thus the introduced nonlinear fields are weaker which leads to more stable motion of the particles.

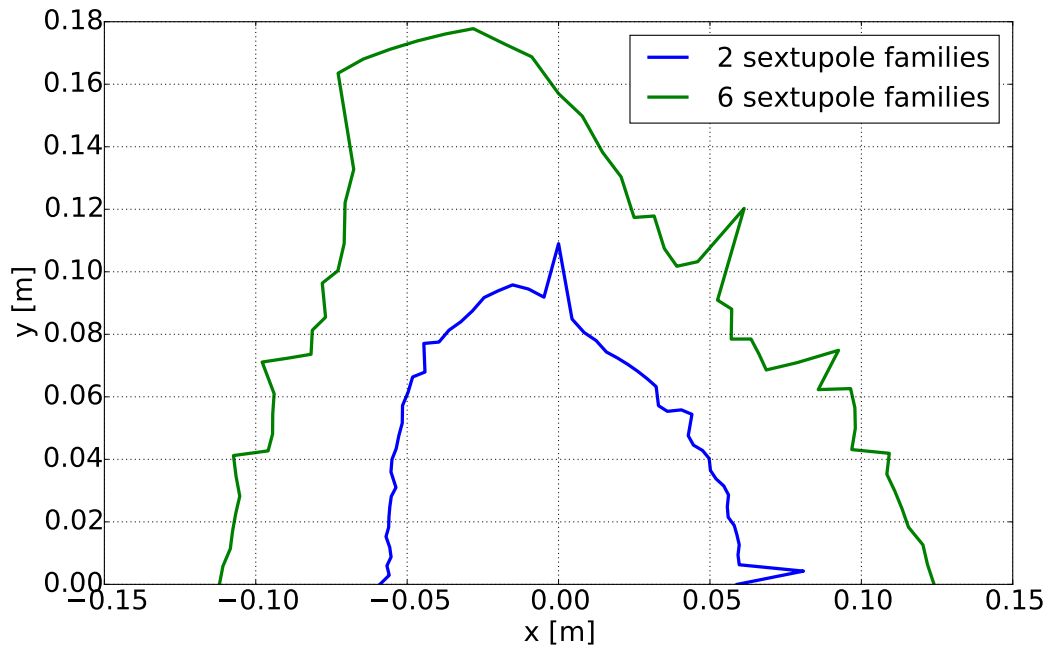


Figure 4.15: Comparison of the dynamic aperture of the ideal lattice after correction with two and with six sextupole families. The calculations were done for 10000 turns. The optical functions at the measurement location were $\alpha_x = \alpha_y = 0$, $\beta_x = 29$ m, $\beta_y = 79$ m.

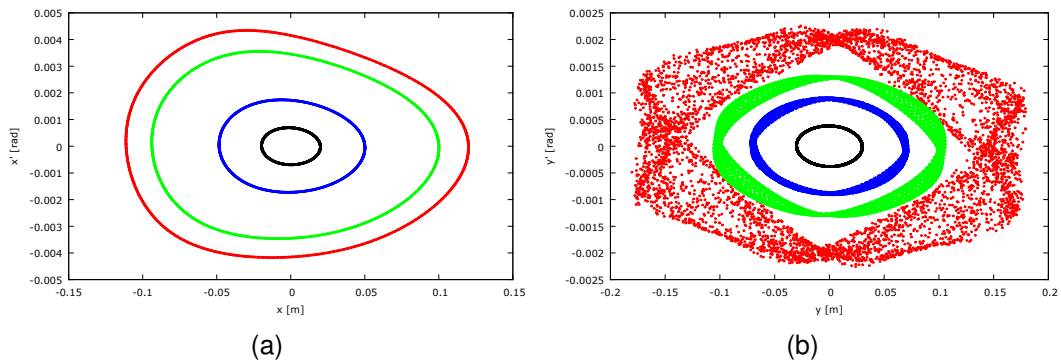


Figure 4.16: Phase space portrait in horizontal plane (a) and in vertical plane (b) for the ideal lattice after chromaticity correction. Six sextupole families, three horizontal and three vertical, were employed. Four colors correspond to four particle initial amplitudes. The red color amplitude defines the border of particle motion stability for 5000 turns. The optical functions at the measurement location were $\alpha_x = \alpha_y = 0$, $\beta_x = 29$ m, $\beta_y = 79$ m.

Phase space portrait of the lattice with six sextupole families is shown in the Figure 4.16. One can see that for the smallest amplitudes the particle follows the perfect ellipses which are Courant-Snyder invariants according to Equation (57). But with increasing of the amplitude the particle trajectory becomes distorted until it crosses the stability boundary.

As a result, with the present quantity and layout of the sextupole magnets the chromaticity at the heavy ion optics was successfully corrected. Six families correction scheme is more preferable because of the significantly larger dynamic aperture.

4.3.3 DA dependence on turns

To check the size of the dynamic aperture with time, the tracking studies for different number of turns was carried out. The MAD-X PTC tracking code was used to perform tracking of particles whose initial coordinates were uniformly spaced in the transverse "x-y" plane. The transverse particles' momenta were zero.

Magnet field errors as well as their fringe fields were taken into account for dipole and quadrupole magnets. Random misalignments were generated for all magnets using gaussian distribution with a cut-off of $\pm 3\sigma$. A closed orbit correction in both planes was applied before the computations.

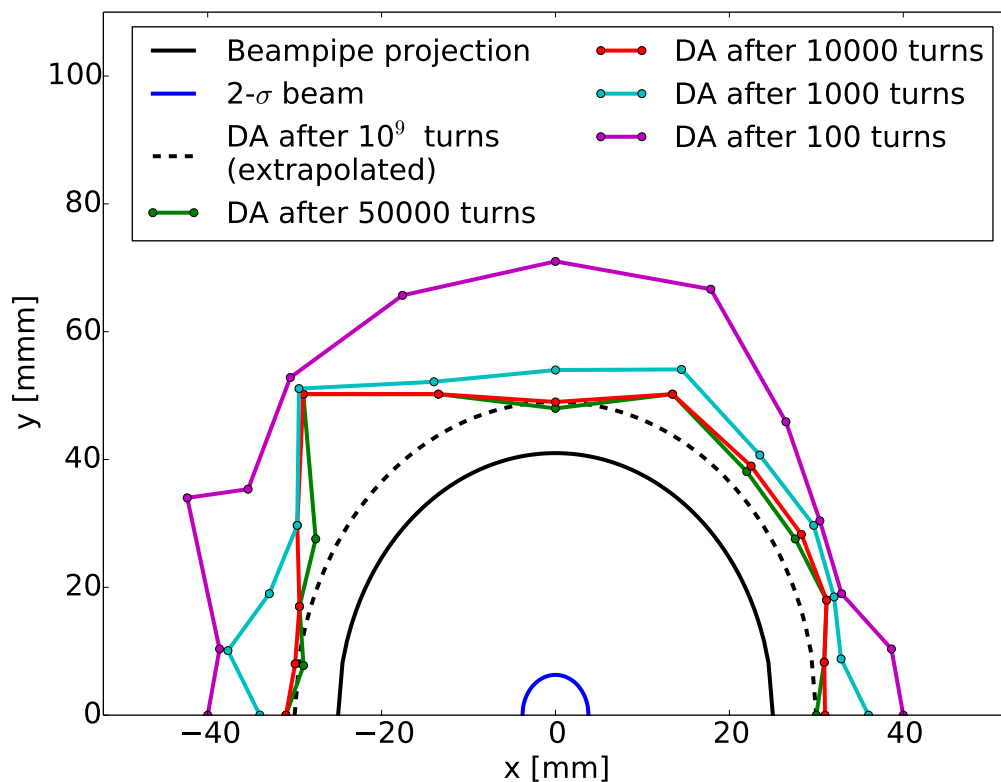


Figure 4.17: Dynamic aperture as a function of number of turns computed for a momentum spread $\Delta p/p = 0$. Dynamic aperture is measured in the location where optics functions are: $\alpha_{x,y} \approx 0$, $\beta_x = 29$ m, $\beta_y = 79$ m. In blue shown a $2\text{-}\sigma$ beam right after injection from CR with the transverse emittance ($2\text{-}\sigma$) $\epsilon_{x,y} = 0.5$ mm mrad (or rms $\epsilon_{x,y} = 0.125$ mm mrad).

Figure 4.17 shows the results of the particle tracking. Several computations were performed for different number of turns ranging from 100 up to 50000. It is possible to extrapolate the dynamic aperture for the larger number of revolutions N with the inverse logarithmic function [49]:

$$D(N) = A + \frac{B}{\log_{10} N}, \quad (112)$$

where A , B are the coefficients obtained after extrapolation. In the Figure 4.17 one can also see a predicted after one billion turns dynamic aperture, which corresponds to about 30 minutes of the beam time in the HESR. Even with such a significant revolution time the long term dynamic aperture is relatively large with a corresponding beam sigma value 15.5σ .

4.3.4 Frequency map analysis

Depending on the type of the experiment, the heavy ion beam may circulate in the HESR for tenths of minutes which corresponds to hundredths million turns. During such a period of time the magnetic field errors can bring a particle to the unstable region. As was already described in Section 2.9.1 the particles with regular motion in the configuration space " $x - y$ " have constant tunes with a stable point in the tune space " $Q_x - Q_y$ ". And on the contrary, in case of irregular motion, it exhibits the tune changes which results in particle "diffusion" in the tune domain. Thus, the conversion, or *mapping*, from " $x - y$ " to " $Q_x - Q_y$ " space should be provided to observe the resonant structure and regions of stability of the system.

Particle tracking studies to determine the border of stability combined with Fourier Transform analysis of the turn-by-turn data can provide valuable insight on the complexity of the dynamics of the beam. It also can give hints for directions in lattice optimization. The FFT analysis applied together with the Hanning windowing to the data, gained after particle tracking, can help to identify the tune shift with the particle amplitude. This reveals the strengths of the nonlinear fields which are felt by the beam [50]. The Hanning filter is of large importance and here is why. The regular FFT has the frequency identification error of $1/N$, where N is the number of turns. The Hanning windowing together with bisection search [51] algorithm⁹ increases the accuracy of frequency search to $1/N^4$. This reduces the number of revolutions needed for tracking to, for example 1024, which appears to be completely sufficient for finding the frequency with great accuracy.

The dynamic aperture was calculated and the frequency map $(x, y) \rightarrow (Q_x, Q_y)$ was constructed via 4D particle tracking and refined FFT analysis [52], which were performed at the GSI computing grid [53]. The computing cluster consists of 380 nodes with 24 cores each – this produces a total number of about 9000 cores.

Each computation unit consisted of the following steps: a set of magnetic field errors

⁹The normal bisection root-finding algorithm is modified here to find the local function maximum

as well as misalignments distributions were generated with unique random seed. The linear optics with the errors was loaded into the MAD-X PTC accelerator code [54] for 2048 turns tracking. The tracking started at the center of the electron cooler. This place was chosen because of the near-zero value of the alpha functions while the beta functions equal there $\beta_x = 29$ m, $\beta_y = 79$ m. The spatial coordinates (x, y) were traced with small step inside a half circle of a large enough radius to embrace the DA area. The slope coordinates were kept constant $x' = y' = 0$. After obtaining a turn-by-turn data, in order to provide mapping from initial coordinates to tune space, for each (x, y) pair after 1024 (2^{10}) turns period a fine frequency search was performed. Thus, after 2048 turns two frequencies were obtained and were used for calculation of *diffusion coefficient* D [55, 56] which is defined as:

$$D = \log_{10} \sqrt{[(Q_x^{(2)} - Q_x^{(1)})^2 - (Q_y^{(2)} - Q_y^{(1)})]^2}, \quad (113)$$

where $Q_{x,y}^{(1)}$, $Q_{x,y}^{(2)}$ are the horizontal and vertical frequencies computed after the first and the second halves of the 1024-turn sample correspondingly. Small diffusion coefficient $D < -7$ indicates a long term stability whereas large $D > -3$ represents an unstable motion [57]. From the experimental evidence [58], particles, which are unstable in the frequency domain, i.e. have a large divergence of the frequency over a short number of revolutions, are more likely to be lost.

Figure 4.18 shows the computation for the lattice obtained after the tune scan with a tune working point $(Q_x, Q_y) = (5.809, 5.816)$. The momentum shift equals to $\Delta p/p = -0.0005$ and it is the minimum possible momentum for the particles in the $2\text{-}\sigma$ beam after injection. The maximum values of the beta functions in the ring were $\beta_x = 91$ m, $\beta_y = 90$ m. From the figure, the motion inside the physical aperture is mostly stable with few perturbations on the edges. When neglecting the small edge disturbance, the main distortion comes from the resonance wedging inside the aperture closer to the top. By identifying it from the tune map (see Figure 4.19) it is a 9th order resonance $7Q_x - 2Q_y = 29$. The unstable red and dark-red areas outside the lattice aperture are due to the vicinity of the linear difference resonance $Q_x - Q_y = 0$. We already showed that this resonance leads only to exchange of motion between the transverse plane but does not lead to particle losses. Hence, these areas do not present any danger and can be reduced by moving the working point slightly far from this resonance.

The dynamic aperture in horizontal plane is 36 mm and in vertical plane it is 52 mm. The emittances which correspond to the computed dynamic aperture are 45×10^{-6} mm mrad in horizontal plane and 34×10^{-6} mm mrad in vertical one. Considering the fact that the acceptance of this ion optical setup is $\approx 22 \times 10^{-6}$ mm mrad in both planes, we conclude that in horizontal plane the dynamic aperture is more than twice larger than the acceptance and in vertical plane it is larger by more than 50%.

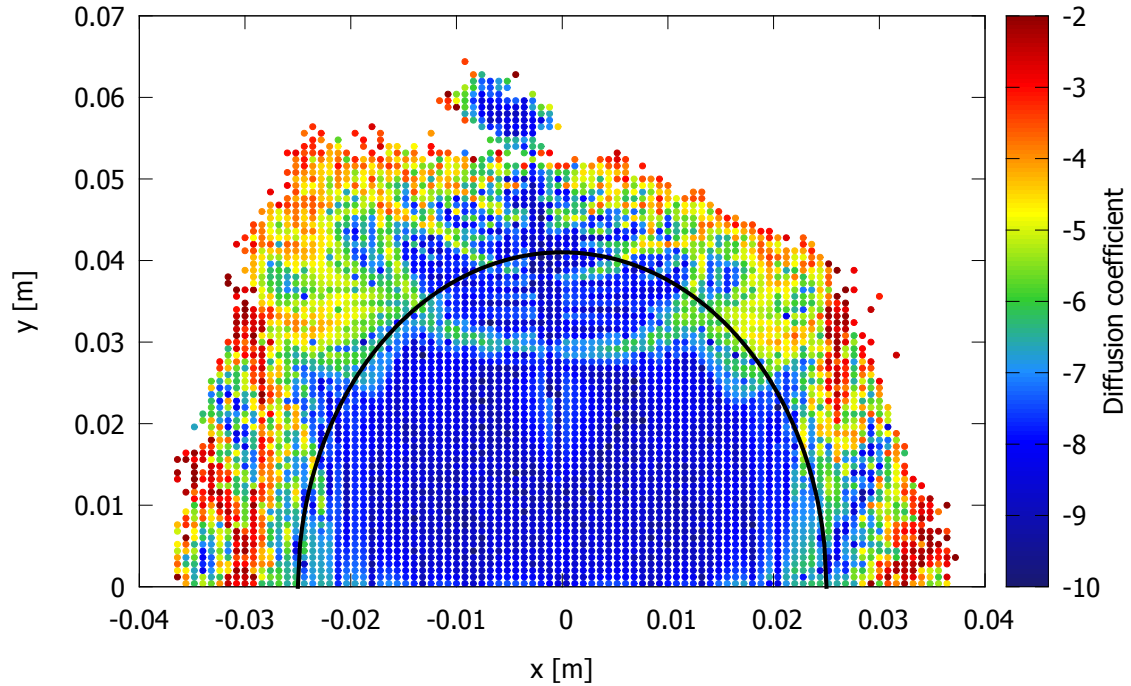


Figure 4.18: Dynamic aperture for $\Delta p/p = -0.0005$ at location with $\beta_x = 29$ m, $\beta_y = 79$ m. The palette bar to the right represents diffusion coefficient, i.e. a measure of chaoticity of particle with given initial coordinates. The dark-blue color represents most stable particle orbits whereas the red indicates high instability and diffusion. The black line denotes the physical aperture projection which is calculated from the $\beta_{x,y}$ -functions values at this location.

Tune map Figure 4.19 shows the main part of the beam internal structure in the frequency domain. The high-order resonant structure, which has most significant impact on the dynamics, consists of five resonances with the lowest 9th order represented by $7Q_x - 2Q_y = 29$ resonance. This is, in fact, the only resonance that disturbs the motion of the particles inside the physical aperture (see Figure 4.18). The other four resonances, which are 10th to 12th order, do not wedge inside the vacuum chamber aperture and thus can be neglected.

Dependence on momentum The momentum spread of the injected into the HESR beam will be in the range $-0.0005 < \Delta p/p < 0.0005$. The frequency map analysis was performed for three values of relative momentum, namely -0.0005 , 0 and $+0.0005$ to cover the whole range. Despite seemingly low values, the momentum spread gives noticeable changes in the beam dynamics in the "x-y" as well as in the " $Q_x - Q_y$ " domains. Let us have a more detailed view.

Figure 4.20 shows the computations in the coordinate "x-y" space. With increase of the momentum the motion inside the aperture becomes more irregular. The two dark-red unstable regions on both sides of the dynamic aperture with -0.0005 momentum deviation

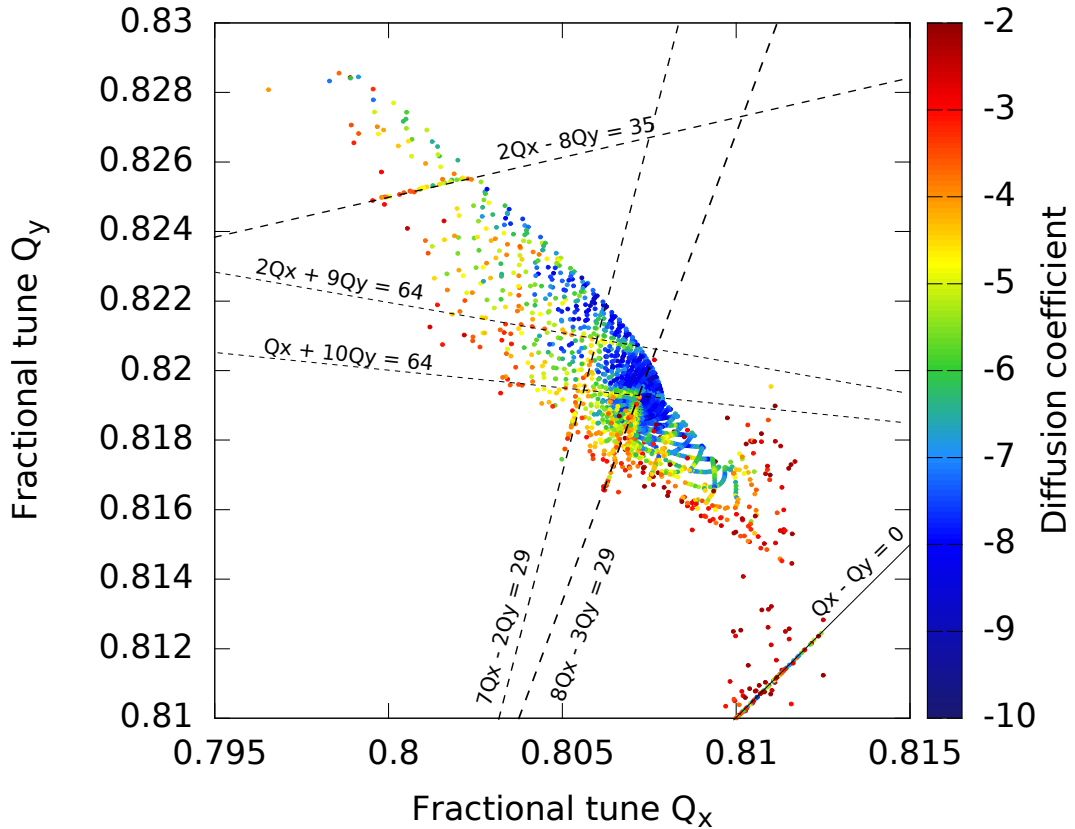


Figure 4.19: Main part of the tune map with fractional horizontal and vertical tunes for $\Delta p/p = -0.0005$. The resonances, those which have an impact on the particles motion, are shown.

(top plot in Figure 4.20) with increase of momentum start to shift to the center thereby creating an unstable region in the core. The frequency map helps to understand the causes of this effect.

The beam dynamics in the frequency domain for three momentum deviations is shown in Figure 4.21. We see that with increase of the momentum the core cluster tends to move closer to the difference resonance $Q_x - Q_y = 0$: at the plot it is a diagonal line with a number of particles attracted to it. Thus, it is the impact of this resonance, which disturbs the motion in the "x-y" coordinate space for the +0.0005 momentum shift in the bottom plot in Figure 4.21. Again, it is a resonance that does not lead to the particle escape and the only effect is the motion exchange between horizontal and vertical planes.

This diffusion tendency results in a transfer of a significant part of the beam to the other side of the difference resonance, from top left to bottom right, to be more precise. Another unfortunate effect of such diffusion is fading out of the resonant structure with momentum increase in coordinate as well as in tune spaces.

If we want to avoid the impact of the difference resonance, the tunes, which are now $(Q_x, Q_y) = (5.809, 5.816)$, should be moved to $(5.81, 5.82)$ or even $(5.81, 5.83)$.

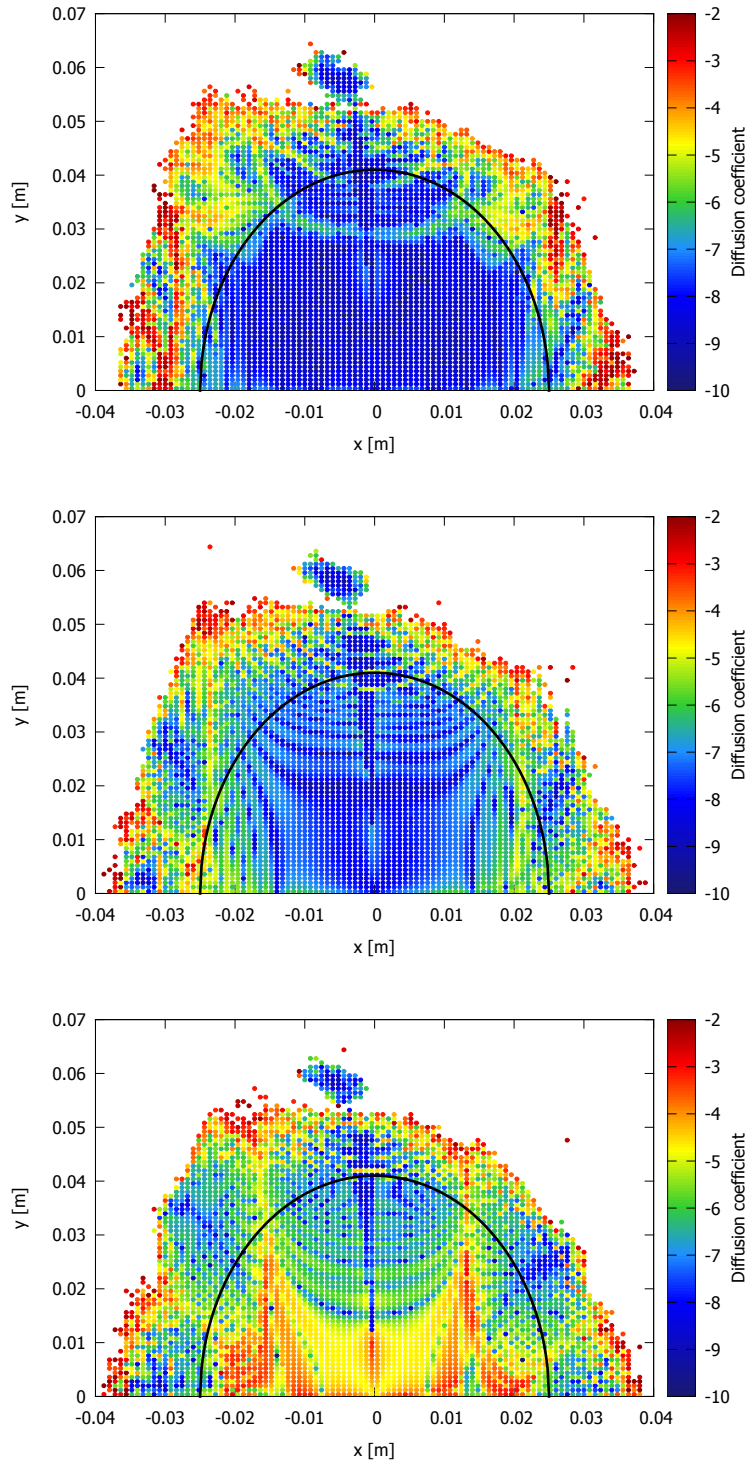


Figure 4.20: Dynamic apertures with diffusion coefficient for momentum shifts $\Delta p/p = -0.0005$ (top), $\Delta p/p = 0$ (middle), $\Delta p/p = 0.0005$ (bottom). The physical aperture projection is denoted with black line. The ion-optical functions at the measurement location are $\alpha_x = \alpha_y = 0$, $\beta_x = 29$ m, $\beta_y = 79$ m.

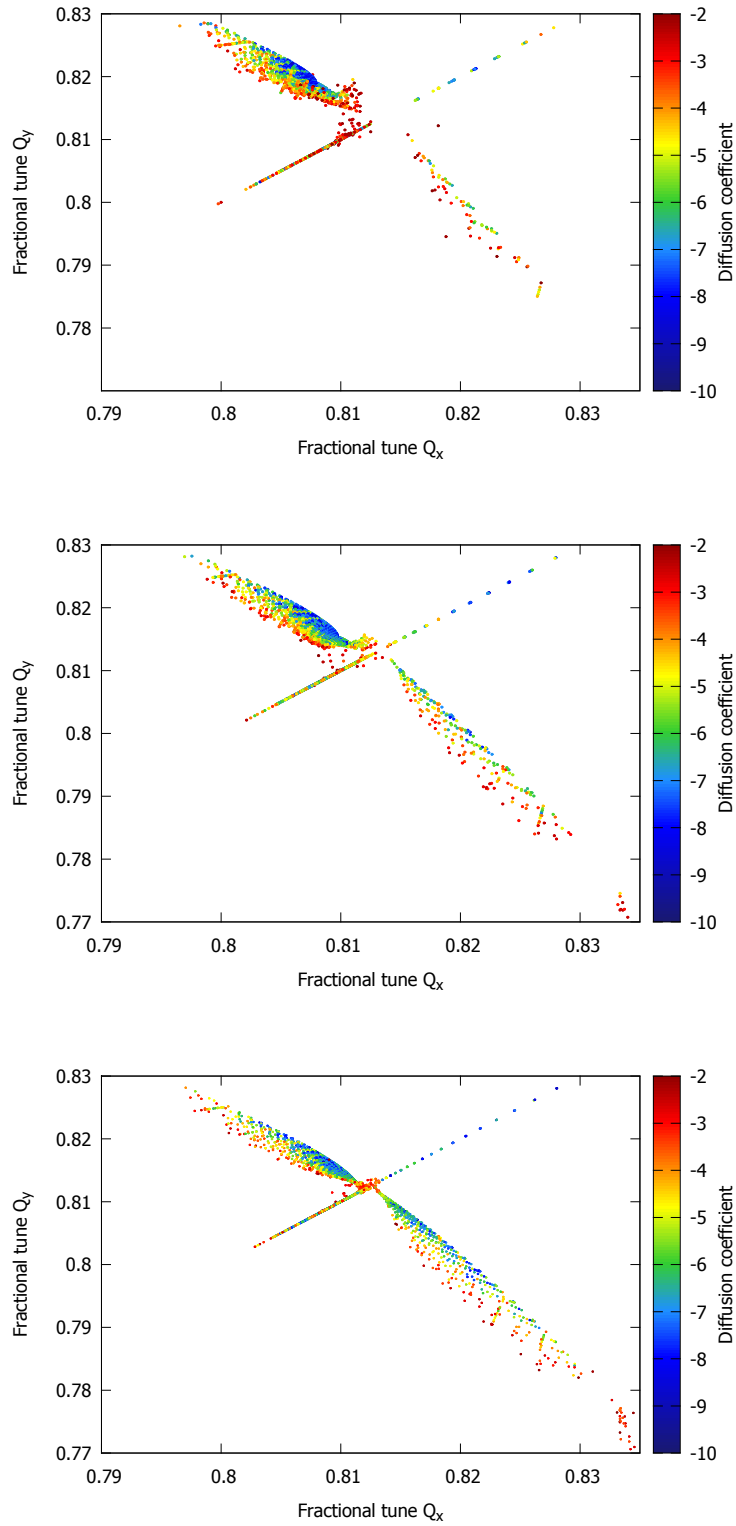


Figure 4.21: Frequency map for different momentum shift $\Delta p/p = -0.0005$ (top), $\Delta p/p = 0$ (middle), $\Delta p/p = 0.0005$ (bottom).

4.4 Space charge tune shift

Space charge is a phenomena which occurs in high-intensity beams due to Coulomb forces between charged particles. It is a collective effect which results in creating of a self-field which defocuses the particles in both planes.

Space charge has to be always accounted for in designing and operating high-intensity proton synchrotrons. The tune spread which occurs due to space charge can cross dangerous resonances. Another harmful effect is the emittance growth which can cause beam losses. Since the heavy ion beams in the HESR can have an intensity of up to 10^9 ions and the energy can go as low down as to 170 MeV, this phenomena had to be investigated.

Space charge in transverse plane acts like a quadrupole, which defocuses in both planes, thus the space charge impact can be considered as merely a quadrupole error. From Section 2.4.2 any quadrupole error in the lattice affects the beam by introducing an additional tune shift to the particles tunes. Consequently, the most important effect of the space charge is an extra tune variation.

There are coherent and incoherent tune shifts. The difference is that the first relates to the beam as a whole by adding the same tune shift value to all the particles. The second, namely incoherent tune shift, is an individual change in betatron tune which is different for different particles. This leads to a tune spread, i.e. the beam in the frequency domain becomes smeared over a certain area. The coherent tune shift can be easily compensated by adjusting the quadrupoles whereas the same cannot be done for the incoherent tune shift.

In case of too large tune spread, the particles can hit the half integer or even whole integer resonances and eventually are lost from the beam. Thus the goal is to estimate the space charge impact in the HESR by its analytical calculation.

The incoherent tune shift due to transverse direct space charge is calculated with the following equation [59,60]:

$$\Delta Q_{x,y} = -\frac{r_0}{\pi} \left(\frac{q^2}{A} \right) \frac{N}{\beta^2 \gamma^3} \frac{F_{x,y} G_{x,y}}{B_f} \frac{1}{E_{x,y} \left(1 + \sqrt{\frac{E_{y,x} Q_{x,y}}{E_{x,y} Q_{y,x}}} \right)}. \quad (114)$$

Here $F_{x,y}$ is a parameter calculated from the geometries of beam and the vacuum chamber. $G_{x,y}$ is a parameter defined from the beam distribution – for Gaussian beam it equals 2. B_f is the bunching factor which equals to 1 for coasting beam and < 1 for bunched beams. $r_0 = 1.54 \times 10^{-18}$ is the classical particle radius for proton; $q = 92$ is the ion charge state; $A = 238$ is the mass of the ion; $N = 10^8$ is the number of particles in a beam; $E_{x,y}$ is four times rms-emittance or $4 \times \varepsilon_{x,y,rms}$; β is beam velocity; γ is relativistic factor; $Q_{x,y}$ is tune in horizontal or vertical planes.

The Equation (114) gives an inverse dependence of the betatron tune shift on the

cube of beam energy. This means that the space charge is much more dangerous at low energies. For the HESR the lowest achievable energy is defined by the minimum magnetic rigidity $B\rho = 5 \text{ Tm}$ and the corresponding energy for bare uranium beam equals 170 MeV.

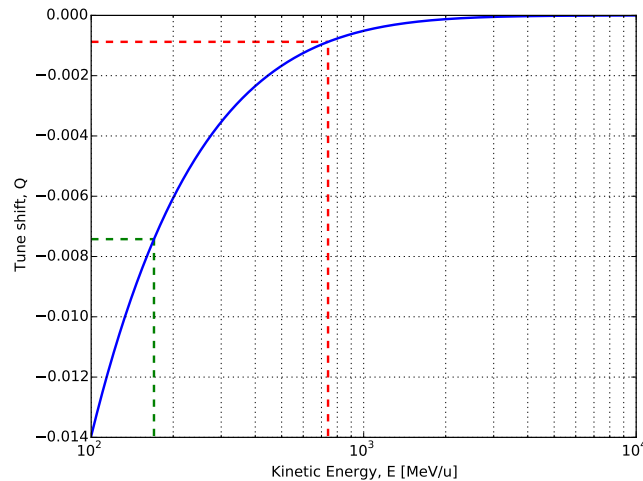


Figure 4.22: Incoherent tune shift due to transverse direct space charge is plotted against the kinetic energy of the beam. The green dashed line shows the minimum achievable energy for bare uranium ions at the HESR which equals 170 MeV and the corresponding tune shift value 0.8×10^{-3} . The red dashed line denotes the injection energy 740 MeV with the corresponding tune shift of 7.4×10^{-3} .

The minimum 170 MeV as well as the injection 740 MeV energies are marked in Figure 4.22 where the tune shift as a function of beam energy is calculated. From the plot, the tune variation for the injection energy due to space charge is expected to be less than 10^{-3} , which is totally negligible. However, the minimum 170 MeV kinetic energy corresponds to almost 0.01 betatron tune shift. In comparison to the values of the tune variation due to amplitude dependence from Section 4.3.4, the tune spread from the space charge at minimum energy is too large to be neglected and should be taken into account during beam deceleration.

Also note that there is an inverse dependence of the tune shift on the transverse emittance. Therefore, if the beam emittance is decreased due the beam cooling, it can potentially enhance the space charge tune shift – this might require special attention at the time of beam commissioning with cooling.

4.5 Charge state separation

Some of the SPARC collaboration experiments will depend on detecting of the recoiling ions after interaction with target nuclei. An example of such an experiment is a study of so called Negative Continuum Dielectronic Recombination [61, 62] or simply NCDR. It is a process in which a projectile ion captures a quasi-free electron from the target. If the ion energy is high

enough than instead of a photon emission the energy is converted to an electron-positron pair creation. Thus via a recombination of a bare nucleus with a quasi-free electron we obtain a down-charged Helium-like ion with a free outgoing positron. In order to catch the outgoing Helium-like uranium ions with a particle detector, these ions should be separated from the primary beam of bare ions, which is done with downstream-located dipole magnets.

The most important questions to the developed ion optics with regard to the experiment were:

- Is it possible to separate the charge states with the designed ion optical layout and planned beam characteristics?
- How many bending magnets are required for the separation of the charge states?
- Do the created down-charged ions perform a full revolution in the ring without hitting the aperture? If not, at what point of the beamline after the target will they be lost?
- Where do the particle detectors have to be located for the charge states to be completely separated?

The answers to these questions were given in this part of the study.

A hydrogen gas-jet target is foreseen as an internal target for the SPARC physics experiments. Two different target positions are discussed in this section. By far the most accepted location is the drift space in the south-west arc, which is denoted as "Location 1". In addition a location in the north-west arc, denoted as "Location 2", is inspected here in terms of charge state separation downstream the beam line.

An electron-cooled bare uranium beam together with down-charged H-like and He-like uranium ions are modeled using MIRKO simulation program [8]. The rms values which describe the properties of the injected beam are as follows: the horizontal and vertical emittances are $\varepsilon_x/\varepsilon_y = 0.125/0.125 \text{ mm mrad}$, the relative momentum spread is $\Delta p/p = 5 \times 10^{-4}$ [40]. The interaction of the beam with target as well as intra-beam scattering lead to the emittance blowup. These processes are counteracted by applying the electron cooling [38] together with barrier voltage. The latter compensates the mean energy loss coming from the interaction with a target. The final equilibrium value of the horizontal emittance, which is $\varepsilon_x = 0.25 \text{ mm mrad}$, is slightly larger than that of the injected beam whereas the vertical emittance does not increase so heavily and equals $\varepsilon_y = 0.15 \text{ mm mrad}$. The momentum spread is decreased by one order of magnitude to $\Delta p/p = 5 \times 10^{-5}$. The described beam properties of the injected beam and during the beam cooling are shown in Table 4.4.

The target locations and the investigated regions of interest (ROI) are shown in Figure 4.23. The beam with both target and electron cooling turned on is simulated and the results are presented in horizontal plane, exactly where the charge state separation takes place because of the horizontally bending magnets.

Table 4.4: Comparison of the beam parameters of the injected beam and after electron cooling. All rms values.

	After injection	Target + electron cooling
Relative momentum spread, $\delta p/p$	5×10^{-4}	5×10^{-5}
Horizontal emittance, ε_x	0.125 [mm mrad]	0.25 [mm mrad]
Vertical emittance, ε_y	0.125 [mm mrad]	0.15 [mm mrad]

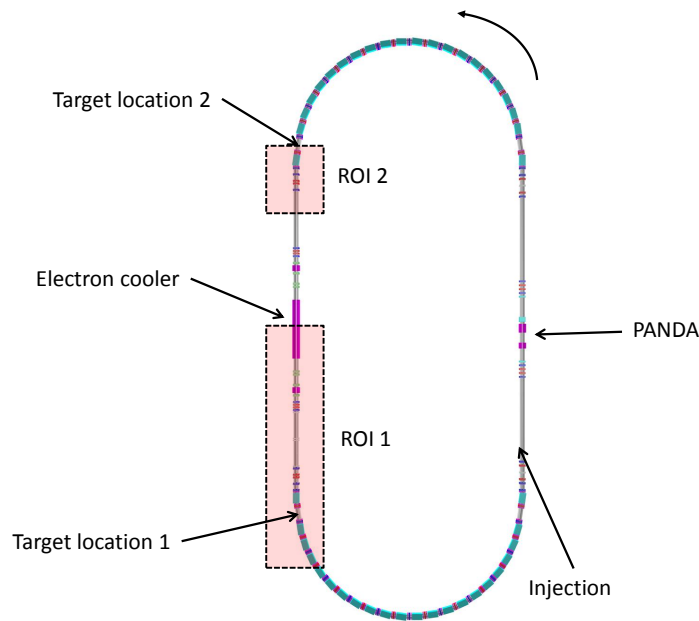


Figure 4.23: Two target locations and the corresponding regions of interest (ROI) are shown. The latter are highlighted with red transparent rectangulars. The motion of the beam is counter-clockwise which means that in the HESR west part the beam moves from the top to the bottom.

4.5.1 Location 1. Target in the south-west arc

A part of the beam line with a SPARC target in the west-south section of the HESR with the $2\text{-}\sigma$ beam, which gives in two dimensions more than 90 % of particles [11], is modeled. The emittance of the beam is taken as the equilibrium one from the counteracting target interaction and electron cooling and equals $\varepsilon_{x,y} = (0.25, 0.15) \text{ mm mrad}$. The horizontal and vertical beta functions at the target locations are equal $\beta_{x,y} = 18 \text{ m}$ and correspond to the 4.2 mm radius or 8.4 mm diameter for the $2\text{-}\sigma$ beam .

It is assumed that via charge exchange reactions such as, e.g. radiative electron capture (REC) and negative continuum dielectronic recombination (NCDR), the respective Hydrogen-like and Helium-like uranium ions are obtained. Also for this position of the target the down-charged ions, coming as a result of the radiative recombination (RR) reaction with the free electrons in the upstream-located electron cooler, should be taken into account.

With the internal target positioned exactly in the middle of the drift space, the simulated main bare uranium beam and the ions from the charge exchange reactions from the target and electron cooler are shown in the top plot of Figure 4.24. As can be seen, the charged exchanged reaction products from the target, such as H-like and He-like ions, are lost in the fourth dipole of the arc. In the second and third dipoles the ion distribution is too wide because of the large β_x -function. Also at this point the charge exchange ions are not bent sufficiently outwards by the dipoles. As a result, they cannot be resolved to the desired extent in the locations of the second and third dipoles. The perfect location for the particle detector is just before the fourth dipole where the beta function in the horizontal plane has its minimum value $\beta_x = 7$ m which corresponds to a diameter of a $2\text{-}\sigma$ beam slightly more than 5 mm. Thus, if the particle detector placed before the fourth dipole, the resolved particle distributions (bottom plot in Figure 4.24) do not overlap and are well separated with safe interjacent gaps.

The critical point is that the H-like uranium ions, coming from the ion-electron recombination in the electron cooler, interfere with the He-like ions from the target at the detector location, as shown in Figure 4.24. If this poses a problem during the experiment, the ion optical functions should be accordingly adjusted.

4.5.2 Location 2. Target in the north-west arc

As an alternative, another location for the internal target in the drift space in the north-west part of the ring (see Figure 4.23) is investigated. The advantage of this position, in comparison to the south-west arc, is the absence of the electron cooler upstream the target. Therefore we do not obtain the contaminating ions coming from the electron-ion recombination in the electron cooler. This results in much more clean experimental conditions.

In order to model the ion beam, the same techniques, lattice and beam properties were applied as in the previous Section 4.5.1. Left plot in Figure 4.25 shows the uranium beam separation of the main beam and two charge states obtained after the target. In spite of the fact that there is only one bending magnet which is available for the separation, the simulation shows that it is still enough to resolve the uranium charge states.

The right plot in Figure 4.25 shows a clear separation of the charge states for the position of the detector around 3 m from the last defocusing quadrupole. The horizontal beta function has a local minimum value at this point $\beta_x = 7.5$ m which corresponds to the

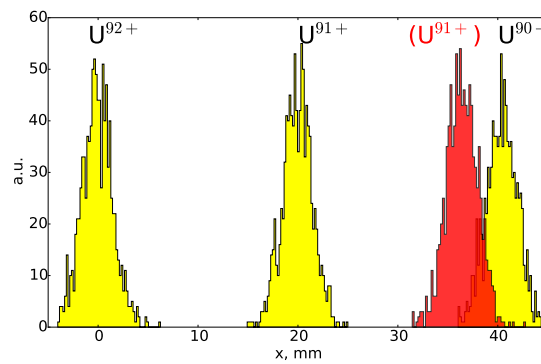
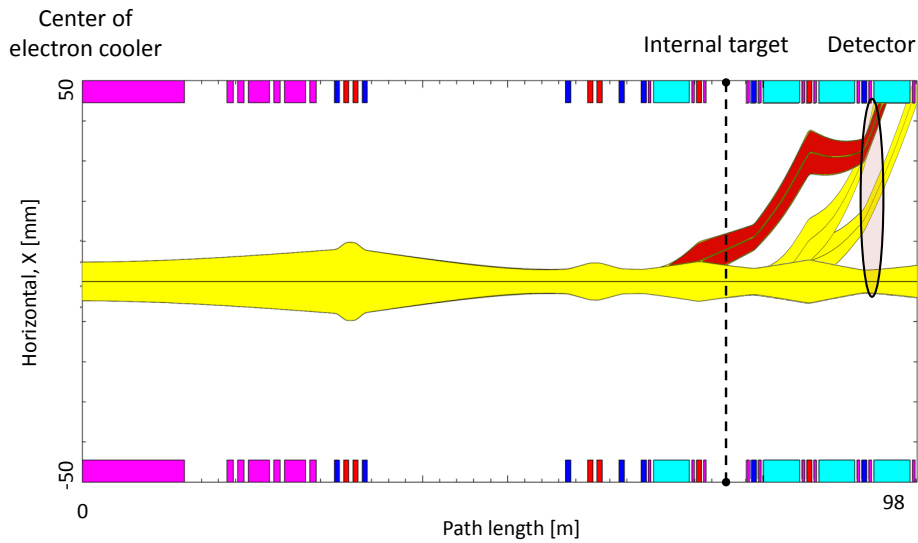


Figure 4.24: The top plot shows the propagation of the bare uranium beam after the electron cooler with H-like and He-like ions from the target charge exchange reactions, which are shown in yellow. In red color one can see the Hydrogen-like uranium ions coming as a result of the electron-ion recombination in the electron cooler. The dipoles, focusing and defocusing quadrupoles are represented with, respectively, cyan, red and blue rectangles. The bottom plot shows the particle distributions obtained at the detector. The yellow peaks correspond to the main bare uranium beam and to the charge exchange reaction products from the target. Red denotes the H-like ions coming from the radiative recombination in the electron cooler. Remark: the ratios between the peaks do not correspond to the real intensities. The purpose is to show the transverse position and the distribution width of the corresponding ions in the particle detector.

5.4 mm diameter of the $2\text{-}\sigma$ beam.

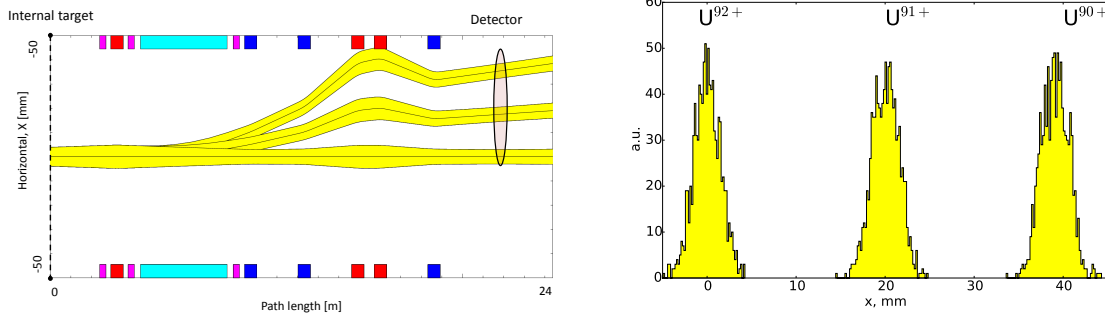


Figure 4.25: The left plot shows the propagation of the bare uranium beam after the electron cooler and its charge exchange reaction products after the interaction with the target. The right plot shows the particle distributions obtained at the detector. The yellow peaks correspond to the main bare uranium beam and the charge exchange reaction products from the target. Remark: the ratios between the peaks do not correspond to the real intensities. The purpose is to show the transverse position and the distribution width of the corresponding ions in the detector.

Adiabatic damping Let us show how the transverse emittance varies with energy. In the phase space, either horizontal or vertical, the vertical axis represents the trajectory slope or the transverse momentum normalized to the longitudinal one. Therefore during the change of particle energy its transverse emittance is changed proportionally to factor $\beta\gamma$. For instance, in case of acceleration, during which the emittance shrinks, this is called *adiabatic damping*.

Since the magnetic rigidity of the HESR allows for an acceleration of the bare uranium beam up to 4.94 GeV/u the emittance will be smallest at the maximum energy. To make a comparison with the injected emittance $\varepsilon_0 = 0.5 \text{ mm mrad}$, the emittance ε_1 at the highest energy 4.94 GeV/u will be:

$$\varepsilon_1 = \frac{\varepsilon_0 \beta_0 \gamma_0}{\beta_1 \gamma_1} = 0.12 [\text{mm mrad}], \quad (115)$$

where β_0, γ_0 and β_1, γ_1 are the velocity relative to speed of light and the Lorentz factor for the injection energy 740 MeV and for the maximum energy 4940 MeV respectively. The beam size due to betatron motion scales as square root from emittance (see, e.g. Equation (81)). Thus the beam, when accelerated to almost 5 GeV, will be about twice as smaller as the injected beam – it additionally improves the separation quality.

5 Experiment with uranium beam at the ESR@GSI

5.1 ESR overview

The ESR storage ring at GSI in Darmstadt [63] can accelerate a broad range of ions from helium up to bare uranium. It has a lot of similarities with the HESR: for instance, electron and stochastic cooling, large diversity of ions for acceleration, internal gas-jet target experiments etc.

The ion velocities in the ESR are in the range $\beta \in [0.1; 0.9]$. The vacuum pressure of about 10^{-11} mbar provides minimum collision rate between circulating ions and the atoms of the rest gas. The electron and stochastic cooling systems control the beam size in 6D phase space. The equilibrium parameters of the beam during the cooling are for emittance $\varepsilon_{x,y} = 0.1 \text{ mm mrad}$ and for energy spread $dE/E \approx 10^{-4}$. At maximum, about 10^8 particles can be stored in the machine at once. The circumference of the ESR storage ring at GSI is 108.36 m. The maximum magnetic rigidity $B\rho = 10 \text{ Tm}$ allows for storage of the U^{92+} ions at the energy of about 555 MeV/u.

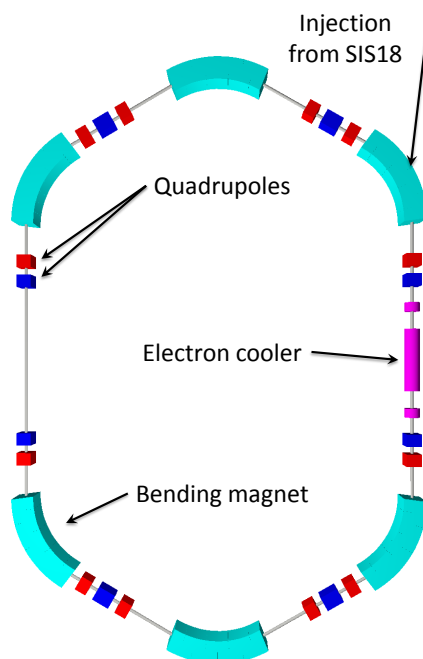


Figure 5.1: General layout of the ESR storage ring.

The Figure 5.1 shows the ring geometry with the positions of the injection point from SIS-18 synchrotron, lattice magnets and electron cooler.

At the time of our experiments the RF voltage was equal to 100 V with the RF harmonic

set to $h = 2$. This resulted in two bunches, each of about 10 m length, circulated in the ring. The cooling was achieved with the current in the electron cooler set to $I = 250 \text{ mA}$ which corresponds to the density 3.8×10^6 electrons per cm^3 [64].

5.1.1 Isochronous optics

The storage ring was operated in the isochronous regime¹⁰ which means that the energy of the beam equals to the transition energy γ_t and the phase slip factor η is zero. The corresponding, isochronous, ion optical layout was set during the experiment.

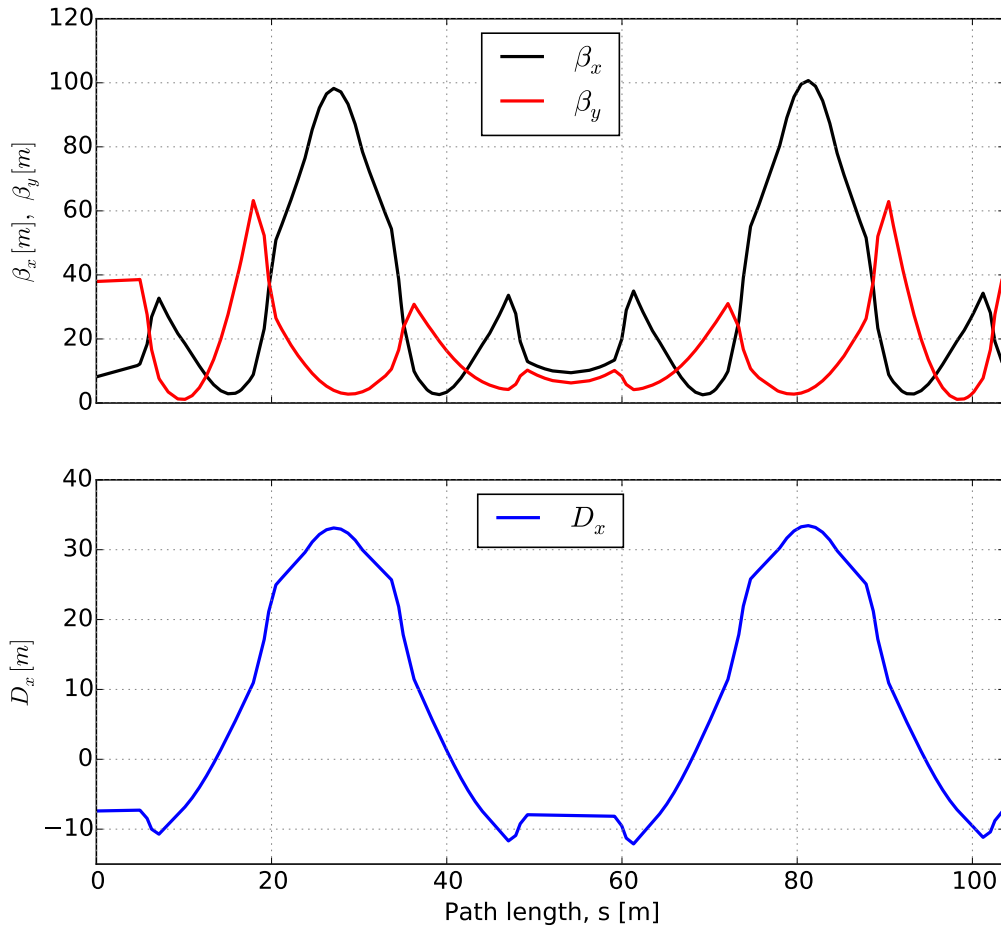


Figure 5.2: Ion optical functions of the ESR in the isochronous mode.

The ion optical functions for the isochronous lattice are plotted in Figure 5.2. As can be seen from the plot, the dispersion does not equal zero in the straight section. That

¹⁰This mode of a storage ring is employed for the mass spectrometry

is, of course, not a desirable condition but rather a forced one because of the following reason. The standard optics mode of the ESR is characterized by the value of γ_f which is much higher than the available beam energies in the ring. Therefore we need to lower the transition energy by changing the dispersion function to reach the $\gamma = \gamma_f$ condition. Since it was not possible to sufficiently lower the dispersion in the arcs, the only way out was to lower it in the straight sections. Thus, if initially the dispersion in the straights was zero, in the isochronous optics it is set to negative values.

From the Figure 5.2, the maximum value of dispersion function in the arcs reaches 33 m. The maximum horizontal beta function is about 100 m whereas the vertical one reaches the value of 63 m. The betatron tune working point during operation was equal to $(Q_x, Q_y) = (2.30, 2.42)$.

5.2 Experiment. Dispersion measurement

In this section the process of finding the dispersion function of the isochronous ESR lattice is described.

The deviation of the beam, which has a relative momentum shift $\Delta p/p_0$, from the reference orbit is defined:

$$x = x_0 + D_x \frac{\Delta p}{p_0} \quad (116)$$

Here x_0 is the reference closed orbit for the particle with design momentum p_0 which is defined by the dipole field components such as those from steerers or dipole errors from magnet misalignments or field imperfections. D_x is the dispersion function at the ring location where the measurement of the beam deviation takes place. Knowing the magnetic rigidity $B\rho$, the design momentum p_0 is computed from the Equation (6).

Helium-like U^{90+} ions were used as a primary beam. The magnetic rigidity, defined by the dipole field, during the experiment was set to $B\rho = 7.621$ Tm. It corresponds to the energy of the ions 339.0 MeV/u. The energy of the electrons in the E-cooler is adjusted to have the same velocity with the corresponding energy 185.97 keV.

The energy of the beam was changed step by step with the help of the electron cooler while keeping the dipole guiding field constant. The energy of the electrons was varied in the [185.65; 187.10] keV range which relates to the [338.69; 341.06] MeV range for ions. The velocity defined by this energy range has a value of about $\beta \approx 0.68$. At each step, a few second time was waited out during which the ion beam was thermalized via electron-ion Coulomb interaction and eventually started to circulate with the same speed as the electrons in the cooler. Afterwards, the readout of the BPMs for the beam amplitude values was carried out. The uniformly distributed along the ring 12 Beam Position Monitors (BPM) were used for this purpose.

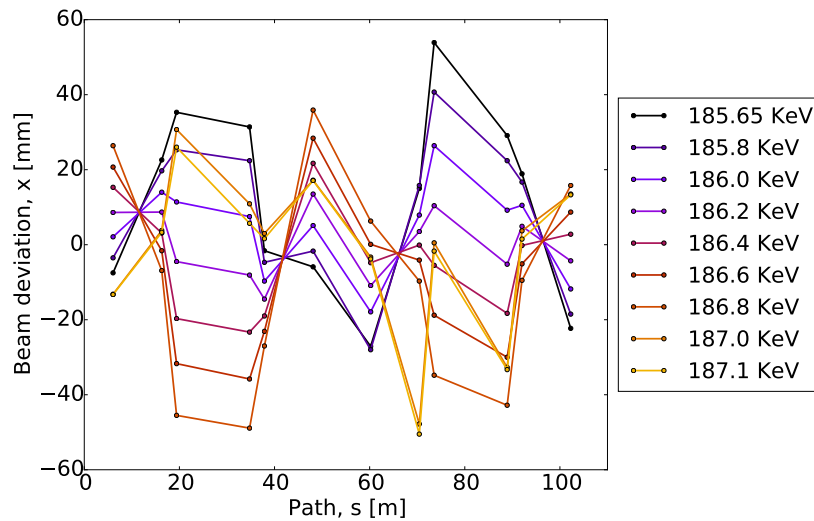


Figure 5.3: The beam deviations for the electron energy range [185.65, 187.1] keV is shown. Each line denotes the beam deviation at the beam position monitors for the given energy, with black for the minimum and yellow for maximum energy value.

The results of the measurements are shown in Figure 5.3. The beam deviation was measured in total for 9 values of the electron energies. The energies outside the [185.65, 187.1] keV interval were not accessible because of the complete beam loss outside the above defined limits. Therefore, the above established energy range is the *energy acceptance* of the isochronous ion optics.

From Figure 5.3 one can observe an abnormal behaviour of the beam at the two energy values, 187.0 keV and 187.1 keV, for which the amplitude values fall out of the trend. It becomes more clear when we plot the beam deviation as a function of the cooler energy only for one monitor. The first BPM, located at $s = 6.05$ m, is taken as an example. We also add the transition energy to the plot.

The Figure 5.4 shows the corresponding dependence. The E-cooler energy during the experiment was constantly being increased. From the figure it is clearly seen that the beam amplitude monotonously grows up with energy until 186.8 keV, but at 187.0 keV and 187.1 keV the beam positions drop down extremely. Taking into account the transition energy value of 186.85 keV, it means that the last two measurements of the beam amplitude, which fall out of the general trend, were performed just after crossing the γ_{tr} . A similar dependence, as in Figure 5.4, is obtained for other beam position monitors. Another point is that the beam positions in the vertical plane virtually did not vary while changing the cooler energy during the experiment. And only for the two energies above the transition the monitors showed inconsistent non-physical beam positions which deviated to an extent of 10 mm.

The explanation, why the beam position monitors give the wrong values, can be as

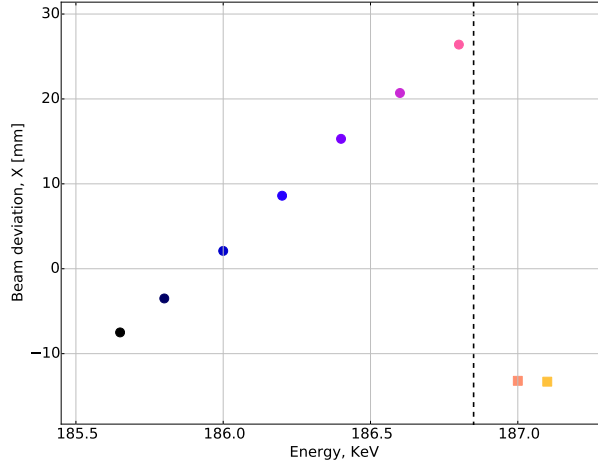


Figure 5.4: The beam amplitude at the first BPM as a function of the E-cooler energy is shown. The BPM is located at $s = 6.05$ m. The two values, denoted with filled squares, correspond to the energies 187.0 keV and 187.1 keV. The transition energy $\gamma_{tr} = 186.85$ keV is shown with dashed line.

follows. It is known from the longitudinal dynamics [44] that the transition crossing gives rise to several effects such as e.g. head-tail, negative mass, microwave instabilities. This disturbs the synchrotron motion in the RF bucket and destroys the longitudinal auto-focusing. The result is that the RF system, which was turned on during the experiment, could not any longer fulfill its function. Consequently, the bunched beam uniformly spreads out over the circumference of the ring becoming a coasting one.

Since the beam position information is hidden in the frequency domain it is crucial for the BPMs to work only with bunched beam [65,66]. In our case, the transition point is located at the 186.85 keV. As a result, the values of the BPMs readings at the energies 187.0 keV and 187.1 keV were measured for the coasting beam. Thus these readings are concluded to be random values from electronics noise [67] and, based on the aforesaid reasoning, were excluded from the further analysis.

In the Equation (116) we operate with momentum deviations $\Delta p/p_0$. To convert from energy to momentum values the energy-momentum relation is used:

$$E^2 = (pc)^2 + (mc^2)^2 \quad (117)$$

Writing the differentials for both sides of the equation and with $E\beta = pc$ we obtain:

$$\frac{dE}{E} = \beta^2 \frac{dp}{p}, \quad (118)$$

from which we find the expression for momentum deviation:

$$\frac{\Delta p}{p} = \frac{1}{\beta^2} \frac{\Delta E}{E}. \quad (119)$$

Now we need to find the dispersion function. Let's consider two beam deviations x_1 and x_2 at two different relative energy deviations $(\Delta E/E)_1$ and $(\Delta E/E)_2$ at a certain BPM position. Subtracting the second from the first and using the Equation (119) we have:

$$x_2 - x_1 = \frac{D_x}{\beta^2} \frac{\Delta E}{E_0}, \quad (120)$$

where E_0 is a design energy which corresponds to the design momentum p_0 . Here β is the speed relative to the speed of light, not to be confused with $\beta_{x,y}$ – betatron functions.

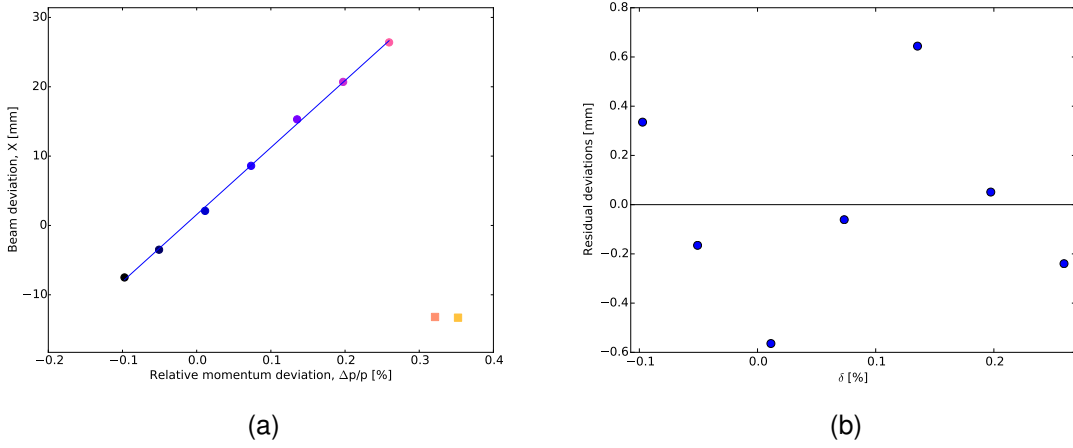


Figure 5.5: (a) The linearly fitted beam amplitude dependence on the relative momentum. The BPM is located at $s = 6.05$ m. The two momentum values above the transition energy (squared markers to the right) which corresponded to 170 keV and 171.1 keV were excluded from the fitting. (b) Residual deviations after the linear fit.

The Figure 5.5 shows the linearly fitted experimental data from the first BPM. The same linear fit procedure was applied to all of the BPMs in order to obtain in the end 12 values of dispersion.

In the plot, which shows the residual deviations after the fitting in Figure 5.5b, one can note the S-shaped dependence on the momentum. Such an S-pattern was observed in all other BPMs which indicates a non-statistical tendency and thereby suggests a presence of higher-than-linear terms in the dispersion function. This assumption will be reaffirmed later in the Section 5.3

After fitting the BPM data we find the twelve inclination angles corresponding to 12 monitors. Each angle gives the dispersion value according to Equation (120). The theoretically predicted values of the dispersion function in the isochronous ion optical lattice were calculated with the MIRKO accelerator code. The comparison between theory and the

experiment is presented in the Figure 5.6.

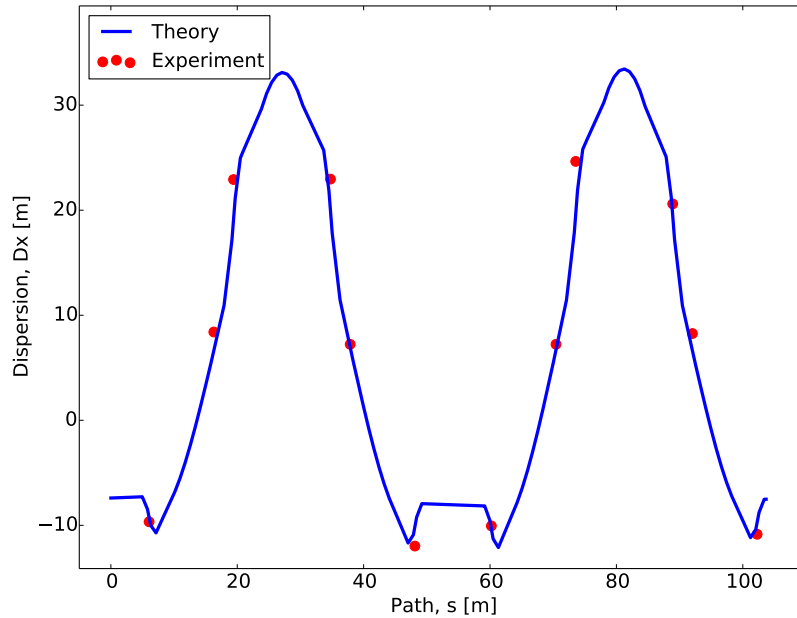


Figure 5.6: The comparison between theoretical predictions from MIRKO (blue) and the experimental values (red) of the dispersion in the ESR. The size of the errors for the experimental values is less than the marker size.

Except for few minor deviations, we can see a good agreement between the data from the experiment and the numerical simulations. This example – dispersion function calculation – demonstrates the validity and, what is important, high accuracy of the results obtained from the accelerator codes, which are used in the research.

5.3 Experiment. Transition energy

In the second part of the experiment the transition energy of the lattice was found. The Schottky detector system was used for this purpose.

5.3.1 Schottky detector

Schottky spectroscopy is a non-destructive method based on the frequency analysis of the circulating charged beam [68], which is used for precision mass measurements of nuclides. Because of the high charge states of the ions the Schottky system in the ESR is sensitive even to single stored ions due to high signal-to-noise ratio. The longitudinal Schottky spectrum during the experiment at the ESR was measured at the 130th harmonic of the revolution frequency.

5.3.2 Experiment outline

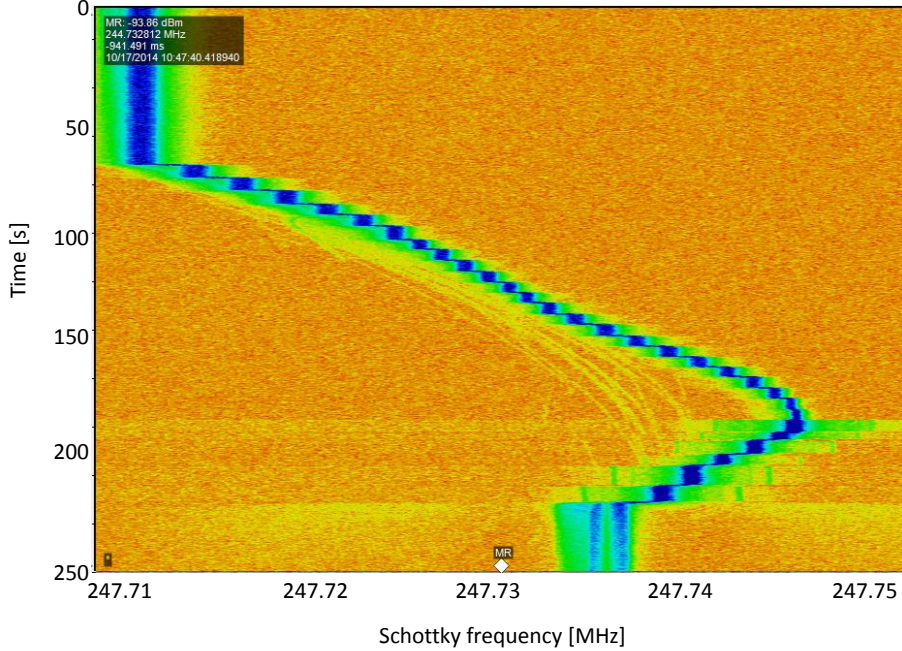


Figure 5.7: Frequency signal from the Schottky detector for the incremental increase of the electron cooler energy. One step corresponds to 50 eV.

Figure 5.7 shows the change of the revolution frequency of the beam during the incremental change the electron cooler energy. The latter was changed every 5 seconds in 50 eV steps from 185.7 keV up to 187.2 keV without changing the dipole guiding field. Outside this energy interval the beam was lost almost immediately after injection. Expressing the available energy range in terms of relative momentum deviation $\delta = \Delta p/p$, gives the momentum acceptance range of $[-0.08; 0.38]\%$.

One can see from Figure 5.7 that the frequency of the revolution increased during first 22 steps, reached the extremum at the 23rd, and then started to go down. The peak corresponds to the Schottky frequency of 244.745 MHz and the electron cooler energy ≈ 186.8 keV. The broadening of the beam frequency width just after crossing the transition energy can also be observed. It presumably comes from the beam longitudinal instabilities during the γ -crossing [44], which are described in the previous Section 5.1.

Figure 5.8 shows the relative frequency deviation as a function of the relative momentum shift. A non-linear behaviour can be observed prior to the function maximum – this can be explained by the non-linear dependence of the transition energy on the momentum. Now, applying the Equation (94), derived in Section 2.6, which describes the beam revolution frequency as a function of the momentum shift, we can find the transition

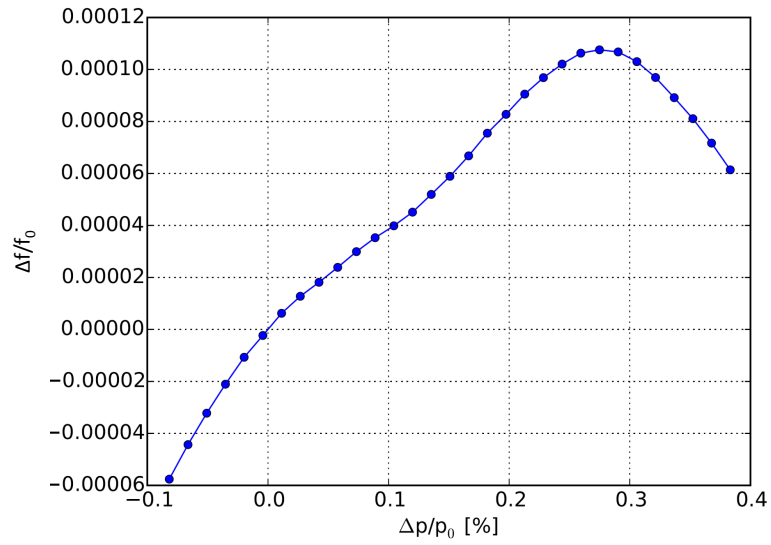


Figure 5.8: The relative frequency shift as a function of relative momentum deviation.

energy as a function of the relative momentum. This dependence is shown in Figure 5.9.

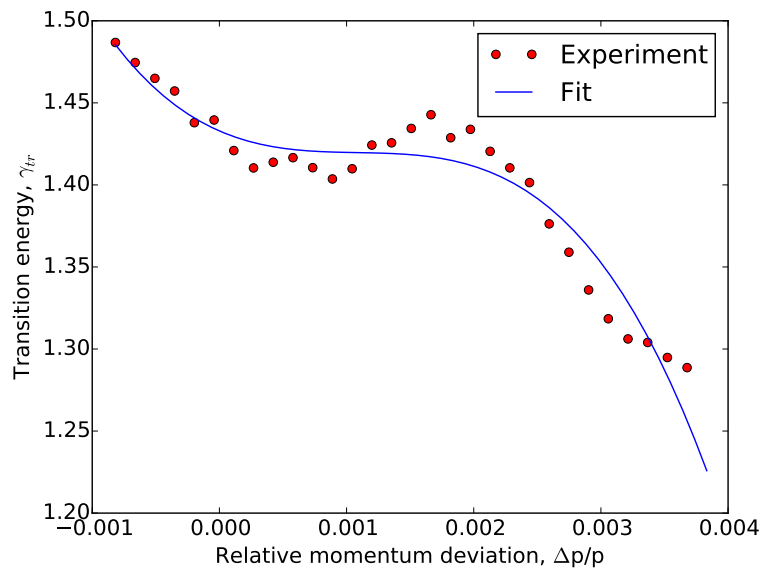


Figure 5.9: Transition energy from experimental data (red dots) as a function of relative momentum deviation, is fitted with cubic polynomial (blue curve).

A cubic polynomial interpolation can be performed to fit the dependence of the transition gamma on fractional momentum $\delta = \Delta p/p_0$:

$$\gamma_{rr}(\delta) = G_0 + G_1\delta + G_2\delta^2 + G_3\delta^3 \quad (121)$$

From the fit the polynomial coefficients are as follows:

$$G_0 = 1.433, G_1 = -34, G_2 = 3.0e3, G_3 = -9.2e6.$$

From Equations (87) and (92) we know that the transition energy is directly calculated from the dispersion function. Thus it can be concluded that latter contains higher than linear terms with strong 3rd order presence. This is an unfortunate effect for the mass measurements because of the strong requirements for high mass resolution accuracy. However, this difficulty can be overcome by performing the high-precision experiment in the fixed momentum range where the transition energy does not vary in the desirable margins [69].

6 Summary

A new ion optical setup dedicated for the operation of the HESR storage ring with heavy ions was designed. The developed heavy ion optics, comparing to the antiproton optics, is characterized by the 4 times enlarged acceptance, reduced quadrupole strengths and minimized chromaticities.

The designed optics was optimized by searching for the tune working point with a maximum dynamic aperture. This will potentially result in decrease of the beam losses during the experiments and prolong the beam lifetime.

The closed orbit correction was performed, which resulted in reducing the residual beam deviation to ± 2 mm in horizontal and ± 4 mm in the vertical plane.

The target-beam overlap was achieved for the worst-case scenario when the difference between the beam centroid and the center of the target is 5 mm. The present set of the dipole magnet correctors was explored and proven to be sufficient to correct the mismatch in terms of amplitude and angle. However it results in some unwanted residual up-to-15 mm beam deviations around the target.

The developed optics was checked for the possibility of the charge state separation of the Hydrogen-like and Helium-like uranium ions produced in the internal target experiments. With the present optics the charge exchange ions avoid hitting the aperture, as it would in the antiproton optics, and in the same time have sufficient separation at the location of the particle detector.

The study of the resonance structure for the optimized tune working point (5.809, 5.816) is completed. The correctness of the chosen working point was proven by the absence of resonances lower than 9th order in the beam tune map. However, for the maximum positive momentum shift of 0.05 % the tunes almost reach the difference resonance line. Therefore, the working point which is more distant from the difference resonance might be considered.

Two locations for the internal target, in the north-west as well as in the south-west arc of the HESR, are investigated. The employment of the latter can involve complications related to the upstream-located electron cooler. This location should be studied more deeply and the ion-electron recombination rate from the expected transverse and longitudinal temperatures of the electron cooler should be calculated.

The experiments with the Helium-like primary beam at the existing ESR storage ring at GSI were carried out. The dispersion function, which was calculated from the beam position monitors readings, was compared to the one obtained from the accelerator codes. The transition energy was measured with the aid of the installed Schottky spectrometers. Third-order momentum dependence in the transition energy was observed. This information could be employed for the future mass measurement experiments at the ESR storage ring.

The same tools and methods which were used in the optimization of the HESR optics

were applied in the above-described experiments. Essential outcome is that this allowed to benchmark the theoretical calculations. This gives us the necessary confidence for the future experiments in the HESR which strongly rely on the present ion-optical optimization.

List of Figures

1.1	FAIR layout [5] with existing (blue) and planned (red) facilities.	2
2.1	Motion in Frenet-Serret curvilinear coordinate system. The circular reference orbit (red) and particle oscillatory motion (blue) are shown. ρ - local bending radius, s - longitudinal coordinate parallel to the propagation direction of reference particle.	8
2.2	Pure quadrupole (a) and sextupole (b) fields in the transverse plane. For a quadrupole field the direction of the Lorentz force for a positively charged particle is presented with a green arrow, a black arrow shows the magnetic field direction.	13
2.3	Courant-Snyder invariant ellipse.	18
2.4	Phase space in normalized coordinates.	20
3.1	HESR layout.	32
4.1	Standard antiproton optics for PANDA experiment. Dispersion function is shown with green, horizontal beta function β_x - black, vertical beta function β_y denoted with red.	37
4.2	Blue line shows the dependence of the phase advance on the normalized gradient of the quadrupole in the FODO cell. The green zone indicates the range of the normalized gradient values for which the acceptance has the largest values.	39
4.3	Periodic solution for the optical functions in the FODO cell. The two long magnets are the dipoles. The first, the middle and the last magnets are the quadrupoles. The other magnetic elements are sextupoles or dipole corrector magnets – they did not affect the computation.	40
4.4	Optical functions for half of the arc.	41
4.5	Optical functions for the full lattice. The path length $s = 0$ corresponds to the beginning of the arc. The center of the electron cooler is located at $s = 250$ m, the PANDA target is positioned at $s = 509$ m.	42
4.6	Uncorrected (red) and corrected (blue) closed orbits are shown for ten random seeds for horizontal plane.	45
4.7	Uncorrected and corrected closed orbits maximum deviations are shown for 500 seeds for horizontal (blue) and for vertical (green) planes.	46
4.8	The closed orbit bump in the horizontal plane at the internal target location. Plot (b) is a magnified area from the orbit distortion in the plot (a). Its purpose is to show the amplitude and the angle of the orbit in a more precise way. . .	48
4.9	The closed orbit bump in the vertical plane at the internal target location. Plot (b) is a magnified area from the plot (a) to show the amplitude and the angle of the orbit more precisely.	48

4.10 Resonance diagram up to 4th order. The black line (1,-1) defines the difference resonance $Q_x - Q_y = 0$	50
4.11 Tune scan with the indicated old and new tune working points.	51
4.12 Coloured lines represent the resonance lines up to 8th order. The working point $(Q_x, Q_y) = (5.809, 5.816)$ is denoted with a black dot.	52
4.13 Dynamic aperture for the tune working point (5.809, 5.816), physical aperture (denoted as beam pipe projection) and the 2- σ beam are shown.	53
4.14 Optical functions of the lattice in heavy ion mode (solenoids included in the calculations): horizontal amplitude β_x (black), vertical amplitude β_y (red), dispersion function D_x (green). Path length s [m]: 0-156 m - north arc, 156-287 m - electron cooler, 287-443 m - south arc, 444-575 m - PANDA straight.	55
4.15 Comparison of the dynamic aperture of the ideal lattice after correction with two and with six sextupole families. The calculations were done for 10000 turns. The optical functions at the measurement location were $\alpha_x = \alpha_y = 0$, $\beta_x = 29$ m, $\beta_y = 79$ m.	56
4.16 Phase space portrait in horizontal plane (a) and in vertical plane (b) for the ideal lattice after chromaticity correction. Six sextupole families, three horizontal and three vertical, were employed. Four colors correspond to four particle initial amplitudes. The red color amplitude defines the border of particle motion stability for 5000 turns. The optical functions at the measurement location were $\alpha_x = \alpha_y = 0$, $\beta_x = 29$ m, $\beta_y = 79$ m.	56
4.17 Dynamic aperture as a function of number of turns computed for a momentum spread $\Delta p/p = 0$. Dynamic aperture is measured in the location where optics functions are: $\alpha_{x,y} \approx 0$, $\beta_x = 29$ m, $\beta_y = 79$ m. In blue shown a 2- σ beam right after injection from CR with the transverse emittance (2- σ) $\varepsilon_{x,y} = 0.5$ mm mrad (or rms $\varepsilon_{x,y} = 0.125$ mm mrad).	57
4.18 Dynamic aperture for $\Delta p/p = -0.0005$ at location with $\beta_x = 29$ m, $\beta_y = 79$ m. The palette bar to the right represents diffusion coefficient, i.e. a measure of chaoticity of particle with given initial coordinates. The dark-blue color represents most stable particle orbits whereas the red indicates high instability and diffusion. The black line denotes the physical aperture projection which is calculated from the $\beta_{x,y}$ -functions values at this location.	60
4.19 Main part of the tune map with fractional horizontal and vertical tunes for $\Delta p/p = -0.0005$. The resonances, those which have an impact on the particles motion, are shown.	61

4.20	Dynamic apertures with diffusion coefficient for momentum shifts $\Delta p/p = -0.0005$ (top), $\Delta p/p = 0$ (middle), $\Delta p/p = 0.0005$ (bottom). The physical aperture projection is denoted with black line. The ion-optical functions at the measurement location are $\alpha_x = \alpha_y = 0$, $\beta_x = 29$ m, $\beta_y = 79$ m.	62
4.21	Frequency map for different momentum shift $\Delta p/p = -0.0005$ (top), $\Delta p/p = 0$ (middle), $\Delta p/p = 0.0005$ (bottom).	63
4.22	Incoherent tune shift due to transverse direct space charge is plotted against the kinetic energy of the beam. The green dashed line shows the minimum achievable energy for bare uranium ions at the HESR which equals 170 MeV and the corresponding tune shift value 0.8×10^{-3} . The red dashed line denotes the injection energy 740 MeV with the corresponding tune shift of 7.4×10^{-3}	65
4.23	Two target locations and the corresponding regions of interest (ROI) are shown. The latter are highlighted with red transparent rectangulars. The motion of the beam is counter-clockwise which means that in the HESR west part the beam moves from the top to the bottom.	67
4.24	The top plot shows the propagation of the bare uranium beam after the electron cooler with H-like and He-like ions from the target charge exchange reactions, which are shown in yellow. In red color one can see the Hydrogen-like uranium ions coming as a result of the electron-ion recombination in the electron cooler. The dipoles, focusing and defocusing quadrupoles are represented with, respectively, cyan, red and blue rectangulars. The bottom plot shows the particle distributions obtained at the detector. The yellow peaks correspond to the main bare uranium beam and to the charge exchange reaction products from the target. Red denotes the H-like ions coming from the radiative recombination in the electron cooler. Remark: the ratios between the peaks do not correspond to the real intensities. The purpose is to show the transverse position and the distribution width of the corresponding ions in the particle detector.	69
4.25	The left plot shows the propagation of the bare uranium beam after the electron cooler and its charge exchange reaction products after the interaction with the target. The right plot shows the particle distributions obtained at the detector. The yellow peaks correspond to the main bare uranium beam and the charge exchange reaction products from the target. Remark: the ratios between the peaks do not correspond to the real intensities. The purpose is to show the transverse position and the distribution width of the corresponding ions in the detector.	70
5.1	General layout of the ESR storage ring.	71

5.2	Ion optical functions of the ESR in the isochronous mode.	72
5.3	The beam deviations for the electron energy range [185.65, 187.1] keV is shown. Each line denotes the beam deviation at the beam position monitors for the given energy, with black for the minimum and yellow for maximum energy value.	74
5.4	The beam amplitude at the first BPM as a function of the E-cooler energy is shown. The BPM is located at $s = 6.05$ m. The two values, denoted with filled squares, correspond to the energies 187.0 keV and 187.1 keV. The transition energy $\gamma_{tr} = 186.85$ keV is shown with dashed line.	75
5.5	(a) The linearly fitted beam amplitude dependence on the relative momentum. The BPM is located at $s = 6.05$ m. The two momentum values above the transition energy (squared markers to the right) which corresponded to 170 keV and 171.1 keV were excluded from the fitting. (b) Residual deviations after the linear fit.	76
5.6	The comparison between theoretical predictions from MIRKO (blue) and the experimental values (red) of the dispersion in the ESR. The size of the errors for the experimental values is less than the marker size.	77
5.7	Frequency signal from the Schottky detector for the incremental increase of the electron cooler energy. One step corresponds to 50 eV.	78
5.8	The relative frequency shift as a function of relative momentum deviation. . .	79
5.9	Transition energy from experimental data (red dots) as a function of relative momentum deviation, is fitted with cubic polynomial (blue curve).	79

List of Tables

2.1	Normal (upright) multipole components in Cartesian and cylindrical coordinates.	14
3.1	Magnets at the HESR.	31
4.1	A list of the parameters of the antiproton optics.	36
4.2	A list of the parameters of the heavy ion mode optics.	43
4.3	A list of the parameters of the heavy ion mode optics.	54
4.4	Comparison of the beam parameters of the injected beam and after electron cooling. All rms values.	67

Accelerator terms

beam cooling The process which reduces the beam phase space. The most effective so far are electron and stochastic cooling.

beam position monitor A diagnostics device which measures the transverse position of the beam by measuring the strength of the electric field produced by the beam.

beta function Measure of a beam width.

betatron oscillations A stable oscillation around the equilibrium orbit, in vertical and horizontal planes. The restoring force for the oscillation is provided by the quadrupole.

bump A local closed orbit bump created with dipole corrector magnets.

chromaticity Linear rate of tune change with momentum change.

closed orbit The path about which particle performs betatron oscillations. It changes with magnet errors and particle momentum.

dispersion The change of particle position with relative momentum offset $\Delta p/p$.

dynamic aperture The maximum values of the initial betatron amplitudes, with which the motion of the particle is still stable.

lattice A periodic arrangement of the bending magnets, quadrupoles and other magnetic elements in an accelerator.

momentum compaction A relative variation of the orbital length with momentum change.

phase advance A fraction of a betatron oscillation. 2π phase advance corresponds to one full oscillation.

phase space A six-dimensional hyper-volume consisting of particles positions and momenta in three orthogonal planes (x, p_x, y, p_y, z, p_z) .

resonance A condition when a perturbing force disturbs the particle motion so the betatron oscillations grow indefinitely.

RF cavity A normal conducting or superconducting metal chamber that contains the electromagnetic field used for particles acceleration.

synchrotron radiation An electromagnetic radiation which a particle emits when accelerated perpendicular to its velocity vector, e.g. in circular motion.

working point A point (region) on the tune diagram Q_x vs Q_y where the machine operates.

References

- [1] FAIR. <http://www.fair-center.eu/for-users.html>.
- [2] Th Stöhlker, HF Beyer, A Bräuning-Demian, C Brandau, A Gumberidze, RE Grisenti, S Hagmann, F Herfurth, Ch Kozhuharov, Th Köhl, et al. SPARC: The Stored Particle Atomic Research Collaboration At FAIR. In APPLICATION OF ACCELERATORS IN RESEARCH AND INDUSTRY: Twenty-First International Conference, volume 1336, pages 132–137. AIP Publishing, 2011.
- [3] Thomas Stöhlker, Yuri A Litvinov, Vincent Bagnoud, Ulf Bechstedt, Christina Dimopoulou, Alexei Dolinskii, Christopher Geppert, Siegbert Hagmann, Takeshi Katayama, Thomas Köhl, et al. SPARC experiments at the high-energy storage ring. *Physica Scripta*, 2013(T156):014085, 2013.
- [4] Thomas Stöhlker, Yuri A Litvinov, Angela Bräuning-Demian, Michael Lestinsky, Frank Herfurth, Rudolf Maier, Dieter Prasuhn, Reinhold Schuch, and Markus Steck. SPARC collaboration: new strategy for storage ring physics at FAIR. *Hyperfine Interactions*, 227(1-3):45–53, 2014.
- [5] Eberhard Widmann. Perspectives for low energy antiproton physics at fair. *Hyperfine Interactions*, 229(1-3):123–128, 2014.
- [6] MADX. <http://mad.web.cern.ch/mad/>.
- [7] PJ Bryant. AGILE, a tool for interactive lattice design. Technical report, 2000.
- [8] MIRKO. https://www.gsi.de/en/work/fairgsi/primary_beams/abteilungen/system_planning/lattice_design_and_ion_optics/mirko.htm.
- [9] Shyh-Yuan Lee. Accelerator physics, volume 491. World scientific Singapore, 1999.
- [10] LD Landau and EM Lifshitz. *Mechanics*, 1976.
- [11] Helmut Wiedemann et al. Particle accelerator physics, volume 314. Springer, 2007.
- [12] S Turner. CAS CERN Accelerator School. 5. Advanced accelerator physics course. Proceedings. Vol. 1. Technical report, European Organization for Nuclear Research, Geneva (Switzerland), 1995.
- [13] Toru Ogitsu, Yasuo Ajima, Michael Anerella, John Escallier, George Ganetis, Ramesh Gupta, Dietrich Hagedorn, Michael Harrison, Norio Higashi, Yosuke Iwamoto, et al. Superconducting combined function magnet system for J-PARC neutrino experiment. *Applied Superconductivity, IEEE Transactions on*, 15(2):1175–1180, 2005.

- [14] Klaus Wille. The physics of particle accelerators. Oxford Univ. Press, 2000.
- [15] George William Hill. On the part of the motion of the lunar perigee which is a function of the mean motions of the sun and moon. *Acta mathematica*, 8(1):1–36, 1886.
- [16] J Liouville. Note on the Theory of the Variation of Arbitrary Constants. *Journ. de Math*, 3:349, 1838.
- [17] Yuri A Litvinov. Mass and half-life measurements of stored exotic nuclei at the FRS-ESR facility. *Nuclear Physics A*, 805(1):260c–269c, 2008.
- [18] MHR Donald, PL Morton, H Wiedemann, et al. Chromaticity correction in large storage rings. *IEEE Trans. Nucl. Sci*, 24:1200–1202, 1977.
- [19] Philip J Bryant and Kjell Johnsen. The principles of circular accelerators and storage rings. Cambridge University Press, 2005.
- [20] Ralph J Steinhagen. Tune and chromaticity diagnostics. CAS, Dourdan, France, page 317, 2008.
- [21] Herbert Goldstein, Charles Poole, John Safko, and Stephen R Addison. Classical mechanics. *American Journal of Physics*, 70(7):782–783, 2002.
- [22] Eric Winsberg. Simulated experiments: Methodology for a virtual world. *Philosophy of science*, 70(1):105–125, 2003.
- [23] Ronald Kleiss, F Schmidt, and Y Yan. On the feasibility of tracking with differential-algebra maps in long-term stability studies for large hadron colliders. Technical report, Superconducting Super Collider Lab., Dallas, TX (United States). Funding organisation: USDOE, Washington, DC (United States), 1992.
- [24] Vladimir Igorevich Arnold. Mathematical methods of classical mechanics, volume 60. Springer Science & Business Media, 1989.
- [25] Vladimir I Arnold. Instability of dynamical systems with several degrees of freedom (Instability of motions of dynamic system with five-dimensional phase space). *Soviet Mathematics*, 5:581–585, 1964.
- [26] Jacques Laskar. Frequency analysis for multi-dimensional systems. *Global dynamics and diffusion. Physica D: Nonlinear Phenomena*, 67(1):257–281, 1993.
- [27] Massimo Giovannozzi, Walter Scandale, and Ezio Todesco. Prediction of long-term stability in large hadron colliders. *Part. Accel.*, 56(LHC-Project-Report-45):195–225, 1996.

- [28] R Bartolini, IPS Martin, G Rehm, and F Schmidt. Calibration of the nonlinear ring model at the Diamond Light Source. *Physical Review Special Topics-Accelerators and Beams*, 14(5):054003, 2011.
- [29] P Brunelle, A Loulergue, A Nadji, LS Nadolski, MA Tordeux, et al. Non linear beam dynamics studies at SOLEIL using experimental frequency map analysis. *Proceedings of IPAC*, 10:4653–4655, 2010.
- [30] Inti Lehmann et al. Physics Programme of PANDA at FAIR. arXiv preprint arXiv:0909.4237, 2009.
- [31] Nikos Petridis. Private communication, 2014.
- [32] R. Grisenti et al. Design of the target at HESR,.
- [33] PHELIX laser system. https://www.gsi.de/start/forschung/forschungsgebiete_und_experimente/appa_pni_gesundheit/plasmaphysikphelix/phelix.htm.
- [34] H Stockhorst, R Maier, D Prasuhn, and R Stassen. Stochastic momentum cooling experiments with a barrier bucket cavity and internal targets at COSY-Jülich in preparation for HESR at FAIR. *IPAC*, 10:846, 2010.
- [35] Rudolph Maier. High.
- [36] Bruno Autin. Dispersion suppression with missing magnets in a FODO structure-application to the CERN Antiproton Accumulator. *IEEE Trans. Nucl. Sci.*, 26(CERN-PS-AA-79-18):3493–5, 1979.
- [37] GI Budker. An effective method of damping particle oscillations in proton and antiproton storage rings. *Soviet Atomic Energy*, 22(5):438–440, 1967.
- [38] T. Katayama et al. Electron.
- [39] Markus Steck, C Dimopoulou, A Dolinskii, O Gorda, T Katayama, SA Litvinov, Yu A Litvinov, F Nolden, C Peschke, and Th Stöhlker. Current Plans for Beam Cooling at FAIR. *RUPAC*, 12:63–67.
- [40] O. Dolinsky et al. Technical Design Report on the Collector Ring. Technical report, 2013.
- [41] Juelich Research Center. www.fz-juelich.de.
- [42] Berndt Lorentz. Private communication, 2013.

- [43] Xiaobiao Huang. Matrix formalism of synchrotron coupling. *Physical Review Special Topics-Accelerators and Beams*, 10(1):014002, 2007.
- [44] Elias Métral and Dieter Möhl. TRANSITION CROSSING.
- [45] H Stockhorst, R Maier, D Prasuhn, R Stassen, T Katayama, et al. Feasibility Study of Heavy Ion Storage and Acceleration in the HESR with Stochastic Cooling and Internal Targets, 2013.
- [46] H Soltner, U Bechstedt, R Tölle, and JG de Villiers. Magnetic-Field Calculations for the Magnets of the High-Energy Storage Ring (HESR) at FAIR. Proc. of PAC09, Vancouver, BC, Canada, MO6PFP016, 166(8), 2009.
- [47] Werner Herr. Implementation of new closed orbit correction procedures in the MAD-X program. Technical report, 2002.
- [48] Frank Zimmermann. Measurement and correction of accelerator optics. Proceedings of the 1998 Joint US-CERN-Japan-Russia School on Particle Accelerators, Montreux, pag, pages 17–20, 1998.
- [49] Massimo Giovannozzi, Walter Scandale, and Ezio Todesco. Dynamic aperture extrapolation in the presence of tune modulation. *Physical Review E*, 57(3):3432, 1998.
- [50] R Bartolini, A Verdier, Ezio Todesco, C Pellegrini, M Cornacchia, J Corbett, Massimo Giovannozzi, Walter Scandale, and P Tran. Measurements of the tune variations induced by non-linearities in lepton machines. Technical report, 1996.
- [51] Thomas H Cormen, Charles E Leiserson, Ronald L Rivest, Clifford Stein, et al. Introduction to algorithms, volume 2. MIT press Cambridge, 2001.
- [52] Matteo Frigo and Steven G Johnson. The design and implementation of FFTW3. *Proceedings of the IEEE*, 93(2):216–231, 2005.
- [53] GSI Computing Grid. <https://wiki.gsi.de/foswiki/bin/view/Linux/GridEngine>.
- [54] Frank Schmidt. Mad-x ptc integration. In Particle Accelerator Conference, 2005. PAC 2005. Proceedings of the, pages 1272–1274. IEEE, 2005.
- [55] Yannis Papaphilippou. Frequency maps of LHC models. In Particle Accelerator Conference, 1999. Proceedings of the 1999, volume 3, pages 1554–1556. IEEE, 1999.
- [56] L Nadolski and J Laskar. Review of single particle dynamics for third generation light sources through frequency map analysis. *Physical Review Special Topics-Accelerators and Beams*, 6(11):114801, 2003.

- [57] Jocelyn Couetdic, Jacques Laskar, Alexandre CM Correia, Michel Mayor, and Stéphane Udry. Dynamical stability analysis of the HD 202206 system and constraints to the planetary orbits. *Astronomy & Astrophysics*, 519:A10, 2010.
- [58] David Robin, C Steier, J Laskar, and L Nadolski. Global dynamics of the advanced light source revealed through experimental frequency map analysis. *Physical review letters*, 85(3):558, 2000.
- [59] J Rossbach and P Schmüser. Basic course on accelerator optics. CERN European Organization for Nuclear Research-Reports-CERN, pages 17–17, 1994.
- [60] Karlheinz Schindl. Space charge. Proceedings of the Joint US-CERN-Japan-Russia School on Particle Accelerators in Montreux, 1998.
- [61] AN Artemyev, VM Shabaev, Th Stöhlker, and AS Surzhykov. Negative continuum dielectronic recombination and its competitive processes.
- [62] AN Artemyev, VM Shabaev, Th Stöhlker, and AS Surzhykov. Negative-continuum dielectronic recombination into excited states of highly charged ions. *Physical Review A*, 79(3):032713, 2009.
- [63] ESR website. https://www.gsi.de/en/start/forschung/forschungsfelder/appa_pni_gesundheit/atomphysik/research/experimental_facilities/esr.htm.
- [64] M Steck, K Beckert, H Eickhoff, B Franzke, F Nolden, H Reich, B Schlitt, and T Winkler. Lowest temperatures in cooled heavy ion beams at the ESR. In EPAC, volume 98, page 1064, 1998.
- [65] P Kowina, W Kaufmann, J Schölles, and M Schwickert. Optimisation of shoe-box type beam position monitors using the finite element methods. In Proceedings of DIPAC, 2005.
- [66] Robert E Shafer. Beam position monitoring. In AIP Conference Proceedings, volume 212, pages 26–58, 1989.
- [67] Oleksandr Chorniy. Private communication, 2014.
- [68] Bernhard Schlitt, K Beckert, T Beha, H Eickhoff, B Franzke, H Geissel, H Irnich, HC Jung, TF Kerscher, O Klepper, et al. Schottky mass spectrometry at the heavy ion storage ring ESR. *Hyperfine Interactions*, 99(1):117–125, 1996.
- [69] Sergei Litvinov. Private communication, 2014.
- [70] T. Stöhlker et al. IX.

- [71] R. Maier. High Energy Storage Ring HESR, FAIR MAC. <http://indico.gsi.de/getFile.py/access?sessionId=3&resId=0&materialId=5&confId=532>, 2009.
- [72] Brian William St Leger Montague. Basic Hamiltonian mechanics. 1995.
- [73] Jacques Laskar. Introduction to frequency map analysis. In Hamiltonian systems with three or more degrees of freedom, pages 134–150. Springer, 1999.
- [74] J Laskar et al. Frequency map analysis and particle accelerators. Portland, PAC, 3:378–382, 2003.

Acknowledgements

I am sincerely grateful to my tutor at GSI Yuri Litvinov for the guidance during writing of the thesis. Despite extremely busy schedule, he has been always managing to stay "online" for invaluable support and scientific assistance.

I want to express my gratitude to Oleksiy Dolinsky, priceless discussions with whom on the accelerator physics topics as well as his high-value recommendations have made an enormous impact on the study.

I thank Andrey Surzhykov for accepting me as a PhD student and also for fascinating and educative scientific conversations on frequent occasions at various conferences.

I would like to thank Sergey Litvinov, not only as my football teammate and fantastic goalkeeper, but also as an excellent accelerator physicist who provided me with priceless assistance during the study time. I also acknowledge Markus Steck, who together with Sergey got me involved in the experiment at the ESR storage ring where I've had an incredible opportunity of operating the accelerator machine.

Many thanks go to the FZ Jülich community including Bernd Lorentz, Hans Stockhorst, Takeshi Katayama and Dieter Prasuhn who are heavily committed to the HESR storage ring project. They have been so kind to provide me with all the important information concerning the lattice beam optics (Bernd Lorentz), stochastic and electron beam cooling details (Hans Stockhorst and Takeshi Katayama) and general directions for the ion optical improvements (Dieter Prasuhn).

I thank Yuri Senichev for the fruitful discussions on the beam dynamics optimization in the HESR and Giuliano Franchetti who introduced me to the Micromap particle tracking library.

I am grateful to Yannis Paphilippou for the valuable discussions on the Frequency Map Analysis technique. Special thanks goes to Phil Bryant who introduced me to a WinAgile accelerator design program. It is important to mention Michele Carla with whom I was fortunate to share a flat during the JUAS accelerator school. I thank him for our enthusiastic disputes concerning different aspects of accelerator physics.

I specially thank Pierre-Michel Hillenbrand for the conversation time on atomic physics topics, Shahab Sanjari for his assistance with Schottky spectra analysis, Nikos Petridis for explanations on the principle of operation of gas-jet targets and Thomas Stöhlker for providing an effective working environment in the SPARC collaboration.

The acknowledgments go to Maksym Zyzak and Yuri Sorokin for the lunch-time debates on the fundamental physics as well as programming techniques.

I thank Tatiana Litvinova who has been gigantically helping with the organizational

issues throughout the course of the study. She, together with Fritz Bosch, are also greatly acknowledged for the German translation of the "Abstract" for the current paper.

Finally, I am most grateful to my family, my parents and my wife, for their strongest support and enormous patience, especially during the writing of the thesis. Without them this paper would not have been possible.